Lee, Chang Sheng (2023) *Advanced sensing technologies and systems for lung function assessment.* PhD thesis.

Advanced Sensing Technologies and Systems for Lung Function Assessment

Lee Chang Sheng

B.Eng Mechatronics Engineering, University of Glasgow, Glasgow, 2013

M.Sc Mechanical Engineering, National University of Singapore, Singapore, 2016

Matriculation Number: XXXXXXXX

Submitted in fulfilment of the requirements for the

Degree of Doctor of Philosophy

James Watt School of Engineering

College of Science and Engineering

University of Glasgow

June 2023

Abstract

Chest X-rays and computed tomography scans are highly accurate lung assessment tools, but their hazardous nature and high cost remain a barrier for many patients. Acoustic imaging is an alternative to lung function assessment that is non-hazardous, less costly, and has a patient-to-equipment approach. In this thesis, the suitability of acoustic imaging for lung health assessment is proven via systematic review and numerical airway modelling. An acoustic lung sound acquisition system, consisting of an optimal denoising filter translated into imaging for continual and reliable lung function assessment, is then developed.

To the author's best knowledge, locating obstructed airways via an acoustic lung model and the resulting acoustic lung imaging have yet to be investigated in the open literature; hence, a novel acoustic lung spatial model was first developed in this research, which links acoustic lung sounds and acoustic images with pathologic changes. About 89% structural similarity between an acoustic reference image based on actual lung sound and the developed model acoustic image based on the computation of airway impedance was achieved.

External interference is inevitable in lung sound recordings; thus, an indirect unifying of wavelet-based total variation (WATV) and empirical Wiener denoising filter is proposed to enhance recorded lung sound signals. To the author's best knowledge, the integration of WATV and Wiener filters has not been investigated for lung sound signals. Selection and analysis of optimal parameters for the denoising filter were performed through a case study. The optimal parameters achieved through simulation studies led to an average 12.69 ± 5.05 dB improvement in signal-to-noise ratio (SNR), and the average SNR was improved by 16.92 ± 8.51 dB in the experimental studies. The hybrid denoising filter significantly enhances the signal quality of the captured lung sounds while preserving the characteristics of a lung sound signal and is less sensitive to the variation of SNR values of the input signal.

A robust system was developed based on the established lung spatial model and denoising filter through hardware redesign and signal processing, which outperformed commercial digital stethoscopes regarding SNR and root mean square error by about 8 dB and 0.15, respectively. Regarding sensing sensitivity power spectrum mapping, the developed system sensors' position is neutral, as opposed to digital stethoscopes, when representing lung signals, with a signal power loss ratio of around 5 dB compared to 10 dB from digital stethoscopes. The developed system obtains better detection by about 10% in the obstructed airway region compared to digital stethoscopes in the experimental studies.

Table of Contents

List of Tables

List of Figures

Acknowledgement

Author's Declaration

I declare that, except where explicit reference is made to the contribution of others, this dissertation is the result of my own work and has not been submitted for any other degree at the University of Glasgow or any other institution. This thesis has been produced in accordance with the University of Glasgow's Code of Good Practice in Research.

Printed Name: Chang Sheng Lee

Signature:

Publications

Patent

[1]   C. S. Lee, Y. Lou, M. Li, and R. Dahiya, "Lung imaging system for targeted therapy" U.S. Patent Application No. 20230104486, Oct 05, 2022.

Journal papers

[2]   C. S. Lee, M. Li, Y. Lou, and R. Dahiya, "Restoration of lung sound signals using a hybrid wavelet-based approach," *IEEE Sensors Journal*, vol. 22, no. 20, pp. 19700-19712, Oct.15, 2022.

[3]   C. S. Lee, Y. Lou, M. Li, Q. H. Abbasi, and M. A. Imran, "Locating nidi for high-frequency chest wall oscillation smart therapy via acoustic imaging of lung airways as a spatial network," in *IEEE Access*, doi: 10.1109/ACCESS.2023.3317443.

[4]   C. S. Lee, M. Li, Y. Lou, Q. H. Abbasi, and M. A. Imran, "Acoustic lung imaging utilized in continual assessment of patients with obstructed airway: A systematic review," *Sensors*, vol. 23, no. 13, p. 6222, Jul. 2023

[5]   C. S. Lee, M. Li, Y. Lou, Q. H. Abbasi, and M. A. Imran, "An acoustic system of sound acquisition and imaging generation for frequent and reliable lung function assessment," submitted to *IEEE Sensors Journal*, Jun 02, 2023

Conference papers

[6]   C. S. Lee, M. Li, Y. Lou, and R. Dahiya, "A hybrid approach of wavelet-based total variation and Wiener filter to denoise adventitious lung sound signal for an accurate assessment," *2022 IEEE International Conference on Consumer Electronics (ICCE)*, 2022, pp. 1-6.

[7]   C. S. Lee, M. Li, Y. Lou, and R. Dahiya, "Selecting efficient parameters thresholds for a hybrid wavelet-based total variation and Wiener filter for denoising lung sound signals," *2022 6th International Conference on Imaging, Signal Processing and Communications (ICISPC)*, Kumamoto, Japan, 2022, pp. 106-110.

[8]   C. S. Lee, M. Li, Y. Lou, and R. Dahiya, "Modelling and simulation of pulmonary acoustic signal and imaging for lung function assessment," *2023 IEEE International Conference on Consumer Electronics (ICCE)*, Las Vegas, NV, USA, 2023, pp. 01-06.

[9]   C. S. Lee, M. Li, Y. Lou, and R. Dahiya, "The effect of sensor array design on acoustic imaging for enhancing HFCWO therapy," presented at the *2023 IEEE International Multi-Conference on Systems, Signals and Devices (SSD)*, Mahdia, Tunisia, Feb 22, 2023.

[10]   C. S. Lee, M. Li, Y. Lou, and R. Dahiya, "Design of a robust lung sound acquisition system for reliable acoustic lung imaging," presented at the *2023 IEEE International Ultrasonics Symposium*, Montreal, Quebec, Canada, Sep 03, 2023.

Nomenclature and Abbreviations

Nomenclature

A	Reduced incidence matrix
A_s	Cross-sectional area of an airway segment
A_o	Airway area
A_i	Luminal area
a_n	Captured ambient noise without lung signals
a_s	Capture lung signals with noise
b	Branches
$\mathbb{C}$	Set of complex numbers
c	Cartilage ($k = 1$ to 17)
C_0	Capacitance
c_g	Speed of sound in air
C_g	Air specific heat
C_t	Terminal tissue compliance
C_1, C_2	Constants for reference image Q_r and captured image Q
d	Denoised signal
D	First-order difference matrix
D_o	Airway diameter
D_i	Internal airway diameter
E_s	Airway wall modulus soft tissue
E_c	Airway wall modulus cartilage
E_i	Young's modulus, subscript i replaced by c for the cartilage or by s for the soft tissue
F	Flow rate
F_1	Input flow
F_2	Output flow
F_v	Sound attenuation by air viscosity
F_s	Sampling frequency
F_t	Sound attenuation by thermal dissipation
f_{WS}	Word select frequency
f_y	Noisy signal peak amplitude from the database

G_0	Conductance
G_i	Conductance, subscript i replaced by c for the cartilage or by s for the soft tissue
H	Empirical Wiener filter
h	Interpolation function
H_w	Airway wall thickness
i	Sensor position
$\mathbf{I_s}$	Branch current source vector
$\mathbf{I}$	Node current vector
I_t	Terminal tissue inertance
j	Wavelet scale index
J	number of data collected
$\mathbf{J_s}$	node source current vector
$J_0(z_v), J_1(z_v),$ $J_0(z_t), J_1(z_t)$	Bessel functions
k	Airway segment layer
k_a	Harmonic order of amplitude modulation
k_m	Number of vanishing moment
K_g	Air thermal conductivity
l	Axial coordinate?
L_0	Inductance
L_i	Inductance, subscript i replaced by c for the cartilage or by s for the soft tissue
m	Row matrix
m_a	Amplitude modulation
m_f	Frequency modulation
n	Column matrix
N	Total sample number
L_n	Nidus length
P	Pressure, airway pressure
$\bar{P}$	Lung pressure signal over a time interval
P_1	Input pressure
P_2	Output pressure

P	Sound pressure within the airways
N_s	Total number of airway pressure signals within a known boundary
P_n	Node acoustic pressure matrix or should be k?
P_0	Reference sound pressure
P_s	Sinusoidal voltage source
Q	Acoustic lung image
Q_r	Reference lung image
$\mathbb{R}$	Set of real numbers
R_0	Acoustic resistance
R_i	Resistance, subscript i replaced by c for the cartilage or by s for the soft tissue
R_t	Terminal tissue resistance
S_i	Sensor sensing position
s_n	Sample number/size
s	Soft tissue (k = 18 to 35)
T	Total time
t	Time
t_k	Time interval
u	Sensing sensitivity test number
V_s	Branch voltage source vector
V	Branch voltage vector
V_n	Node voltage vector
v_a	Modulated airflow noise
v_e	Ambient noise
v_f	Noise from electronic sensor
v_t	Total noise from ambient, airflow, and electronic sensor
v_w	WGN for wheeze airflow source
V_c	Airway wall viscosity cartilage
W	Wavelet transform
x	x-axis
x_a	Output of airflow hitting on the airway
$\hat{x}_a$	Estimated output of airflow hitting on the airway

x_e	Simulated noise-free lung signal
x_f	Output of airflow hitting on the airway with noise
x_n	Amplitude of noise free lung signals
x_r	Airflow transmitted out of the chest and recorded with an electronic sensor
x_s	Airflow in the airway
x_t	WATV signal
$\hat{x}_t$	Estimated WATV signal
x_w	Simulated white noise
y	y-axis
y_r	Airflow recorded with a sensor
y_s	Simulated noisy lung signal
Y	Acoustical admittance
$\mathbf{Y}$	Branch admittance matrix
$\mathbf{Y_b}$	Branch admittance vector
$\mathbf{Y_n}$	Node admittance matrix
Y_g	Segment admittance
Y_k	k-th layer admittance
$\mathbb{Z}$	Set of sinusoidal variables
Z	Acoustical impedance
Z_c	Characteristics impedance
Z_g	Segment impedance
Z_k	k-th layer impedance
Z_{s0}	Small sinusoidal impedance
Z_w	Wall impedance
ω	Angular frequency
ω_c	Wavelet coefficient
Δ	Recursion index
γ	Propagation coefficient
α	Internal airway radius
α_j	Threshold shape controller
β	TV parts

σ	Square root of noise variance
η	Control parameter
ζ	Acoustic image area (control/reference)
λ_j	Regularization parameter
ρ_g	Air density
v_g	Airway wall viscosity
ρ_c, ρ_s	Lung density
μ	Step size
τ	Obstructed airway acoustic image
θ	Threshold function
μ_{Qr} and μ_Q	Local means for reference image Q_r and captured image Q
σ_{Qr} and σ_Q	Standard deviations for reference image Q_r and captured image Q
σ_{QrQ}	Cross-covariance for reference image Q_r and captured image Q

Abbreviations

1D	One dimensional
2D	Two dimensional
3D	Three dimensional
ACT	Airway clearance therapy
AWT	Airway wall thickness
BP	Bandpass
COPD	Chronic obstructive pulmonary disease
CRD	Chronic respiratory diseases
CT	Computed tomography
COVID-19	Coronavirus-2 disease 2019
e.g.	Example
EIT	Electrical impedance tomography
FIR	Finite impulse response
FPC	Flexible printed circuit
HFCWO	High-frequency chest wall oscillation
i.e.	That is
LUS	Lung ultrasound

MCC	Mucociliary clearance
MEMS	Micro-electromechanical systems
MRI	Magnetic resonance imaging
MSE	Mean square error
NOS	Newcastle-Ottawa scale
PCB	Printed circuit board
PRISMA 2020	Preferred Reporting Items for Systematic Reviews and Meta-Analyses 2020
RMSE	root mean square error
RTI	Respiratory tract infection
SALSA	Split augmented Lagrangian shrinkage algorithm
SCK	Serial clock
SD	Serial data
SG	Savitzky-Golay
SNR	Signal-to-noise ratio
SPIDER	Sample, Phenomenon of Interest, Design, Evaluation, Research type
SSIM	Structural similarity
TDM	Time-division multiplexing
TV	Total variation
VC	Volume control
VRI	Vibration response imaging
WATV	Wavelet-based total variation
WATV-Wiener	Hybrid WATV and empirical Wiener filter
WGN	White Gaussian noise
WS	Word select
WSO	Word select output

Chapter 1   Introduction

Chronic respiratory diseases (CRD) affect the lung and lead to chest pain, shortness of breath, coughing, and thick mucus production. Routinely, CRD are characterised by the thickening of airway walls (airway inflammation) and mucus, leading to airflow obstruction. Hillrom's Monarch® Airway Clearance System, a modern high-frequency chest wall oscillation (HFCWO) respiratory home care product, provides effective airway clearance therapies for patients to perform respiratory therapy at home. Modern HFCWO device is equipped with individual mechanical pods that can be activated independently and applied onto the patient's thorax to thin the mucus and remove mucus either through coughing or swallowing by providing small oscillations of mechanical pods at relatively high frequencies, typically between 5 and 20 Hz (intensity) for a duration of about 15 to 30 minutes. Therapy parameters such as the intensity and the duration differ for individuals and depend highly on the patient's lung function condition at that point in time. The current practice is that patients will report to the hospital for a quarterly check on their lung health before an adjustment can be performed to the respiratory therapy parameter.

Airway inflammation and the thickening of mucus can alter the production and transmission of lung sound spectrally and regionally [11-16]. The changes in lung sound transmission and production for alterations in the structure and function of our respiratory system can be measured quantitatively via digital stethoscope auscultation or lung imaging. While chest X-rays and computed tomography (CT) are the usual technology for detecting changes in the lung structure and function through imaging, they are costly to operate and require a patient-to-equipment/facilities approach. These methods have hazardous health effects that are also unsuitable for frequent assessment. During an outbreak of diseases, e.g., COronaVIrus-2 Disease 2019 (COVID-19), the patient-to-equipment approach is undesirable, where movement in public and hospitals are restricted to prevent cross-contamination and worsening lung conditions. Comparably, auscultation is a patient-to-equipment approach that requires patients' full corporation and specific placement of the digital stethoscope on the chest area for optimal analysis. Hence, auscultation by digital stethoscope is also tricky for frequent assessment of the patient's lung condition due to the patient-to-equipment approach.

In this thesis, a system was developed to overcome challenges faced by existing lung function assessment techniques by mapping lung sound distribution and locating airway obstruction (nidi) into intuitive acoustic lung images for frequent and continual monitoring.

The system consists of a hardware platform with an array of micro-electromechanical systems (MEMS) microphones for simultaneous lung sounds acquisition at a different location, signal processing for enhancing captured lung sounds, and an imaging algorithm to translate the captured lung sounds into intuitive imaging for lung function assessment.

1.1 Research Motivation

From the discussion earlier, it will be helpful if patients or clinicians can assess lung health conditions frequently to optimise respiratory therapy and target the affected lung region. Adapting respiratory therapy to individual patients' unique medical development is challenging as auscultation or imaging was used only during periodical medical visits to check the patient's lung function. The therapy outcome can be bolstered by frequent or continual observation of lung functions [17, 18].

Acoustic imaging transmuted from recorded lung sounds with an array of digital sensors is a straightforward technique for early and continual lung function assessment, non-hazardous, provides an equipment-to-patient approach and enhances healthcare delivery to patients with lung diseases [19, 20]. Vibration response imaging (VRI) has been proposed to monitor respiratory distribution within the lungs dynamically and is regarded as a digital stethoscope alternative which records vibration emitted from the chest using an array of digital stethoscope sensors alike and converts them into grey-scale images for analysis. VRI technology is an excellent way to detect lung sound distribution during mechanical ventilation in several studies [11, 21-23]. VRI can detect respiratory distribution under a controlled environment, not affected by mild acute respiratory diseases [24]. VRI is also in excellent agreement with electrical impedance tomography (EIT), which has a high linear correlation with CT in detecting regional respiratory distribution [24-27].

Positive quantitative data correlation can be observed between VRI and lung diseases such as smoking index [23], the build-up of excess fluid between layers of the pleura outside the lungs (pleural effusion) [22], and the presence of tumours pressing on the airway [22]. Alterations in lung function produce a different sound transmission. "Normal" and "abnormal" lung sound frequencies and amplitude (intensities) containing spatial information can be captured with acoustic sensors, such as MEMS microphones, and digital stethoscopes. However, the challenges faced by the VRI, which converts lung sound into imaging, is that no positive correlation between VRI's quantitative data and airway obstruction was established, such as asthma [22] and chronic obstructive pulmonary disease

(COPD) [28]. VRI requires additional equipment, such as a vacuum for the acoustic sensors, inconveniencing doctors and patients. VRI also requires a controlled environment (noise-free); however, the ideal controlled environment is not always present and practicable, such as at home or in a clinical setting. Hence, accurate representation of captured lung sounds for subsequent acoustic imaging conversion for lung function assessment still needs to be developed significantly [29]. Thus, a need has risen for portable devices to capture acoustic lung sounds with better accuracy and lower cost than the digital stethoscope to monitor lung function by locating airway obstructions (nidus). Moreover, the design of acoustic imaging devices, including the sensor number and sensing diameter, has traditionally been empirical, which makes acoustic imaging for pulmonary diagnosis hard [22, 30, 31].

The suitability of acoustic imaging to provide an early and continual assessment of lung functions and enable smart airway therapy via targeting affected lung regions, particularly when movement is restricted in the community, and the limited accessibility to the equipment needs to be identified. A need to determine if the detection of ventilation distribution, such as airflows in the airways, can evaluate structural abnormalities and assess functional characteristics through imaging is required. Hence, studying the airway through mathematical modelling and acoustic sensor array design simulation of an acoustic imaging system is critical. To the author's best knowledge, no studies provide an acoustic imaging correlation between the visualisation and quantification of airway remodelling with respiratory diseases such as asthma and COPD. Furthermore, with numerical modelling and simulation, the system design, sensor numbers, and the position of sensors on the patients can be optimised. Lung sounds can be translated into acoustic imaging as an alternative to standard imaging to assess lung function frequently for improved therapy efficiency; thus, acquiring robust lung signals is vital for the accurate assessment of lung functions. Currently, VRI uses a conventional bandpass filter to reduce ambient noise, requiring a prior diagnosis of lung functions to eliminate much of the ambient noise. Conventional bandpass-filtered signals may still contain noise that can influence lung imaging assessment precision. Hence, reducing external interference without removing critical frequency information on the captured lung sound signals is essential, as noise-free environments are impractical, especially in urban or home settings. Lastly, the proof-of-concept of the design and implementation of a wearable, without the need for additional equipment, robust lung sound acquisition and image system using MEMS microphones that reduce external noise contamination through hardware redesign and signal processing is required.

1.2 Purpose of the Research

This thesis aim is to help patients and clinicians assess lung function early, frequently and gain knowledge of lung conditions that leads to an optimised therapeutic treatment. The optimised therapeutic treatment is defined as enabling smart therapy by focusing on the location of obstructed lung region and reducing the therapy duration. Thus, capturing accurate lung sound data and presenting accurate acoustic images of lung function through a simple-to-use, non-invasive, affordable biometric sensor is vital in this thesis. The application criteria are 1) Non-ionising radiation sensing technologies to reduce the health risk involved with ionising radiation sensing systems for daily regional assessment of lung function and optimal therapy parameters; 2) Portable, home-based usage and equipment-to-patient approach which can prevent cross-contamination, save travelling time and patient preparation, and the number of visits to medical facilities; and 3) An assessment tool through imaging that non-trained healthcare personal can understand the assessment results, e.g., a healthy lung showing darker intensity lung image, and lighter intensity lung image correlates to the unhealthy lung. The following objectives are investigated to achieve these aims:

i) Evaluate the suitability of mapping lung sound distribution in the airway for early, frequent, and continual lung function assessment, leading to optimised home care respiratory therapy.

ii) Establish the sensitivity of the acoustic lung signals and imaging to airway pathology.

iii) Examine the feasibility of acoustical lung imaging via an array of acoustic sensors capturing lung sounds at various chest wall locations concurrently, in particular the number of sensors and the sensor sensing area.

iv) Develop affordable and robust electronic instrumentation and signal analysis methods required for non-invasive measurement of the transmission of airway frequency signals and converting the signal into imaging for lung function assessment, in particular locating of the nidi.

1.3 Key Contributions

The following approaches are performed and proposed in this thesis to accomplish the aims and objectives in addressing challenges in the assessment of lung functions via lung sounds and acoustic imaging:

1) The aptness of the equipment/hospital-to-patient approach – bedside, portable acoustic imaging to provide an early and continual assessment of lung functions, enable targeted airway therapy, namely when movement is restricted in the community, and the limited accessibility to the equipment is demonstrated.

   To the best of the author's knowledge, most reviews have focused on the traditional patient-to-equipment approach measuring lung function and mainly on a non-acoustic approach. Prior research on the possibility of bedside or portable acoustic imaging delivering comparable outcome measures to those patient-to-equipment/hospital approaches has not been examined extensively. Furthermore, no approach has been shown to be better than another. The systematic review findings have identified opportunities to develop further acoustic imaging technology approach that is better than the current one. The systematic review is presented in Chapter 2.

2) A novel acoustic lung model [3, 8, 9] incorporating spatial location with airway input parameters flexibility is developed. A new and effective method for assessing lung function with acoustic imaging was presented, which links acoustic lung images with pathologic changes utilizing acoustic imaging simulation. Additionally, the model provided design guidelines for acoustic imaging systems, or served as a performance assessment of already-in-use multimicrophone array-based acoustic imaging systems.

   To the best knowledge of the author, locating nidi through an acoustic lung model and the resulting acoustic lung imaging have yet to be performed. Thus, a novel spatial-based network of the respiratory system modelling is explored, and sensor array design studies through acoustic lung imaging based on the model are conducted. The study results in a framework for the optimisation of the HFCWO therapeutic technique that has shown: 1) The acoustic relationships and imaging characteristics between the sensing system and the location of nidus; and 2) How the sensor numbers and sensor sensing sensitivity affect the image dynamics at various locations within the chest area. The potential of assessing lung function with acoustic imaging has been validated through respiratory remodelling and obtained a similarity of about 89% compared to the acoustic image initiated from actual lung sound signals. The structural similarity (SSIM) index was used to measure the pixel quality and structural similarity between the reference and the acoustic image output, in

terms of the image contrast, the brightness and the structure terms, similar to the utilisation in the medical acoustic image analyses [32, 33]. The SSIM index [34] ranges from 0 to 1, where 0 indicates no similarity between the reference and the acoustic image output, and 1 denotes identical images [32-34]. Simulation studies based on the model are used to analyse the practicality and the extreme design of the acoustic imaging system on the resolution of the located nidus. For instance, a practical system design with sensor numbers between 35 and 4 may recognize nidus lengths between 22 and 73 mm. On the other hand, an extreme system design with more than 1000 sensors can recognize greater nidus resolution at under 10 mm. Additionally, this research may be utilised to offer recommendations for acoustic imaging system design and assess the number of sensors and sensing diameter in current acoustic imaging systems. Furthermore, the geographic detection of nidus length allows for analysing of HFCWO therapy results. The acoustic lung spatial model and the design of an array of acoustic sensors through numerical simulation are detailed in Chapter 3.

3) A unique and ideal integration of wavelet-based total variation (WATV) and empirical Wiener denoising method (WATV-Wiener) is proposed [2, 6, 7] to significantly enhance the signal-to-noise ratio (SNR) while preserving the characteristics of a lung sound signal. An intensive analysis of selecting and fine-tuning the WATV-Wiener filter parameters was demonstrated through simulation studies and case studies instead of the typical parameters' approximation approach. In the simulation and experimental studies, the WATV-Wiener filter obtained a mean 13.54 ± 4.76 dB improvement in SNR and optimal root mean square error (RMSE).

The denoising filter is vital for systems that map lung sound distribution into images, as the accuracy and quality of acquired lung sounds affect the lung function assessment result. Furthermore, a controlled (noise-free) environment for capturing lung sound signals is impractical. To the author's best knowledge, the combination and integration of WATV and the Wiener filter has not been investigated. The WATV-Wiener filter is detailed and presented in Chapter 4.

4) A wearable, extensible, and robust lung sound acquisition and acoustic imaging system, overcoming current digital stethoscopes' limitations and producing more accurate acoustic images for continual lung function assessment, was constructed for continual and reliable lung function assessment [5, 10]. The design and

implementation of a cheap yet robust lung sound acquisition system using MEMS microphones that reduce external noise contamination through redesigned hardware and signal processing is detailed and demonstrated in Chapter 5. RMSE and SNR, reflect the accuracy in capturing desired signals and signal quality to noise contamination. The proposed system's lung signal acquisition unit outperforms commercial digital stethoscopes, in a noisy setting, regarding RMSE by around 0.15 and SNR by around 8 dB. Regarding sensing sensitivity power spectrum mapping, the proposed system sensors' position is neutral when representing lung signals, with a signal power loss ratio of around 5 dB compared to 10 dB from digital stethoscopes. The proposed system obtains about 10% better accuracy detection of the actual nidi length than digital stethoscopes.

To the best knowledge of the author, the proposed system, comprising various sensing and functional components, including an onboard computer and an array of daisy-chained MEMS microphones packaged into a standalone or wearable mobile device for the assessment of lung function via acoustic imaging translated from lung sounds captured from the array of MEMS microphones have not been investigated. The proposed system is low-cost, ranging from USD 120 to 280, for a typical 12 to 24 acoustic sensors array [21, 24, 30, 31, 35, 36] recording lung sound simultaneously at different locations, as compared to digital stethoscopes [37, 38] USD 300, with only single data point collection.

1.4 Thesis Outline

A systematic review methodology was utilised in Chapter 2 to identify the answer to the research motivation, i.e., the aptness of the acoustic imaging system to provide an early and accurate assessment of lung conditions, can the approach or system be used as a continuing lung function assessment tool to enable smart therapy for patients by providing the location of nidus? A thorough literature search was conducted with six established databases: Scopus, PubMed, ScienceDirect, Web of Science, SciELO Preprints, and Google Scholar. Studies shortlisted for review were based on the eligibility requirements specified by SPIDER (Sample, Phenomenon of Interest, Design, Evaluation, Research type). 15 studies remained for additional examination after the screening process in the updated 2020 preferred reporting items for systematic reviews and meta-analyses (PRISMA 2020). The methodological quality of the included studies was evaluated using a modified version of the Newcastle-Ottawa scale (NOS) for evaluating quality in outcome studies. Factors found

in the included studies were grouped into categories based on outcome measures and the technologies used as a reference.

Chapter 3 develops an airway model for the feasibility study in locating nidus via acoustic imaging, and the impact of the number of acoustic sensors and the sensor sensing sensitivity on the imaging through simulation and modelling study. There is currently no gold standard concerning acoustic imaging, no technologies have shown to be better than another for locating or measuring nidi regionally and frequently, as highlighted in Chapter 2. The proposed airway model was further employed to evaluate new or existing acoustic imaging systems due to the flexibility in the airway input parameters and the sensor array design.

Chapter 4 focuses on developing a unique denoising filter to enhance the captured lung sounds for accurate representation and the nidi location, as the airway modelling study in Chapter 3 is based on noise-free airway signals. Captured lung signals often contain interference as a controlled environment for capturing lung sound signals is not practical, leading to inaccurate lung health assessments. Artefacts may be introduced when an unsuitable denoising filter is applied, particularly in the lung sound signals domain. Hence, the WATV-Wiener filter is introduced to denoise noisy lung sound signals and present an accurate representation of desired lung sound signals regardless of noise variance in the surrounding. The WATV-Wiener filter performance is analysed by applying onto different one-dimensional (1D) actual lung sounds of different noise levels.

A low-cost yet robust wearable lung sound acquisition system that enhances signal sensing and acoustic imaging for lung function assessment via hardware and software development was demonstrated in Chapter 5. The system consists of an array of daisy-chained high SNR ICS-52000 MEMS microphones and an Arduino Teensy 3.6 microcontroller that is compact and reconfigurable. The design flexibility allows real-time changes to signal processing and usability features to be applied on the same system. The lung signals acquired from the MEMS microphones were transferred to the microcontroller via flexible printed circuit cables and to the computer via a flat data cable for data analysis and denoising with the proposed filter in Chapter 4, as the captured signals can contain significant noise. The system was evaluated against commercially available digital stethoscopes for signal qualities and sensor sensitivity area, in a noisy setting to imitate actual recordings and via a customised lung sound simulator to remove ambiguity in the results. The system was also evaluated for the presentation of acoustic imaging in locating the nidi.

Chapter 6 summarises the accomplishments of the thesis and reflects upon the best practices for future development.

Chapter 2   Acoustic Lung Imaging Utilised in the Frequent Assessment of Lung Function in Patients with Obstructed Airway: A Systematic Review

The systematic review is the foundation of evidence-based medicine and healthcare, giving the opportunity to combine data scientifically [39, 40] to improve the consistency of results, thus contributing to and enhancing doctors' and clinicians' decision-making, i.e., what works and works that has potential and requires further research. Systematic review systematically assesses and reviews current knowledge, reduces bias, and helps establish the knowns and unknowns through quality assessment of data presented in the subject area of interest. A systematic review is a reproducible approach to identifying research gaps as the data, including the search, are documented at every review step.

Chapter 2 is reproduced* from [4], where the thesis author is the main author of the paper. Chapter 2 is organised as follows. Section 2.1 is the introduction. Section 2.2 describes the methodology used in the literature review. The results, discussions and summary are presented in Section 2.3, Section 2.4, and Section 2.5, respectively.

2.1 Introduction

Respiratory diseases such as asthma, bronchitis, COPD, COVID-19, and pneumonia are the most common cause of obstruction in airways that affect the lung, leading to chest pain, shortness of breath, coughing, and mucus production [41-44].

Respiratory therapy enhances the mobilization of mucus in the lung to reduce airway resistance and improve breathing [45]. E.g., an HFCWO device is used to lower the mucus viscosity through percussion and vibration on the chest and creates the coughing action, which helps to eject the mucus from the airway [45-47]. HFCWO device has been enhanced over the year, such as integrating electronic control for specified pressure oscillating discs to deliver palpitation directly to targeted chest areas [46, 47]. Thus, frequent regional assessment of lung function is imperative [48] to enable smart respiratory therapy and delivery of efficient treatment, such as targeting affected airways and adjusting the therapy

---

parameters promptly to optimise and reduce the duration for patients with respiratory diseases.

Traditional lung function assessment, such as chest X-ray, CT, and magnetic resonance imaging (MRI), have the advantages of high-resolution imaging, but they are patient-to-equipment approaches, unsuitable for frequent assessment due to the ionizing radiation effect on the patient's health [49, 50] and pose having the risk of transporting patients to the equipment in the clinical setting [51, 52]. The lack of equipment accessibility, especially in small communities during the recent COVID-19 outbreak, where movement restrictions added to the disadvantage of the patient-to-equipment approach [53]. The advances in the nonionizing acoustic approach to the lung function assessment have enabled the equipment-to-patient (bedside/portable) approach and frequent lung function assessment [29, 54], where obstructed airways affect sound transmission (acoustic signals) routes and have spectral and regional impacts that can benefit from several measurements over the chest area [29, 55].

To date, reviews on lung function assessment have a broad focus [29, 56-61]. E.g., Rao et al. [29] reviewed different types and approaches of acoustic outcome measures on lung functions. Kolodziej et al. [56], Ramsey et al. [57], and Dubsky et al. [58] reviewed patient-to-equipment approaches that require patient preparation and mainly non-acoustic approaches. Lauwers et al. [59] reviewed multidisciplinary outcome measures that were utilised to evaluate the respiratory therapy effectiveness in participants below the age of eighteen with COPD. Augustin et al. [60] and Oliveira et al. [61] concentrated on the patient-based reported outcome, such as the patient's quality of life. To the author's best knowledge, previous studies on the potential of bedside/portable acoustic imaging to achieve similar outcome measures as those patient-to-equipment approaches have not been systematically reviewed. Hence, the systematic review aimed to answer the following research question: can equipment-to-patient acoustic imaging be used as a continuing lung function assessment tool, enabling smart therapy for patients with respiratory diseases?

2.2 Methods

This systematic review was reported according to the updated Preferred Reporting Items for Systematic Reviews and Meta-Analyses 2020 (PRISMA) guidelines [62], and the checklist can be found in [4]. The systematic review was conducted as per the registered PROSPERO protocol record (CRD42023417131), accessed on 18 May 2023, https://www.crd.york.ac.uk/PROSPERO/display_record.php?RecordID=417131.

2.2.1 Search Strategy and Study Selection

The search strategies were constructed a priori using different terms relating to continuing beside/portable acoustic imaging on regional lung health/function. A thorough description of the search strategy and terms are shown in Appendix A1. The literature search was performed between 31 March 2023 and 14 April 2023. The terms used in the search were defined based on the critical elements from the SPIDER (Sample, Phenomenon of Interest, Design, Evaluation, Research type) model, as the SPIDER model is suitable for a qualitative evidence-based systematic review [63, 64]. Suitable keywords were selected, e.g., patients with obstructed airway or CRD refer to S (sample), PI (the phenomenon of interest) relates to the bedside/portable acoustic images, D (design) is the published literature of any research design, E (evaluation) is referenced to the assessment tool characteristics and, R (research type) connects to qualitative, or quantitative, or both research studies types. To be as inclusive as possible and in addition, the review questions did not have a specific study methodology; hence, D (design) and R (research type) elements of SPIDER were excluded from the keywords selection. The search was conducted by one reviewer (the author) from the following reference databases published in English: Web of Science, PubMed, ScienceDirect, Scopus electronic database, Google Scholar, and SciELO Preprints. No restriction on publication date, and participant's age, while conference proceedings and studies on animals were excluded. 30% of the identified records from the database, randomly selected, were evaluated by a second reviewer (author's industry supervisor Y.L.). Four disagreements were discussed and resolved with consensus between the two reviewers.

2.2.2 Data Collection and Synthesis

Titles and abstracts were screened at the first stage. In the second stage, the introduction was reviewed to ensure that the selected studies' objectives fit the research question. A full-text review and possible potential papers from the shortlisted studies' reference list were performed in the third stage. The corresponding and first author of the shortlisted papers were used to avoid introducing bias, double counting, and possible duplicate publications from the same group. Two reviewers (the author and Y.L.) extracted relevant data from the studies included in the qualitative synthesis and review using a customised spreadsheet containing study variables: author and the year of publication, study design, study population, technique, measured respiratory disease, recording venue, and the significant outcome. Any data discrepancies or disagreements were discussed and resolved with consensus with the author's primary research supervisor and, if necessary, the author's

secondary research supervisor. There was complete agreement between the two reviewers in terms of data extraction. Key outcomes in this systematic review refer to the individual-identified studies reporting statistically significant ability to perform home-based or bedside assessment of lung function, regardless of the statistical analysis used. Meta-analyses were not performed as the studies were conducted in various populations and used varied definitions and statistical analysis on the measure of lung health/function outcomes; therefore, appraisals and findings of each study were given independently.

2.2.3 Risk of Bias

Different risk of bias tools exists for different study types, such as Cochrane risk of bias (RoB) for randomised trials and National Institutes of Health quality assessment tools for controlled intervention studies [65]. An adapted form of the Newcastle-Ottawa Scale (NOS) [65-67] for cross-sectional studies were utilised in this review as the studies selected for quality review and synthesis were purely cross-sectional studies. Each reviewer graded each item based on the information provided in the articles. Item 1 has a maximum of 5 stars, and was graded with stars if the sample size truly represented the average target population or somewhat representative of the average in the target group, justified sample size, the response rate is satisfactory, and measured with a validated measurement tool. Item 2 has a maximum of 2 stars, was graded with stars if the confounding factors were controlled, and study control for any additional factor. Item 3 has a maximum of 3 stars; 2 stars were graded if the outcome is assessed by independent blind assessment or record linkage, and 1 star for self-report and statistical analysis was not used. Each study's quality score was determined as the sum of all scores, ranging from 0 to 10 points, with higher scores indicating higher quality. In addition, for a fair review, no weighting was applied as any possible area for bias to be more crucial than another was considered. Two reviewers (the author and Y.L.) independently assessed the risk of bias with the NOS tool for each included study. There is no disagreement between the two reviewers with regard to the quality assessment of the included studies. The details of the quality assessment are presented in Appendix A2.

2.3 Results

2.3.1 Study Selection

The electronic database search yielded 496 papers, and 14 papers were identified from cross-reference and citation. 153 records were screened after duplicates were eliminated, of which 17 were assessed in full text. After the review process presented in Figure 2.1, 2 papers were

excluded due to the unavailability of the full text. The study selection process led to 15 studies, which were included in the review for quality assessment and synthesis of results.

Identification of studies via databases and registers

Identification

Records identified from databases and registers (n = 510):
Databases (n = 496)
- Scopus (n = 92)
- PubMed (n = 4)
- ScienceDirect (n = 346)
- Web of Science (n = 30)
- SciELO Preprints (n = 0)
- Google Scholar (n = 24)
Registers (n = 14)
- Additional records identified through cross reference and citation

Records removed *before screening*:
Duplicate records removed (n = 357)

Screening

Records screened (n = 153)

Records excluded on the basis of title, and authors (n = 136)

Reports sought for retrieval (n = 17)

Reports not retrieved (n = 0)

Reports assessed for eligibility (n = 17)

Reports excluded (n = 2):
Identifying only the types of diseases, medicine treatment, or the needs of therapy.
(n = 0)
Unavailability of full text articles (n = 2)

Included

Studies included in qualitative synthesis and review (n = 15)

Figure 2.1   PRISMA 2020 flow of information for studies selection and inclusion

2.3.2 Study Characteristics

Table 2.1 narrates each of the selected studies in terms of study design, study population, approach, diseases, venue of the assessment, and the primary outcome of the techniques in terms of lung health. These 15 studies from Table 2.1 were conducted on patients with obstructed airways relating to respiratory diseases and were cross-sectional studies. 5 studies [21, 68-71] focused on patients with CRD, while 6 studies [35, 72-76] reported on patients with lung consolidation, and the remaining 4 studies [77-80] investigated on COVID-19

patients. 8 studies [68, 71, 72, 74, 77-80] utilised LUS and the remaining 7 studies [21, 35, 69, 70, 73, 75, 76] utilised VRI technology as observed in Table 2.1. The total number of participants per study ranged between 10 and 219. The study population inclines slightly towards males (684/1190) at about 57%. 3 studies [72, 74, 79] were experimented on children below the median age of 13, 4 studies [68, 69, 75, 77] investigated on elderly above the median age of 60, and the remaining 8 studies [21, 35, 70, 71, 73, 76, 78, 80] tested on adults between the median age of 13 and 60.

Author (year)	Study design	Sample population	Technique	Venue	Diseases	Outcome
Jambrik et al. [68] (2004)	Cross-sectional	n = 121 Female: 43 Male: 78 Age: 67 ± 12	LUS	ICU	Chronic pulmonary disease.	Pulmonary abnormalities.
Dellinger et al. [69] (2007)	Cross-sectional	n = 38 Female: 24 Male: 14 Age: 60 ± 16	VRI	ICU	Chronic pulmonary disease	Geographical lung area and sound energy change.
Anantham et al. [75] (2009)	Cross-sectional	n = 56 Female: 23 Male: 33 Age: 68 ± 13	VRI	CE	Pleural effusion	Bilateral effusion.
Guntupalli et al. [70] (2009)	Cross-sectional	n = 66 Female: 32 Male: 34 Age: 56 (Median)	VRI	Hospital	Asthma, COPD	Geographical lung area and sound energy change.
Lev et al. [35] (2010)	Cross-sectional	n = 82 Female: 57 Male: 25 Age: 59 ± 19	VRI	ICU	Consolidation, congestion, pleural effusion, atelectasis	Geographical lung area and sound energy change.

Table 2.1   The findings of the included study characteristics.

Author (year)	Study design	Sample population	Technique	Venue	Diseases	Outcome
Bing et al. [21] (2012)	Cross-sectional	n = 36 Female: 12 Male: 24 Age: 58.34 ± 14.72	VRI	Outpatient clinic and ICU	Acute exacerbation of COPD.	Geographical lung area and sound energy change.
Liu et al. [76] (2014)	Cross-sectional	n = 23 Female: 10 Male: 13 Aged: 56 ± 2	VRI	CE	Idiopathic pulmonary fibrosis	Geographical lung area change.
Ambroggio et al. [74] (2016)	Cross-sectional	n = 132 Female: 58 Male: 74 Age: 4.4 (Median)	LUS	Hospital	Pneumonia, wheezing, bronchiolitis, pleural effusion	Lung consolidation.
Gorska et al. [71] (2016)	Cross-sectional	n = 60 Female: 28 Male: 32 Age: 31-72	LUS	Outpatient clinic	Asthma, COPD	Geographical bronchial wall thickness change.
Jiang et al. [73] (2017)	Cross-sectional	n = 62 Female: 28 Male: 34 Age: 43.12 ± 13.64	VRI	CE	Pneumonia	Sound energy change.
Chen et al. [77] (2020)	Cross-sectional	n = 51 Female: 23 Male: 28 Aged: 61 (Median)	LUS	Hospital	COVID-19, other respiratory symptoms	Geographical lung intensity change.

Table 2.1 (Continued)   **The findings of the included study characteristics.**

Author (year)	Study design	Sample population	Technique	Venue	Diseases	Outcome
Giorno et al. [78] (2020)	Cross-sectional	n = 34 Female: 13 Male: 21 Age: 13 (Median)	LUS	Hospital	COVID-19	Geographical lung intensity change.
Musolino et al. [79] (2020)	Cross-sectional	n = 10 Female: 4 Male: 6 Age: 11 (Median)	LUS	Hospital	COVID-19	Geographical lung intensity change.
Ruiz et al. [72] (2020)	Cross-sectional	n = 200 Female: 84 Male: 116 Age: 0.4 (Median)	LUS	Hospital	Bronchiolitis	Pulmonary abnormalities.
Rizzetto et al. [80] (2021)	Cross-sectional	n = 219 Female: 67 Male: 152 Age: 58 (Median)	LUS	Hospital	COVID-19	Geographical lung intensity change.

Abbreviations: CE, controlled environment; ICU, intensive care unit; LUS, lung ultrasound.

Table 2.1 (Continued)   **The findings of the included study characteristics.**

Positive observation of either change in geographical lung area or sound energy, or both, was the most common outcome obtained by 11 studies [21, 35, 69-71, 73, 76-80]. The remaining 4 studies [68, 72, 74, 75] reported positive observations of lung consolidations. 12 studies [21, 35, 68-72, 74, 77-80] performed the assessment at an uncontrolled environment such as hospital, ICU and clinics, while, the remaining 3 studies [73, 75, 76] performed the assessment at a controlled setting. 8 studies [35, 68, 71, 74, 75, 77, 78, 80] compared lung assessment from two different techniques. 1 study [35] compared VRI with

chest X-ray, 1 study [75] compared VRI with LUS, 2 studies [68, 74] compared LUS with chest X-ray, and the remaining 4 studies [71, 77, 78, 80] compared LUS against CT.

2.3.3 Quality Scores in Individual Studies

The quality assessment of individual studies is summarised in Table 2.2. The 15 selected studies scored in the range of 5 to 9 using an adapted form of NOS for cross-sectional studies, where studies were classified as unsatisfactory studies (0–4 points), satisfactory studies (5–6 points), good studies (7-8 points), and very good studies (9–10 points) [67, 81]. From Table 2.2, 2 studies [68, 80] were identified as very good studies, 9 studies [35, 70-75, 77, 78] were determined as good studies, while the remaining 4 studies [21, 69, 76, 79] were satisfactory. None of the selected studies was unsatisfactory.

Study ID	Selection (5)				Comparability (2)	Outcome (3)		
	Trait of the sample	Sample size	Non-responds	Determine of the exposure (risk factor)	Comparability of subjects in different outcome groups based on design or analysis.	Analysis of outcome	Statistical test	Total (10)
Jambrik et al. [68] (2004)	★		★	★★	★★	★★	★	9
Dellinger et al. [69] (2007)	★		★	★	★	★	★	6
Anantham et al. [75] (2009)	★		★	★	★★	★	★	7

Table 2.2 **Quality assessment of included studies using Newcastle-Ottawa scale adapted for cross-sectional studies.**

Study ID	Selection (5)				Comparability (2)	Outcome (3)		
	Trait of the sample	Sample size	Non-responds	Determine of the exposure (risk factor)	Comparability of subjects in different outcome groups based on design or analysis.	Analysis of outcome	Statistical test	Total (10)
Guntupalli et al. [70] (2009)	★		★	★	★	★★	★	7
Lev et al. [35] (2010)	★		★	★	★★	★	★	7
Bing et al. [21] (2012)	★		★	★	★	★★		6
Liu et al. [76] (2014)	★		★	★	★	★		5
Ambroggio et al. [74] (2016)	★		★	★★	★	★★	★	8
Gorska et al. [71] (2016)	★		★	★★	★	★★	★	8
Jiang et al. [73] (2017)	★		★	★	★	★★	★	7

Table 2.2 (Continued)   Quality assessment of included studies using Newcastle-Ottawa scale adapted for cross-sectional studies.

Study ID	Selection (5)				Comparability (2)	Outcome (3)		
	Trait of the sample	Sample size	Non-responds	Determine of the exposure (risk factor)	Comparability of subjects in different outcome groups based on design or analysis.	Analysis of outcome	Statistical test	Total (10)
Chen et al. [77] (2020)	★		★	★★	★	★★	★	8
Giorno et al. [78] (2020)	★		★	★	★	★★	★	7
Musolino et al. [79] (2020)	★		★	★	★	★	★	6
Ruiz et al. [72] (2020)	★		★	★★	★	★★		7
Rizzetto et al. [80] (2021)	★		★	★★	★★	★★	★	9

NB, the numbers in parenthesis are maximum scores to be given per category.

Table 2.2 (Continued)   Quality assessment of included studies using Newcastle-Ottawa scale adapted for cross-sectional studies.

2.3.4 Results of Individuals/Synthesis

From the synthesis of the shortlisted studies in Table 2.1, LUS [68, 71, 72, 74, 77-80] and VRI [21, 35, 69, 70, 73, 75, 76] are the main techniques that utilised acoustic signals and translated the signals into imaging for frequent bedside/portable assessment. The synthesis results are presented according to the type of outcome measure, with further divisions made based on the compared factors and technologies.

2.3.4.1 LUS

LUS images are based on sound propagation in the matter and sound wave interaction with reflecting interfaces [82]. LUS has made significant progress in evaluating lung pathologies in the last two decades, non-invasive, non-ionising, and safe to repeat the lung function assessment at the patient's bedside numerous times, leading to the reduction of chest X-rays and CT examinations [82, 83]. LUS has also been considered in the emergency setting, such as the pulmonology and thoracic surgery ambulatory clinics [82, 83].

2.3.4.2 LUS Against Chest X-ray

LUS demonstrated statistical equivalent to chest X-ray in detecting respiratory diseases such as lung consolidation and pleural effusion from 50 patients' results, in terms of sensitivity [74]. The radiologic chest X-ray score of extravascular lung consolidation had a substantial linear connection with the LUS echo comet score from 135 images [68]. A significant correlation was found with regard to lung consolidation when the radiologic chest X-rays score was compared with the LUS echo comet score of a single chest intercostal space, specifically on the right side at the third intercostal space on the anterior axillary line [68]. Hence, compared to chest X-rays, LUS can demonstrate statistically equal sensitivity for respiratory findings, such as CRD, pleural effusion, and lung consolidation [68, 74].

2.3.4.3 LUS Against CT

The sensitivity and specificity of lung ultrasound (LUS) for each patient's distinct lung zones were evaluated using chest CT findings as a reference, as CT is the gold standard for evaluating pulmonary abnormalities [71, 77, 78, 80]. The LUS data from 219 patients achieved an overall sensitivity and specificity of 75% (1348/1801) and 66% (549/827), respectively, with CT findings as a reference [80]. LUS was able to identify the differences in the airway wall thickness, statistically comparable to CT from 60 patients' data, and better visualization when compared against the healthy group [71]. The LUS score and CT had a strong correlation, where 37 patients (72.5%) from CT scans were suggestive of COVID-19 or had radiologic symptoms, while LUS exams suggested 40 patients (78.4%) [77]. With a sensitivity of 100%, specificity of 78.6%, positive predictive value of 92.5%, and negative predictive value of 100%, LUS was accurately diagnosed in all 37 patients with abnormal findings on CT [77]. With LUS compared to CT, there were no missed diagnoses of COVID-19 in the group [77]. Similar to [77], when compared to CT, LUS demonstrated statistical equivalent in detecting COVID-19 and lung abnormalities from 12 patients' data [78].

2.3.4.4 VRI

VRI [21-23] has been proposed to monitor respiratory distribution within the lungs dynamically and is regarded as an electronic stethoscope alternative which records vibration emitted from the chest using an array of microphones and converts them into grey-scale images. The hypothesis is that when there are changes in airflow in the lungs, frequency, and intensity, these changes will affect the lung vibration response images [21-23]. The contact sensors on the posterior of the patient's chest wall will simultaneously record 12 to 20-second sound clips. The assumption is that the array of sensors utilized covers the chest posterior fully, including the traditional auscultation area performed by clinicians and doctors, and the nidi location can be identified by comparing energy recorded from the individual sensors. The recordings are converted into digital signals and filtered through a bandpass filter to minimise artifacts such as sounds produced by the environment and heart. The filtered output signal combined with an interpolating function is expressed as an image of breath sound intensities between measured locations and the microphone's location on the chest wall concerning time [22]. VRI images are scored based on the image quality, intensity of the vibrational energy curve, abnormal signs in the image output: unsmooth, inspiratory steep, spike, step, dynamic image, image movement during breathing phases, and maximal energy frame shape. Thus, VRI technology is an excellent way to detect lung sound distribution during mechanical ventilation in several studies [21, 23, 84].

2.3.4.5 VRI Against Chest X-ray

4 individuals with pneumonia but no consolidation had lower vibration intensity than 13 patients with pneumonia plus consolidation (8 ± 14 vs 22 ± 29 x 10^6 AU) [35]. The consolidation identified by chest X-rays overlaps with the increased vibration intensity area, which is represented by darker colours in VRI [35]. This great intensity overshadows the appearance of the left lung due to normalization [35]. The vibration intensity difference between freely breathing and mechanically ventilated patients was significant [35].

2.3.4.6 VRI Against LUS

In the per-patient study (45 cases), VRI can accurately (45/56, 80%) identify the proper diagnosis (right, left, or bilateral effusion) [75]. In the per-hemithorax study, the agreement between the VRI recording and the chest X-rays on the amount of effusion was 74% (83/112) [75].

2.4 Discussion

While exposing patients to unnecessary radiation doses and straining medical resources should be circumvented, clinicians and doctors should consider the assessment of the respiratory system by equipment-to-patient acoustic imaging. A detailed understanding is needed, i.e., potential indication for continual assessment of patients with obstructed airways through acoustic imaging, which can lead to optimal respiratory therapy. Therefore, this systematic review aims to address the capability of acoustic imaging as a home-based and continuous outcome assessment of lung function for patients with obstructed airways. This systematic review identified LUS (8/15 studies) and VRI (7/15 studies) as the implemented approach for home-based/bedside imaging of patients with an obstructed airway. Compared to chest X-rays, LUS and VRI had demonstrated similar accuracy in diagnosing respiratory diseases, particularly pleural effusion and lung consolidation in critically ill patients [35, 68, 74, 83]. Compared to CT, LUS has demonstrated similar reliability in the assessment of (n = 58) COVID-19 patients [77, 78], and has presented the potential to detect changes in the airway thickness in (n = 60) patients with obstructed airway when compared to healthy group [71]. Although there is no comparison between VRI and CT in the shortlisted studies, VRI can accurately (45/56, 80%) identify the correct obstructed region, e.g., right, left or bilateral effusions, when compared to LUS [75]. Table 2.3 offers an overview of the critical factors for the discussed outcome measures.

Since each outcome measure has advantages and unique problems, no perfect approach or one approach that is superior to another could be found. In general, this systematic review summarises a diverse range of investigations conducted over the last two decades. The use of certain outcome measures, study designs, etc., varied widely. Hence, the goal is not to make any claims about ideal acoustic lung imaging but to examine the applicability of various acoustic lung imaging in patients with obstructed airways. Relevant studies were searched in six databases that included a wide range of research articles and a lengthy period, as no restriction on publication timeline for each database was applied to access as much pertinent literature as possible. Precise inclusion and exclusion criteria via SPIDER were utilised regarding the population, exposures, and study outcome. The overall research risk of bias quality was evaluated with an adapted form of NOS.

	LUS	VRI
Approach	Detect the sound wave interaction with reflecting interfaces such as the lung tissue via a specialised probe.	Measures breathing sound distribution in the airway and convert it to vibration energy with an electronic stethoscope/microphone.
Imaging	Maps from the sound propagation that are reflected from the lung tissue or rib cage.	Maps the ventilation distribution into a grayscale figure for lung function assessment
Indications	Assess lung health regionally and globally. Flexible, bedside, and home-based monitoring are possible. Frequent, semi-continuous monitoring due to a nonhazardous approach Comparable assessment outcome of lung function compared to CT and chest X-rays.	Assess lung health regionally and globally. Flexible, bedside, and home-based monitoring are possible. Frequent, semi-continuous monitoring due to a nonhazardous approach. Maps the vibration energy with one planar posterior measurement. Good correlation of lung function assessment compared to LUS and chest X-rays.
Disadvantages	Requires specialised training to operate the equipment. Requires trained personnel to interpret the assessment outcome. Assessment outcome may be affected by the patient's body size [82].	Requires a controlled environment and additional equipment, such as a vacuum pump.

Table 2.3   Key considerations for continuing assessment of lung function.

One potential drawback is that the search may have missed certain significant studies due to the language barrier, as only journals that published studies in English were considered. As only two main techniques, LUS and VRI, were reported in this systematic review, and there is limited published research on acoustic lung imaging for patients with obstructed airways, conclusive statements about the ideal technology for the population could not be made. Additionally, as the majority of the included research exclusively addressed continuing lung assessment with acoustic lung imaging on patients with obstructed airways, other patients with tumours, cancer, or a combination of obstructed airways and tumours may find the author's findings less helpful. Because convenient sampling was used to gather the data for this study, it is important to interpret the results carefully. Lastly, this study was not a controlled, randomised experiment. As a result, the reported imaging effects indicated observation and trends in the assessment of lung function.

Two interdependent main areas of interest can be pointed out for future research. The first is the evaluation of acoustic imaging for regional lung assessment patients with obstructed airways. A common trait that can be observed is that LUS and VRI compute the impedance or the resistivity in the lung or the airway as an indicator for lung function assessment and then converts the signal data to an intuitive image or medical image. With the information on the regional lung information, doctors and clinicians could enhance the ACT with timely adjustment. From the 15 selected studies in Table 2.1, LUS and VRI imaging could be a sensitive measure to quantify local and regional changes in lung pathology. Lung sound and vibration energy produced from the chest wall could be transformed into information that presents local ventilation status and could increase future knowledge of the airway therapy's effectiveness. Second, acoustic lung imaging modelling and simulation have not been explored, and the understanding of the sensor's placement, position, and effect on the outcome measure has not been investigated. These methods could reveal important details about the physiological processes that underlie targeted therapies, revealing distinctions between various therapeutic modalities. Computerised lung sound monitoring might be a sensitive approach to evaluate regional changes in the airways brought on by mucus displacement and better regional ventilation.

2.5 Summary

Chapter 2 has described the considerations and limitations of the potential and limitations of bedside/portable acoustic imaging, such as LUS and VRI, in the continual and frequent assessment of lung function to enable targeted respiratory therapy for improving the therapy

effectiveness. LUS and VRI have shown the potential to achieve similar results as the traditional imaging modality with the small number of selected studies in this systematic review. Further acoustic imaging research, especially the direction in converting lung sound into images for assessment, e.g., VRI is required. VRI requires a controlled environment [73, 75, 76] and is deemed not as established compared to LUS, where LUS has been tested in the hospital and ICU setting [68, 71, 72, 74, 77-80] and has been used in the pilot/comparison study for identifying obstructed airway in COVID-19 [77-80]. Since there is no gold standard, e.g., LUS is better than VRI, or vice versa, for measuring the obstructed airway regionally and frequently, VRI has the potential for home-based usage as no medical interpretation of the results is required, unlike LUS, which requires medical interpretation of the results.

To develop an intuitive acoustic lung imaging system by mapping lung sound distribution, locating airway obstruction (nidi), and overcoming challenges faced by existing lung assessment techniques, the detection of ventilation distribution, such as structural abnormalities in the airway, providing a correlation between the visualisation and quantification of airway remodelling with respiratory diseases, and assess functional characteristics through imaging is required. Hence, studying the acoustic imaging system through mathematical airway modelling and acoustic sensor array design simulation is critical. In addition, acquiring robust lung signals is vital for accurately assessing lung functions through imaging. Thus, reducing external inference without removing critical frequency information on the captured lung sound signals is essential, as noise-free environments are impractical, especially in urban or home settings.

Chapter 3 Locating Nidi via Acoustic Imaging of Lung Airways as a Spatial Network

From Chapter 2, many articles have been written on how to measure and determine lung function in the presence of airway obstruction through acoustic imaging. Additionally, outside the medical community, the popularity of numerical computations of the airway is growing [85, 86]. Studies have been performed, and articles are written on numerically determining the flow in the airway, obtaining geometries from CT and MRI scans, analysing the interaction of airflow structures, and acquiring acoustics using probes. However, a numerical method that combines lung function assessment and an interactive computation of airflow structure is not available at this point. The feasibility of lung function assessment by acoustic imaging is going to be investigated to predict output signals generated by the propagation of airflow through the obstructed airway. The inverse problem can be solved if the calculation is shown to be sufficiently accurate. This method can then be used as a tool to predict the approximate location and size of obstruction from the sounds the patient makes when breathing. Hence, the first step in assessing lung functions via acoustic imaging is to develop a lung model.

Chapter 3 is reproduced[†‡] from [3, 8, 9], where the thesis author is the main author of the paper. Chapter 3 is organised as follows. An overview and an incisive review of the airway modelling and the acoustic sensor array design are presented in Section 3.1 and Section 3.2, respectively. The modelling of airways and generation of the acoustic imaging are described in Section 3.3. Model verification by comparing healthy lungs and the lungs with asthma and COPD symptoms is demonstrated in Section 3.4. The simulation studies on locating nidi, sensor distribution, and image resolution are presented in Section 3.5, followed by general discussions in Section 3.6. Lastly, the summary is given in Section 3.7.

---

† © 2023 IEEE. Reprinted, with permission, from [8] C. S. Lee, M. Li, Y. Lou, and R. Dahiya, "Modelling and simulation of pulmonary acoustic signal and imaging for lung function assessment," 2023 IEEE International Conference on Consumer Electronics (ICCE), Las Vegas, NV, USA, 2023, pp. 01-06. [9] C. S. Lee, M. Li, Y. Lou, and R. Dahiya, "The effect of sensor array design on acoustic imaging for enhancing HFCWO therapy," presented at the 2023 IEEE International Multi-Conference on Systems, Signals and Devices (SSD), Mahdia, Tunisia, Feb 22, 2023.

‡ The article is licensed under an open access Creative Commons CC BY 4.0 license. [3] C. S. Lee, Y. Lou, M. Li, Q. H. Abbasi, and M. A. Imran, "Locating nidi for high-frequency chest wall oscillation smart therapy via acoustic imaging of lung airways as a spatial network," in *IEEE Access*, doi: 10.1109/ACCESS.2023.3317443.

3.1 Overview

Chronic inflammation, cystic fibrosis, and some respiratory viral diseases cause mucous discharge to thicken. HFCWO therapy is a common airway clearance technique for patients with thick mucus and low mucociliary clearance (MCC) efficiency. HFCWO devices are defined as small oscillations of mechanical parts at relatively high frequencies (5-20 Hz) applied onto the patient's thorax for respiratory therapy. Traditional HFCWO devices, such as the Vest 105 by Hillrom [47], use an air-filled garment enclosing the patient's chest to generate motion similar to MCC. The parameter setting and operation are purely empirical according to user experience. Modern HFCWO devices such as the Monarch [47], the AffloVest [87], and the RespIn 11 [46] were equipped with multiple electromagnetic/pneumatic actuators that can be controlled individually, enabling a smart therapy that targets the nidus locations for an optimal therapeutic process. Therefore, knowledge of nidus location in the airway is critical.

Chapter 3 presents studies on acoustic imaging to locate nidi to allow inference on the efficiency of HFCWO physiotherapy by respiratory remodelling and acoustic imaging sensor array design simulations. Moreover, the acoustic imaging system setups are typically empirical, potentially leading to unoptimised nidus detection. Hence, the key contributions are: 1) Proposing a realistic 2D acoustic lung model incorporating spatial location to simulate airway obstruction and to design and optimise acoustic sensor array measurements quantitatively [8, 21-23]. 2) Applying the resulting acoustic image from the proposed 2D airway model to theoretical acoustic sensor array design by considering the sensor distribution, sensor sensitivity area, and sensor number.

First, by predetermining the acoustic sensor sensing area, this research illustrates the relationship between the severity of the airway obstruction and mean acoustic image intensity through the thickening of the airway wall thickness (AWT). A good agreement was found between a reference obstructed airway created from lung sound data and acoustic imaging from the developed model, with a SSIM index of 0.8987, with 1 denoting an identical image. Next, different sensor sensing areas are employed to correlate the observed nidus length with the sensor numbers. About 26,000 sensors are required to identify a resolution of 4.35 mm minimal nidus length with a 10 mm sensor sensing diameter. Comparatively, a 50 mm sensor sensing diameter may identify a roughly 73 mm minimal nidus length resolution with only about 4 sensors. The findings support the theory that better image resolution derives from increased sensor numbers. In addition, the required sensor

numbers and sensing sensitivity can be used as a baseline consideration in the acoustic imaging system design. Additionally, a guideline for designing HFCWO devices and assessing the HFCWO therapy efficacy on the patient for a smarter process through therapy feedback from identified nidus length can potentially be provided by understanding how sensor array and sensing sensitivity affects lung health assessment with the resolution of the detected nidus and optimizing the sensor array.

3.2 Acoustic Airway and Imaging Modelling Review

To realise the HFCWO smart therapy, locating nidi is critical, while one of the direct ways to access nidus location is to present on an image.

Chest X-rays, CT, and MRI are the usual imaging techniques to visualise the airways and lung pathology. However, these approaches are not ideal due to their ionising radiation effects and the patient-to-equipment approach [88]. Unlike chest X-rays, CT, and MRI, EIT [89] is an equipment-to-patient approach and uses non-ionising radiation technology that provides alternatives to monitor airways. However, EIT usually provides transverse plane images instead of the required frontal plane images (see Figure 3.1(b)) for the actuator selection or adjustment (see Figure 3.1(a)), making it challenging to apply with HFCWO therapy.
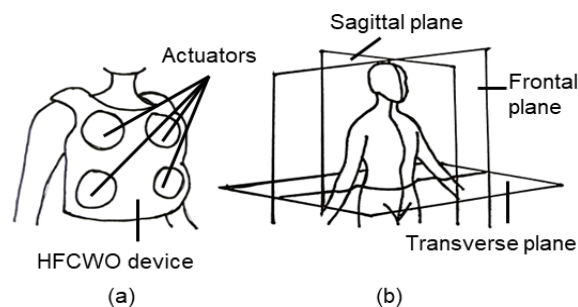
Figure 3.1 **HFCWO device and imaging planes: (a) Typical modern HFCWO device with multiple actuators that can be activated individually for smart therapy, and (b) Anatomical imaging planes.**

In the quantitative forms of lung sound presentation, Kompis et al. [30] developed an acoustic imaging technique that uses simultaneous multimicrophone recordings to assess spatial information. Another technique for converting the acoustic signal to an image is VRI [22]. VRI reflects the dynamic changes in the lung by imaging that utilise the vibration energy created during breathing. By presenting localised information on breath sounds

between different lung sites, the visual representation improves the clinical value [22]. Acoustic imaging and lung disorders, such as smoking index and the accumulation of extra fluid between layers of the pleura outside the lungs, have a positive quantitative data correlation [22]. Computing from the impedance or the resistivity in the lung or the airway through respiratory remodelling as an indicator for lung function assessment is required as an initial step.

Airway obstruction, or the thickening of airway walls in CRD, alter the production and transmission of lung sound spectrally and regionally. Asthma and COPD patients with frequent mucus production in their airways tend to have thicker airway walls than those without, regardless of the severity of breathlessness, and have shown significantly different morphologic airway findings compared to healthy individuals [16]. The change can be measured quantitatively in the lung sound transmission and provide critical information on the disease severity and location of the airway obstruction [11-16]. Spatially distributed airway tree models have been developed to decipher the relationship between bronchi lengths, branching angles, and airway diameters [90]. In the development, Murray's law [91] defined that the relationship between airway bifurcation is fixed, with branch lengths based on a length-to-diameter ratio. Weibel symmetric and Horsfield asymmetric models are the most used conducting airway models [90]. With the advancement of medical imaging techniques, deterministic parameterised bronchial tree generation algorithms were extracted directly from CT, thus constituting the core of patient-specific modelling [90]. The recent works in this area are summarised in [92]. However, those models developed so far are typically simplified to a one-dimensional system of equations to investigate the relationships between healthy and unhealthy respiratory system cycles, such as frequency response, flow rate, resistance, volume, and diagnosis accuracy [11, 90, 93].

Although positive correlation can be identified through acoustic imaging and lung disorders, chronic respiratory diseases, such as asthma and COPD, have not been correlated positively [22, 28]. Moreover, the correlation between acoustic sensors placement and sensitivity were not investigated, and the position of the sensors was typically empirical [22, 30, 31].

3.3 Modelling of Airways and Acoustic Imaging

This research developed a model for acoustic imaging with the following features to improve the investigation of locating airway obstruction, as each patient has a unique set of airway dimensions and structures:

1) The ability to modify the airway input parameters that influence the model's output, such as the wall thickness, length, and diameter, where the patient-centric assessment technique is made possible.

2) The airway model outputs intuitive spatial-based 2D imaging to show airway obstruction in the lung caused by respiratory conditions such as COPD and asthma (Section 3.4).

3) The resolution of the lung image was intended mainly for the assessment and location of the obstruction in the airways due to the limited sensor numbers and HFCWO actuators that can fit onto the patient's posterior chest area (Section 3.5).

Drawing inspiration from [11, 13, 14, 30, 92, 93], the respiratory system is represented as a bifurcating tree network with the linked node of the bifurcating segment and integrated spatial position (x, y) on the airway plane, where the airway plane refers to the three dimensional (3D) airway network space that is projected onto. After that, the network is converted into an electrical network with lumped characteristics and presented as an assessment of the acoustic lung image. In the model development, the following notations are used. $\mathbb{R}$ denotes the set of all real numbers. $\mathbb{R}^{m \times n}$ is the set of all real $(m \times n)$ matrices. $\mathbb{C}$ denotes the set of all complex numbers. $\mathbb{C}^{m \times n}$ is the set of all complex $(m \times n)$ matrices. $\mathbb{Z}(\omega)$ is the set of all sinusoidal variables with angular frequency ω.

The construction of respiratory airway modelling on a single node of the bifurcating airway impedance and the respiratory airway modelling parameter is presented in Section 3.3.1 and Section 3.3.2, respectively. Next, the conversion of the airway impedance into acoustic imaging is presented in Section 3.3.3.

3.3.1 Modelling Respiratory Airway

Each 3D network segment is initially projected toward a 2D plane and given a coordinate for its position (x, y). The respiratory system is thus depicted as a bifurcating tree network, with the joined node of the bifurcating segment at layer k and position (x, y) being indexed by (x, y, k) on the plane illustrated in Figure 3.2(a). Through a recursion index of $\Delta(k)$, the k-th layer segment splits into asymmetrical airways of layers $(k + 1)$ and $(k + 1 + \Delta(k))$ [13]. The airway is then represented as a network of bifurcating cylinders which can be modelled as a transmission line with distributed parameters and further translated into an electrical π

network utilizing lumped parameters, as shown in Figure 3.2(b). The airway network is then resolved by the acoustic pressure at each segment induced by the pressure distribution from bronchi breathing and the airway network [94, 95]. Merging the acoustic power over a predetermined period of time during each breathing cycle, a plane image is generated by the projected network as a subset of the acoustic lung image $Q(x, y) \in \mathbb{R}^{m \times n}$ (discussed in Section 3.3.3).
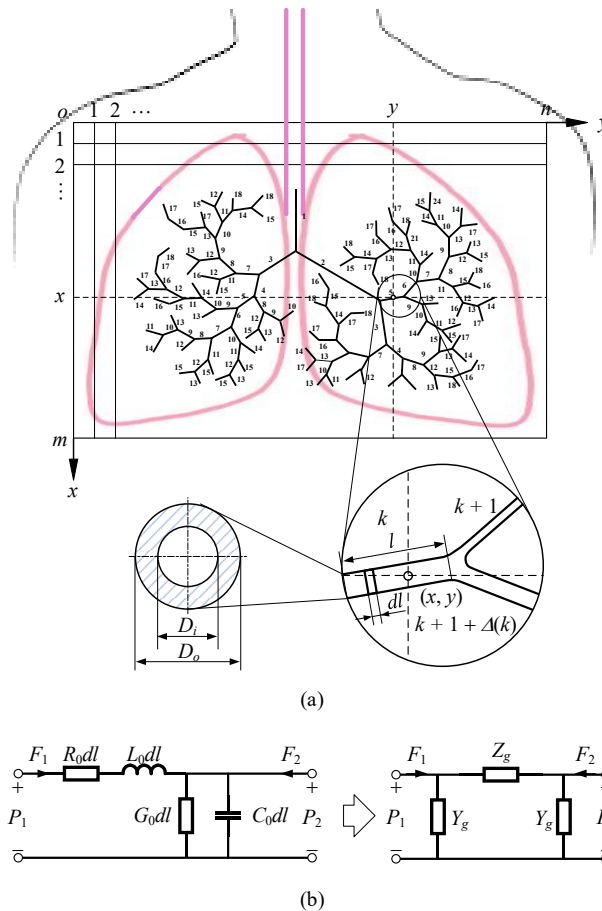
Figure 3.2   Model of human respiratory airway system: (a) airway tree of bifurcating segments, (b) transmission line model of the segment and its equivalent circuit with lumped parameters.

Since the longitudinal motion of the airway is typically negligible in comparison to the acoustic signal [11, 90, 93, 96], the acoustical impedance $Z(\omega)$ and acoustical admittance $Y(\omega)$ averaged over the cross-section of the nonrigid airway segment of Figure 3.2(b) are satisfied by the volume flow rate F and pressure P,

$$\begin{cases} Z(\omega) = F\dfrac{dP}{dl} \\[2mm] Y(\omega) = -P\dfrac{dF}{dl} \end{cases} \tag{3.1}$$

where l is the axial coordinate, and $\omega = 2\pi f$ is the angular frequency (radians/second). When the patient breathes periodically, the airway can be regarded as a steady-state system as the pressure and other velocity components are also periodic, with the same angular frequency ω as the flow due to the periodic airflow rate [90, 93, 96], with each segment as a short nonrigid transmission line tube, with unit-length parameters equivalent analogous acoustic resistance R_0, inductance L_0, capacitance C_0, and conductance G_0 [13]. The velocity in the radial direction (meter/second), and the axial direction (meter/second), and the model wave propagation pressure function, are used, together with all the variables listed in Table 3.2.

In the respiratory system, impedance arises from resistive forces such as elastic forces from tissue compliance, inertial forces from air acceleration, and other factors that oppose breathing in and out. To analyse respiratory impedance in the frequency domain, the time-domain equations modelling pressure $P(t)$ and flow $F(t)$, where t is the time, need to be converted using Fourier transforms, which translates the t time derivatives of pressure P and flow F with terms containing angular frequency ω, allowing the impedance relationships between sinusoidal pressure and flow to be represented in the frequency domain. The modelling and simulation of acoustic impedance measurements were conducted simultaneously to spontaneous breathing as the body produced sinusoidal frequencies are much higher, 400 Hz in this research work, than the typical respiratory rate of 0.25 Hz. Thus, breathing manoeuvre or closure of the airway – for time domain airway modelling, are not required [14, 90, 93, 96, 97]. Refer to [97] and the references within for more in-depth discussion and derivation of time domain airway modelling.

By analogy to the electrical transmission line, the respiratory pressure P, can be considered equivalent to voltage, airflow F as equivalent to current, and the respiratory resistance $\mathbb{Z}$ equivalent to electrical resistances [90, 93, 96], described by,

$$\begin{pmatrix} P_1 \\ F_1 \end{pmatrix} = \begin{pmatrix} \cosh(\gamma l) & Z_c \sinh(\gamma l) \\ \dfrac{1}{Z_c}\sinh(\gamma l) & \cosh(\gamma l) \end{pmatrix} \begin{pmatrix} P_2 \\ F_2 \end{pmatrix}, \tag{3.2}$$

where $P_1 \in \mathbb{Z}$ and $F_1 \in \mathbb{Z}$ are the input pressure and input flowrate, and $P_2 \in \mathbb{Z}$ and $F_2 \in \mathbb{Z}$ are the output pressure and output flowrate, respectively. The propagation coefficient $\gamma \in \mathbb{C}$ and characteristic impedance $Z_c \in \mathbb{C}$ are the given in,

$$
\begin{cases}
\gamma = \sqrt{(R_0 + j\omega L_0)(G_0 + j\omega C_0)} \\
Z_c = \sqrt{(R_0 + j\omega L_0)/(G_0 + j\omega C_0)}
\end{cases}. \tag{3.3}
$$

The transmission line tube with distributed parameters can be equivalent to a π network in Figure 3.2(b) with lumped parameters of segment impedance $Z_g \in \mathbb{C}$ and segment admittance $Y_g \in \mathbb{C}$ in,

$$
\begin{cases}
Z_g = Z_c \sinh \gamma l \approx (R_0 + j\omega L_0)l \\
Y_g = \dfrac{\cosh \gamma l - 1}{Z_c \sinh \gamma l} \approx \dfrac{1}{2}(G_0 + j\omega C_0)l
\end{cases}. \tag{3.4}
$$

Hence, the entire network of airways can be represented as an electrical network made up of a layered bifurcating tree of impedance connected to the ground through an admittance at each bifurcating node, as illustrated in Figure 3.3(a). The air pressure and airflow rate are comparable to electrical potential and current, respectively, when the respiratory airways are analysed as an electrical network [11, 93, 96, 98-100]. The k-th layer's impedance and admittance can be presented in (3.5),

$$
\begin{cases}
Z_k = Z_g(k,\omega) \\
Y_k = Y_g(k,\omega) + 2Y_g(k+1,\omega)
\end{cases}, \quad k = 0, n. \tag{3.5}
$$

The network of airways is constructed with n nodes indexed with encircled numbers, b branches denoted with underlined numbers, the k-th layer as subscript, and a sinusoidal voltage source with amplitude P_s and angular frequency ω in series of a small impedance Z_{s0} applied at the input layer 0 to represent the fundamental component of the periodical patient breath, as presented in Figure 3.3(a).
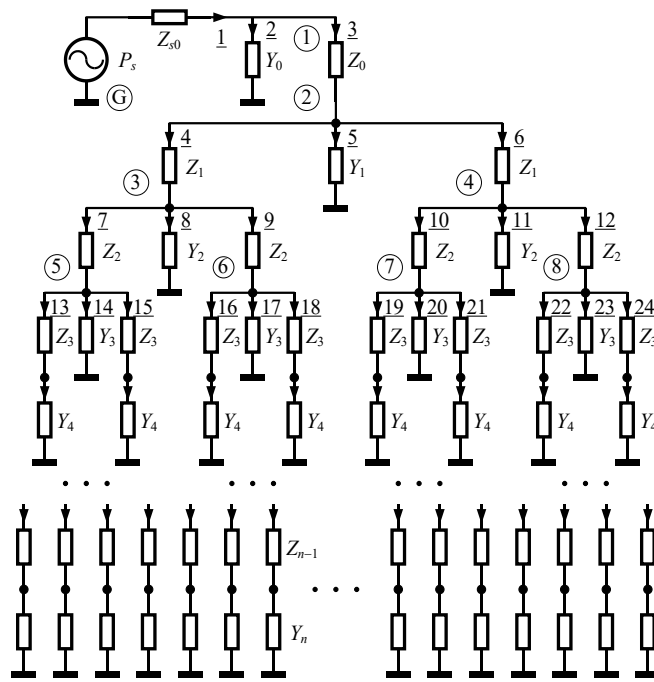
(a)
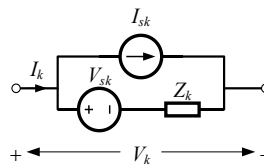
(b)

Figure 3.3 **Model of respiratory airways by equivalent circuit with lumped admittance parameters: (a) Node and branch indices and (b) standard branch.**

An incidence matrix **A** will be used to evaluate and simulate an acoustic network encompassing resistive and capacitive elements scattered over multiple interacting layers and acquiring a descriptor representation of the network, as demonstrated in Figure 3.2, Figure 3.3, and (3.1)–(3.5). Thus, the following annotations shown in (3.6) from the theory of network topology [94, 95] are given as,

$$
\begin{array}{c}
\mathbf{A} \in \mathbb{R}^{(n-1)\times b}, \mathbf{Y} \in \mathbb{C}^{b\times b}, \mathbf{Y_b} \in \mathbb{C}^{b\times 1}, \mathbf{V_s} \in \mathbb{Z}^{b\times 1} \\
\mathbf{V} \in \mathbb{Z}^{b\times 1}, \mathbf{V_n} \in \mathbb{Z}^{n\times 1}, \mathbf{I_s} \in \mathbb{Z}^{b\times 1}, \mathbf{I} \in \mathbb{Z}^{b\times 1}
\end{array},
\tag{3.6}
$$

where **A**, **Y**, **Y$_b$**, **V$_s$**, **V**, **V$_n$**, **I$_s$**, and **I**, are reduced incidence matrix, branch admittance matrix, branch admittance vector, branch voltage source vector, branch voltage vector, node voltage vector, branch current source vector, and node current vector, respectively. A typical branch in a linear network is shown in Figure 3.3 (b), and the node analysis is given in,

$$\begin{cases} \mathbf{A}^{\mathbf{T}} \cdot \mathbf{V_n} = \mathbf{V} \\ \mathbf{A} \cdot \mathbf{I} = \mathbf{0} \\ \mathbf{I} = \mathbf{Y} \cdot \mathbf{V} + \mathbf{I_s} - \mathbf{Y} \cdot \mathbf{V_s} \end{cases}, \qquad (3.7)$$

where Kirchhoff's voltage law and Kirchhoff's current law serve as the first and second requirements in (3.7), respectively, with the third requirement deriving from the standard branch law, and (3.8) can be obtained from the node analysis in (3.7).

$$\mathbf{A} \cdot \mathbf{Y} \cdot \mathbf{A}^{\mathbf{T}} \cdot \mathbf{V_n} = \mathbf{A} \cdot \mathbf{Y} \cdot \mathbf{V_s} - \mathbf{A} \cdot \mathbf{I_s}. \qquad (3.8)$$

The node voltage $\mathbf{V_n}$ is the remaining unknown variable from (3.8). Assuming node admittance $\mathbf{Y_n} \in \mathbb{C}^{(n-1)\times(n-1)}$ is a non-singular and symmetric square matrix, and $\mathbf{J_s} \in \mathbb{Z}^{(n-1)}$ is the node source-current vector as shown in (3.9), the node voltage $\mathbf{V_n}$ can be resolved in (3.10),

$$\begin{cases} \mathbf{Y_n} = \mathbf{A} \cdot \mathbf{Y} \cdot \mathbf{A}^{\mathbf{T}} \\ \mathbf{J_s} = \mathbf{A} \cdot \mathbf{Y} \cdot \mathbf{V_s} - \mathbf{A} \cdot \mathbf{I_s} \end{cases} \qquad (3.9)$$

$$\mathbf{V_n} = \mathbf{Y_n^{-1}} \cdot \mathbf{J_s}. \qquad (3.10)$$

From the graph in Figure 3.3(a), assuming $b = 3 \times 2^n$, and $\mathbf{I_s} = 0$ in (3.6)–(3.9), the reduced incidence matrix $\mathbf{A}$ and branch admittance matrix $\mathbf{Y}$ can be denoted as follows:

$$\begin{aligned} &\mathbf{A} = \left(\begin{array}{c|c} A_{11} & A_{12} \\ \hline A_{21} & A_{22} \end{array} \right), \ \mathbf{Y} = \mathrm{diag}(\mathbf{Y_b}), \ \mathbf{V_s} = \begin{bmatrix} P_s & \mathbf{0}^{1\times(b-1)} \end{bmatrix}^T \\ &A_{11} = \begin{bmatrix} 1 & -1 \end{bmatrix}, \ A_{12} = \begin{bmatrix} 1 & \mathbf{0}^{1\times(b-3)} \end{bmatrix}, \ A_{21} = \mathbf{0}^{(n-2)\times2}, \\ &A_{22} = \begin{bmatrix} a_{i,j} \end{bmatrix}\Big|_{\substack{i=2,\cdots,n \\ j=3,\cdots,b}} = \begin{cases} -1, & \text{if } j = 3(i-1)+k, k = 1, 2, 3 \\ 1, & \text{if } j = i + \mathrm{floor}(i/2) \\ 0, & \text{else} \end{cases}. \end{aligned} \qquad (3.11)$$

Table 3.1 shows the incident matrix $\mathbf{A}$, branch admittance vector $\mathbf{Y_b}$, and branch voltage source vector $\mathbf{V_s}$ of the first four network layers in Figure 3.3. The reduced incidence matrix

A is the resulting network matrix without the row of node G in Table 3.1. Given that the patient's breath pressure is sinusoidal, every joint pressure can be resolved by the network analysis method if the parameters Z_k and Y_k are known.

Incidence Matrix

A	1	2	3	4	5	6	7	8	9	10	11	12	13	14	15	16	17	18	19	20	21	22	23	24
(1)	1	-1	-1	0	0	0	0	0	0	0	0	0	0	0	0	0	0	0	0	0	0	0	0	0
(2)	0	0	1	-1	-1	-1	0	0	0	0	0	0	0	0	0	0	0	0	0	0	0	0	0	0
(3)	0	0	0	1	0	0	-1	-1	-1	0	0	0	0	0	0	0	0	0	0	0	0	0	0	0
(4)	0	0	0	0	0	1	0	0	0	-1	-1	-1	0	0	0	0	0	0	0	0	0	0	0	0
(5)	0	0	0	0	0	0	1	0	0	0	0	0	-1	-1	-1	0	0	0	0	0	0	0	0	0
(6)	0	0	0	0	0	0	0	0	1	0	0	0	0	0	0	-1	-1	-1	0	0	0	0	0	0
(7)	0	0	0	0	0	0	0	0	0	1	0	0	0	0	0	0	0	0	-1	-1	-1	0	0	0
(8)	0	0	0	0	0	0	0	0	0	0	0	1	0	0	0	0	0	0	0	0	0	-1	-1	-1
(G)	-1	1	0	0	1	0	0	1	0	0	1	0	0	1	0	0	1	0	0	1	0	0	1	0

Branch admittance vector

$\mathbf{Y_b}$	$1/Z_{z0}$	Y_0	$1/Z_0$	$1/Z_1$	Y_1	$1/Z_1$	$1/Z_2$	Y_2	$1/Z_2$	$1/Z_2$	Y_2	$1/Z_2$	$1/Z_3$	Y_3	$1/Z_3$	$1/Z_3$	Y_3	$1/Z_3$	$1/Z_3$	Y_3	$1/Z_3$	$1/Z_3$	Y_3	$1/Z_3$

Branch voltage source vector

$\mathbf{V_s}$	P_z	0	0	0	0	0	0	0	0	0	0	0	0	0	0	0	0	0	0	0	0	0	0	0

Table 3.1 **Incidence matrix, branch admittance vector, and branch voltage source vector.**

3.3.2 Parameter of Respiratory Airway Model

The airway wall was modelled using the complex Young's modulus and material density to replicate the acoustic structural interaction accurately [11, 13, 93, 101], where the material parameters of the respiratory system are given in Table 3.2. The airway segments' thickness, cartilage, and soft tissue fractions were determined by referring to the data reported in [13] and identifying the closest Horsfield order segment. Thus, the segment in the k-th layer has the material parameters in,

$$\begin{cases} Z_g(k,\omega) \approx (R_0(k) + j\omega L_0(k))l(k) = \dfrac{j\omega \rho_g l(k)}{A_s(k)(1 - F_v(k,\omega))} \\[2mm] Y_g(k,\omega) \approx \dfrac{1}{2}(G_0(k) + j\omega C_0(k))l(k) \\[2mm] \qquad = \dfrac{j\omega A_s(k)l(k)}{2\rho_g v_g^2}(1 + 0.402 F_t(k,\omega)) + \dfrac{l(k)}{2Z_w(k,\omega)} \end{cases} \tag{3.12}$$

where

$$\begin{cases} F_v(k,\omega) = \dfrac{2}{z_v}\dfrac{J_1(z_v)}{J_0(z_v)}, & z_v = \alpha(k)\sqrt{-j\omega\rho_g/\eta_g} \\[2mm] F_t(k,\omega) = \dfrac{2}{z_t}\dfrac{J_1(z_t)}{J_0(z_t)}, & z_t = \alpha(k)\sqrt{-j\omega C_g/K_g} \\[2mm] \dfrac{1}{Z_w(k,\omega)} = \dfrac{c(k)}{Z_c(k,\omega)} + \dfrac{(s(k))}{Z_s(k,\omega)} \end{cases}$$

and

$$\begin{cases} Z_i(k,\omega) = R_i(k) + j\omega L_i(k) + \dfrac{1}{j\omega G_i(k)} \\[3mm] R_i(k,\omega) = \dfrac{4h(k)E_i}{\pi d(k)^3 l(k)\omega} \\[3mm] L_i(k) = \dfrac{h(k)\rho_i}{\pi d(k)l(k)} \\[3mm] G_i(k) = \dfrac{\pi d(k)^3 l(k)}{4h(k)E_i} \end{cases} \qquad , \quad i = c \text{ or } s.$$

$A_s(k)$, $\alpha(k)$, ρ_g, η_g, C_g, and K_g are denoted as the cross-sectional area of an airway segment, internal airway radius, air density, viscosity, air specific heat, and thermal conductivity, respectively [12, 98, 102]. $F_v(k,\omega)$ and $F_t(k,\omega)$ account for the sound attenuation by air viscosity and sound attenuation by thermal dissipation, computed with series expansion with $J_0(z_v)$, $J_1(z_v)$ and $J_0(z_t)$, $J_1(z_t)$, being Bessel functions of 0-th and 1-st orders [102]. $Z_w(k,\omega)$ represents the wall impedance, which is computed from a series of resistance $R_i(k)$, inductance $L_i(k)$, and conductance $G_i(k)$, and Young's modulus E_i, where the subscript i is replaced by either c for the cartilage or by s for the soft tissue, respectively.

Variable	Units	Value
Air density	ρ_g (kg/m^3)	1.14
Airway wall viscosity	v_g (kg/(m·s))	1.82×10^{-5}
Air specific heat	C_g (cal/kg/K)	240
Air thermal conductivity	K_g (cal/m/s/K)	6.5×10^{-5}
Speed of sound in air	c_g (m/s)	343
Airway wall viscosity cartilage	V_c (Pa·s)	688
Lung density	ρ_c (kg/m^3)	1140
	ρ_s (kg/m^3)	1060
Airway wall modulus soft tissue	E_s (Pa)	5.81×10^4
Airway wall modulus cartilage	E_c (Pa)	3.92×10^5
Terminal tissue resistance	R_t (cmH$_2$O1^{-1}s)	0.5
Terminal tissue inertance	I_t (cmH$_2$O1^{-1}s^2)	0.005
Terminal tissue compliance	C_t (1cmH$_2$O^{-1})	0.1

Table 3.2   Material parameters of the airway geometry.

3.3.3 Acoustic Image Generation

Most of the previous works investigate the variable physical frequency characteristics [11, 93, 96, 98-100], and no spatial information is associated with the nodes. In this study, the spatial location (x, y) was integrated to each node to transform the airway network into a spatial network and generate the resulting acoustic image. The acoustic image can be initiated once the node voltage $\mathbf{V_n}$, which is analogous to the acoustic pressure $\mathbf{P_n}$ distribution within the airways [11, 93, 96, 98-100] is obtained. The sound pressure in dB within the airways is computed as,

$$\mathbf{P} = 20\log_{10}(\mathbf{P_n} / P_0)$$

(3.13)

where $P_0 = 20$ µPa is the reference sound pressure. The sound pressure generated from the lumped electrical network resulting from the transformation of the respiratory modelling, as presented in Figure 3.2 and Figure 3.3 can be captured with an array of acoustic sensors (see Figure 3.4), such as digital stethoscope or MEMS microphone [22, 30, 31]. An interpolation function can be utilised to compute the sound pressure between each sensor [31].

The airway pressure at each sensor location is computed by accumulating the captured signals over a given time interval t from t_1 to t_k and averaging the signals at all bifurcating airway nodes within the sensing area enclosed by the horizontal and vertical lines as the individual area boundary as shown in Figure 3.4,

$$\bar{P}\left(x,y,t_1,t_k\right) = \frac{1}{N_s}\sum_{i=1}^{N_s}\sum_{t=t_1}^{t_k} P_i(t)^2$$

(3.14)

where N_s is the total number of airway nodes within the sensing area. The network of the acoustic lung image $Q(x, y, t_1, t_k)$ is then,

$$Q\left(x,y,t_1,t_k\right) = \bar{P}\left(x,y,t_1,t_k\right)h\left(x,y\right).$$

(3.15)
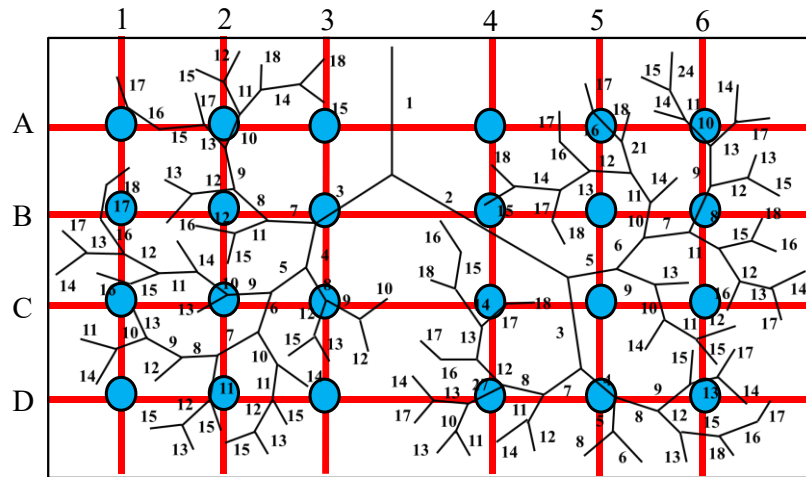
Figure 3.4 **The vertical and horizontal lines separate the airway geometry with the multiple sensing areas, and the known position of the simulated acoustic sensor array design is denoted with circles.**

The sound intensity outside of the sensor position in Figure 3.4 is estimated by interpolation. From the observation in (3.13)–(3.15), the acoustic lung image $Q(\bar{P}, h)$ is defined as the 2D acoustic image which comprise acoustic signal $\bar{P}(x, y, t_1, t_k)$ in (3.13) and (3.14) with interpolation polynomial $h(x, y)$. A high spatial resolution is required, hence, Hermite interpolation was applied to the acoustic signal $\bar{P}$ for projecting acoustic lung imaging [31]. From the study in [31], Hermite interpolation has been proven to be a better performance in presenting accurate lung sound intensity as compared to other established interpolation functions, such as linear, cube spline, Lagrange and nearest neighbour method. Refer to [31] for the Hermite interpolation function in-depth analysis, computation, and application on acoustic lung imaging.

Each acoustic image pixel is normalised, and the output obtained from the pressure sound signal is then presented as an acoustic image with the highest, lowest, and in-between values determined as maroon, white, and grey.

3.4 Model Verification by Pathology Examples

Model verification and the potential to assess the severity of airway obstruction through regional pathology with a predetermined sensor number and sensor sensing area are demonstrated in this section. Additionally, due to the vast range of lung sound frequencies documented in the literature, 400 Hz was chosen as the frequency to convey the results in this thesis for the relevancy to respiratory sounds, also demonstrated in Section 4.6.2 and

Figure 4.14, potential application in acoustic signal processing [93], and the frequency response trends in acoustic signal modelling at 400 Hz were similar to other comparable abnormal lung sound frequencies between 100–1000 Hz [93, 103].

A reference image was produced from a COPD patient's lung sound signal that was selected from a respiratory database [104]. A four-by-six array of sensors, as illustrated in Figure 3.4, where the sensors are considered to be equally dispersed within a 50 mm distance [22, 30, 31], and the acoustic response is the average intensity value within the sensing region. A 2D plane acoustic lung image can be produced with (3.13)–(3.15) and the known sensor and spatial position information (x- and y-axis) as shown in Figure 3.2 and Figure 3.4. The light-coloured (white) area is the colour for the minimal or no pressure data area, which represent the airway's high airflow resistance, whereas the dark-coloured (maroon) area is used to indicate high data locations where the airflow resistance in the airway is the least. Additionally, the in-between data area, where the airway has airflow resistance, is represented by light grey colours.

In the following, the assumption for the model simulation of pathology through AWT remodelling and the quantitative model performance are presented in Section 3.4.1 and Section 3.4.2, respectively. The results and discussion are described in Section 3.4.3.

3.4.1 Pathology Simulation

Airway remodelling was performed by altering the AWT to simulate airway obstruction [105-110]. As shown in Figure 3.2, the total wall thickness of each airway segment $H_w = D_o - D_i$, where D_i and D_o are the inner and outer diameters, respectively.

The inner airway diameter D_i and total wall thickness H_w were measured and compared from patients with illnesses, such as asthma and COPD, using computed tomography in relation to the severity (mild, moderate, severe) of the illness [105-107, 109, 111]. The studies in [105-107, 109, 111] have revealed a range for the mean airway wall area percentage (WA%) increment of 3%–40%, with 0%–3% for controls, 4%–10% for mild conditions, 11%–30% for moderate conditions and more than 30% for severe conditions. The airway wall area (WA) and WA% can be calculated as [106],

$$\begin{cases} \text{WA} = A_o - A_l \\ \text{WA\%} = \text{WA}/A_o \times 100 \end{cases}, \qquad (3.16)$$

where $A_0 = \pi(D_o/2)^2$ and $A_l = \pi(D_i/2)^2$ can be computed as the airway area and the luminal area, respectively.

3.4.2 Performance Assessment

The mean acoustic image intensity (dB) in (3.13)–(3.15) can be utilised as an indicator for the assessment outcome on the severity of airway obstructions [21-23]. The increment (factor) of AWT was implemented to standardise the findings in this study, as mixed airway obstruction results can be identified from the literature, such as the increment of WA% or values of AWT [105-107, 109, 111].

For instance, the AWT must increase by a mean factor of 2.34, as shown in (3.16), for the mean WA% to increase by approximately 11%, from 67% healthy lung to 78% respiratory illness lung [105-107, 109, 111]. Finally, in terms of the severity of respiratory diseases, the internal airway area between asthma and COPD was essentially the same [105]. Therefore, no differentiation between COPD and asthma is made in this modelling study.

The pixels in natural image signals are heavily dependent on one another, especially when the pixels are close together. These dependencies include important details about how the elements in the visual scene are arranged. The SSIM index [34] is a straightforward approach for comparing the reference and distorted signal structures. Additionally, SSIM indexing provides quality assessment from the perspective of image generation, particularly for components of medical images in pixel intensities [32]. The SSIM quality assessment index is based on the computation of three terms, namely the brightness term, the contrast term, and the structure term, as illustrated in,

$$\text{SSIM}(Q_r, Q) = \frac{\left(2\mu_{Q_r}\mu_Q + C_1\right)\left(2\sigma_{Q_r Q} + C_2\right)}{\left(\mu_{Q_r}^2 + \mu_Q^2 + C_1\right)\left(\sigma_{Q_r}^2 + \sigma_Q^2 + C_2\right)}, \tag{3.17}$$

where μ_{Qr} and μ_Q are the local means, σ_{Qr} and σ_Q, are the standard deviations, σ_{QrQ} cross-covariance, and C_1 and C_2 are the constants for reference image Q_r and captured image Q. For detailed derivation and computation, see [34].

3.4.3 Model Validation

The acoustic lung imaging Q projected from lung signals is computed from the lung signal intensity $\bar{P}$ at each sensor location in a coordinate plane over a known time t interval as shown in (3.14) and (3.15). The lung signal intensity is determined as highest (maroon), lowest (white) or in between values (grey). The acoustic signal is normalised, and the output obtained from the intensity of the sound signal is then displayed as an acoustic image.

The spatial resolution of the lung geometry in this model validation is 44 pixels for every 10 millimetres. Figure 3.5 displays acoustic images of a healthy lung (control) and varying respiratory illness severity obtained by adjusting the AWT in Section 3.3 and (3.13)–(3.15). An outline is used in Figure 3.5 to better identify the effect of AWT on the overall (global) lung image intensity. Additionally, Figure 3.6 displays the relationship between the average image intensity and the global AWT increment.
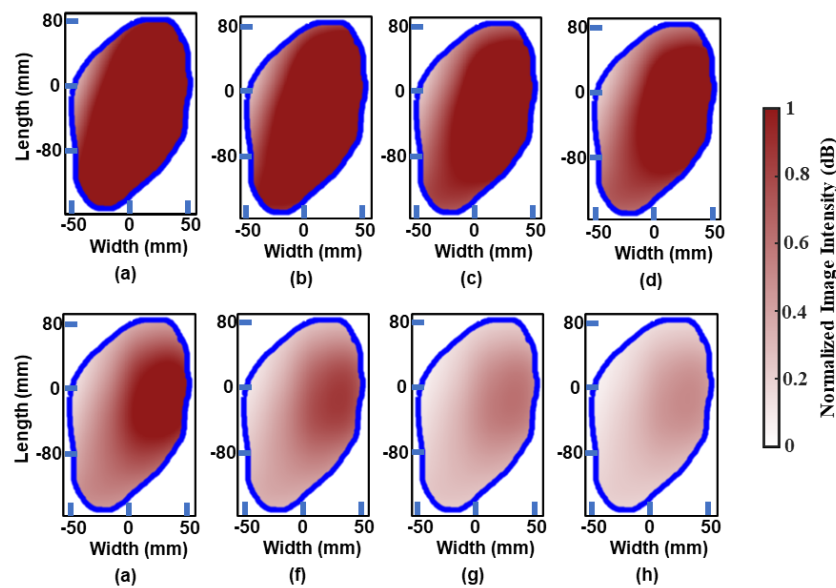
Figure 3.5   **Right lung acoustic images generated from (3.2)–(3.15) acoustic signals and an Hermite interpolation function with various factor increments in AWT. (a) Healthy lung; AWT increasing by a factor of about 1.2, 1.5, 1.7, 2.48, 3.5, 4.97, and 6 in (b), (c), (d), (e), (f), (g), and (h) respectively.**
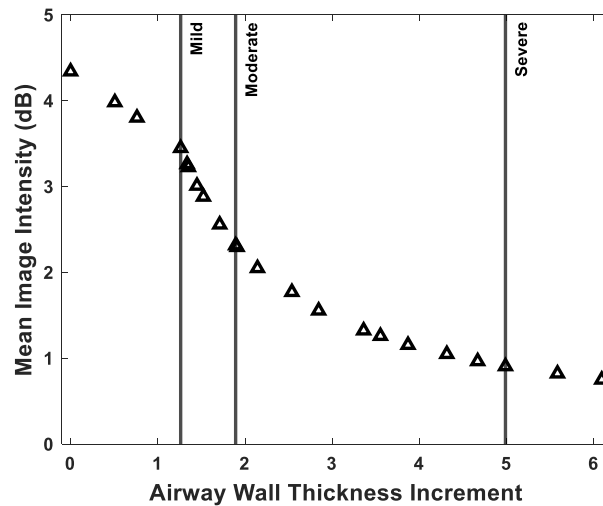
Figure 3.6   Quantitative lung function assessment through the mean image intensity and the thickening factor of AWT.

Figure 3.5 and Figure 3.6 demonstrated the relationship between acoustic lung images of healthy and ill conditions. In contrast to ill conditions, such as mild, moderate, and severe conditions, a healthy lung presents the darkest lung image (high acoustic intensity value) due to the lowest impedance – smallest resistance in the airway, from Figure 3.5 and Figure 3.6 and as observed from (3.2)–(3.13). Moreover, the airflow and the mean image intensity both reduced with the thickening of AWT can be observed in Figure 3.5 and Figure 3.6. Although observable qualitative changes can be seen with the AWT increasing by a factor of more than about 2.48 in Figure 3.5, the mean image intensity in Figure 3.6 can reveal the state of the lungs' condition. Furthermore, the positive correlation between the lung impedance from (3.2)–(3.13) and the results in Figure 3.5 and Figure 3.6 presented a certain level of similarity compared to the literature [21-23, 90, 105, 106, 111], e.g., the global intensity distribution impacting the lung and the airway closer to the trachea (Figure 3.2) is often larger and tends to be the last impacted region by the thickening in AWT.

After the global thickening in AWT and the consequences (severity) on lung function have been demonstrated earlier, the next validation task is the regional increase in AWT. Figure 3.7 contrasts the developed model acoustic image with the obstructed reference lung image, which was created using the lung sound signals extracted from a respiratory database [104], and converted into an acoustic image. The obstructed airway is situated along the posterior right middle scapular line (area B2), and the posterior right lower scapular line (area C3), as shown in Figure 3.4. The region of the obstructed airway can be located in the developed model's acoustic image presented in Figure 3.7. The similarity between the acoustic

reference image and the model acoustic image is highly related given that a mean SSIM index of 0.8987 was obtained, with 1 being the same as the reference [34].
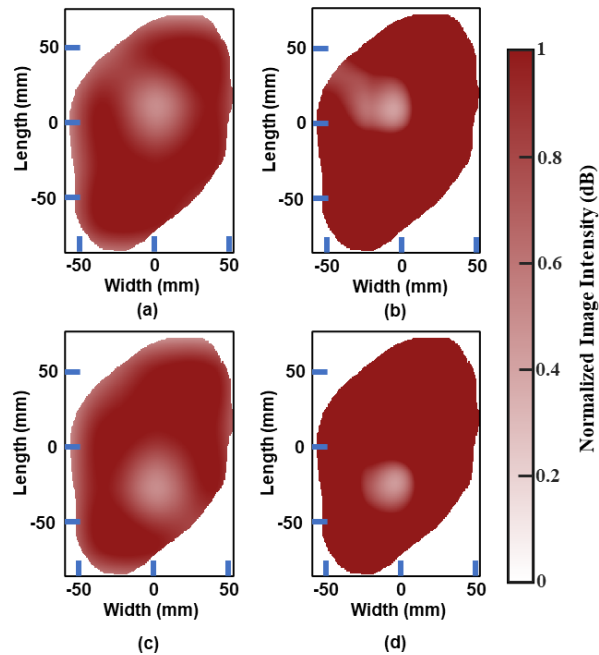
Figure 3.7 **Acoustic imaging of obstructed airway with AWT increased by about a factor of 1.7. (a), (c) Acoustic image produced from lung sound signal and Hermite interpolation function. (b), (d) Model acoustic image produced from airway pressure signal and Hermite interpolation function.**

3.5 Optimal Acoustic Sensor Array Design for Airway Obstruction Detection

Global and regional pathology with prearranged number of sensors, e.g., an array of 4-by-6 with 50 mm uniform spacing acoustic sensors, has been validated in Section 3.4. The remaining task in this study is how the design of the acoustic sensor array affects the minimal detectable nidus length. E.g., the minimal detectable nidus expected if the acoustic sensor array is known or the design of the acoustic sensor array for an envisioned minimal detectable nidus length. To the best of the authors' knowledge, no discussion was attempted relating to the distribution array of acoustic sensors for image assessment and the acoustic imaging resolution, as the array sensor design was typically empirical in the literature [22, 30, 31]. In line with the uniform distribution design of HFCWO electromagnetic/pneumatic actuators [46, 47], and the traditional acoustic imaging system in the literature [22, 30, 31], a uniform multimicrophone distribution, vertically and horizontally, is employed in this thesis. In addition, the overlapping and nonoverlapping sensor sensing sensitivity can be computed due to the influence of the sensor uniformly distributed. Hence, the effect of sensor

sensing sensitivity area and sensor number on the detection of airway obstruction is presented in Section 3.5.1, followed by analysis and discussion in Section 3.5.2.

By employing local first-order image statistics [112] around each pixel, the resulting obstructed airway acoustic image τ are converted into a binary image, as shown in Figure 3.8. As shown in Figure 3.8(c), areas with high-intensity data (healthy) are denoted by 1s, and areas with low-intensity data (obstruction) by 0s. Thus, by comparing the acoustic image pixel area ζ in Figure 3.8(a) and the pixel area τ in Figure 3.8(c), the obstruction in the airway acoustic images can be located, and the area of the missing pixel $(\zeta - \tau)$ can then be used to calculate the obstructed area (nidus) length,

$$Ln = 2\sqrt{\frac{(\xi - \tau)}{\pi}}. \tag{3.18}$$
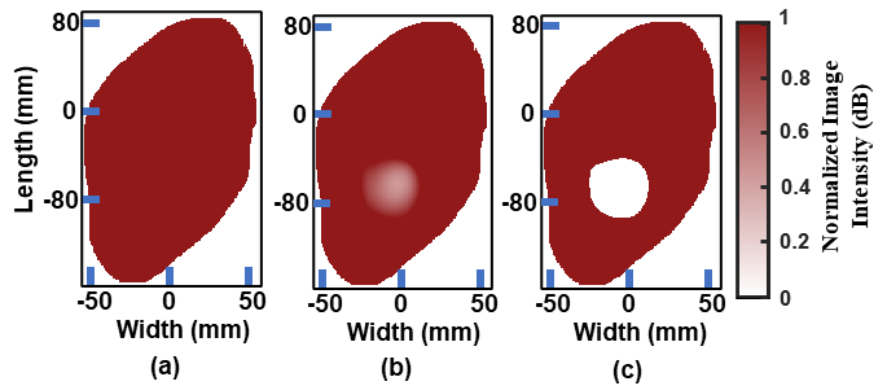
Figure 3.8 **Acoustic image and nidus generation, together with Hermite interpolation function. (a) Healthy acoustic image, (b) Obstructed acoustic image, and (c) Binarised obstructed acoustic image.**

3.5.1 Sensor Sensing Sensitivity and Sensor Number

To study the effect of sensor sensitivity on the smallest observable nidus length L_n, the number of sensors is initially fixed at 12, 16, 20, 25, 32, 40, 45, and 50 per lung side, comparable to the empirical acoustic image system [22, 30, 31]. The selection of the sensor sensing diameters, which ranged from 10 mm to 50 mm in 10 mm increments, was made in accordance with commercially available products and published research [22, 31]. Figure 3.9 shows the relationship between sensor sensitivity with a predetermined number of sensors and the measured minimum nidus length. After the effect of the different sensor

detecting area on the minimum detectable nidus length when used with a predetermined number of sensors, the next step is to evaluate how the number of sensors affects the minimal detectable nidus. Figure 3.10 illustrates how the number of sensors affects the minimum observable nidus length for different sensor sensing sensitivities.
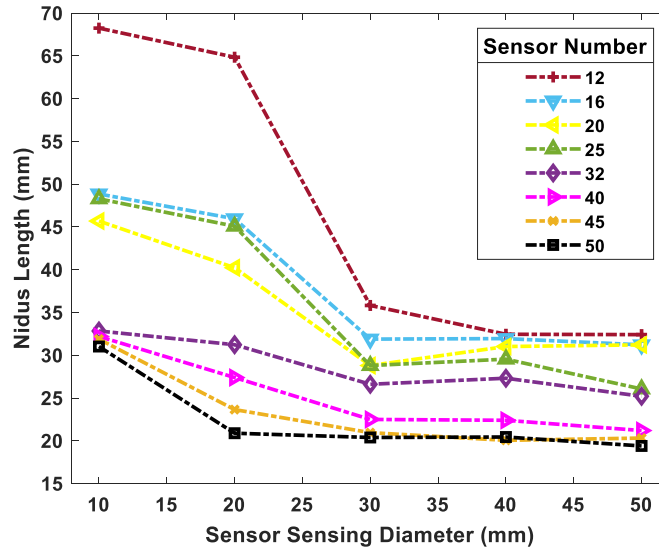
Figure 3.9 **The relation between sensing sensitivity and the minimal nidus length that can be observed with a predetermined sensor number.**

3.5.2 Analysis of the Sensor Array Design

A minimal detectable nidus length of about 68 mm is expected when using 12 sensors with a 10 mm sensor sensing diameter, as illustrated in Figure 3.9. In contrast, a minimal detectable nidus length of about 20 mm is expected with 50 sensors, with sensor sensing diameter between 20 mm and 50 mm. Figure 3.10 demonstrates the number of sensors and the sensor sensing diameter required in the acoustic sensor array for envisioned minimal detectable nidus length.

According to Figure 3.9, a better resolution of the detectable minimal nidus length was obtained with the increase in sensor number, and the sensor sensitivity area overlaps more when compared to fewer sensor numbers and lesser overlapping of sensor sensitivity area. When compared across all sensor sensing diameters, the predefined sensor number showed various observed nidus lengths, as shown in Figure 3.9. The results are in line with the number of sensors and the position, where higher image resolution can be identified with sensor sensing diameter (30 mm–50 mm) overlapping, reducing the over-reliant on

interpolation function, as compared to sensor sensing area that has lesser nonoverlapping sensor sensing diameter (10 mm–20 mm) [31].

(a)

(b)
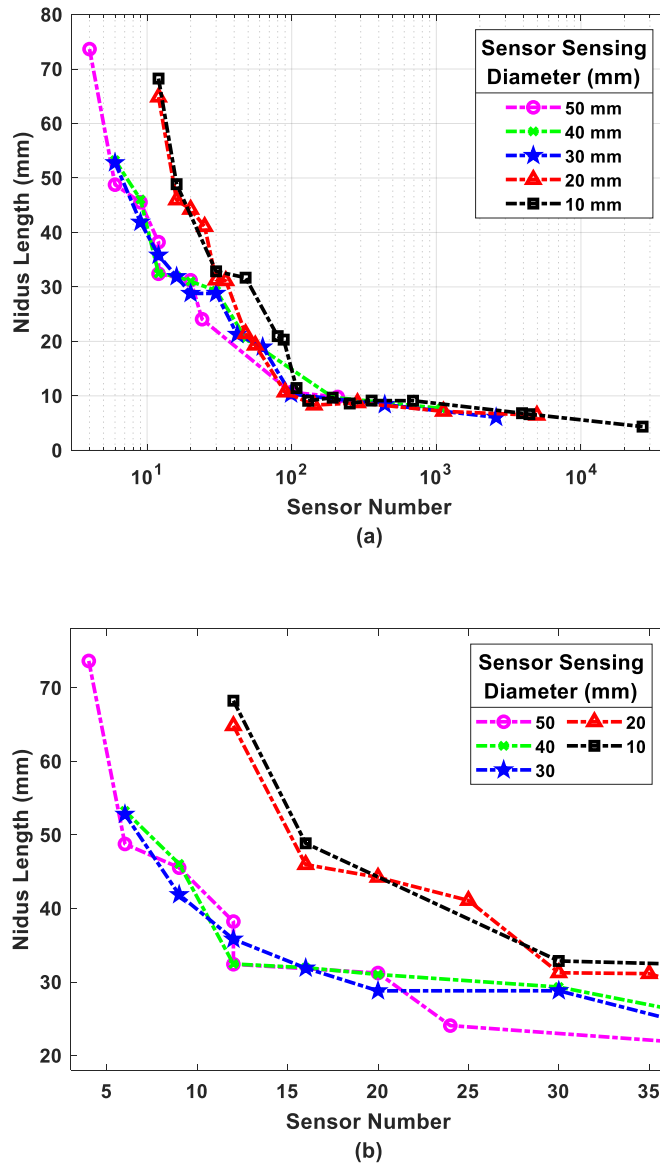
Figure 3.10   The relationship between sensor number and minimal nidus that can be observed on the right posterior of the chest wall. (a) The theoretical impact of sensor number required to identify the nidus length, and (b) The typical sensor numbers in a practical acoustic imaging system.

From Figure 3.10(a), a low resolution observed in the detected nidus length is about 73 mm, requiring about 4 sensors, with a 50 mm sensor sensing diameter and a 0% sensor sensing overlapping area. In comparison, a high resolution identified in nidus length is about 4.35 mm, requiring about 26,000 sensors, with a 10 mm sensor sensing diameter and a 95% sensor sensing overlapping area. The observations in Figure 3.9 and Figure 3.10, where the resolution of nidus length detected increases with the increase in sensor numbers and

corresponded with the understanding that image resolution increases with the number of sensors. The practicality in the designing of an acoustic imaging system for the location of nidus length, in terms of the number of sensors required, is demonstrated in Figure 3.10(b).

3.6 General Discussion

The severity of respiratory diseases has been demonstrated with the mean image intensity and the thickening of AWT. The assessment of lung function through acoustic imaging, such as presenting global and regional obstructed airways, was demonstrated in Figure 3.5–Figure 3.7. All 35-airway segment layers, starting with the trachea at $k = 1$ and terminating at the terminal bronchiole with $k = 35$, were included in the calculation of the acoustical impedance. A similarity rating of about 89% was achieved between the developed model image and a reference image converted from lung sound signals. Minimal differences in Figure 3.7 and the SSIM rating are expected as the acoustic images in Figure 3.7 were generated from two different sources: the developed model computed acoustic impedance and the actual acoustic signal from a respiratory database [104]. Only large airways, e.g., airway segment length > 2 mm, were utilised in the acoustic imaging, as small airways length ≤ 2 mm flow is laminar and silent, hence, do not produce an acoustic signal [103]. Bifurcate node angles of the airway system were assumed to be between 45 and 60 degrees and was drawn ideally in Figure 3.2(a) so that the airway system does not overlap [93]. The sound pressure computation is based on the mean sound pressure within the sensing region, as shown in Figure 3.4 and (3.14). Hence, the SSIM rating can be improved with the additional weighted ratio between pressure in the individual airway segment and sensor sensing radius to (3.13)–(3.15), and an increase in the total number of airway segments in the model.

In addition, this study's objective demonstrated the respiratory model systems' capability to pinpoint the source of airway obstruction through acoustic signals, in terms of the minimal nidus length identified through the location of obstructed airways to both the acoustic sensor sensitives and the number of acoustic sensors to improve HFCWO therapy in Figure 3.5–Figure 3.10. Although the findings in Figure 3.5–Figure 3.10 are based on a uniform distribution of sensor location, this thesis can be used as a starting point to study nonuniform sensor distribution, which may potentially result in a reduction in the number of sensors needed to achieve the same performance. Additionally, this work uses respiratory remodelling and sensor array simulation to evaluate the sensor's placement, sensitivity ranges, and the numbers for minimal nidus length detection. This thesis can also be used to assess an existing acoustic array system and provide direction for the development of

acoustic imaging systems, particularly in imaging systems that employ a multi-acoustic sensor array. Therefore, by comprehending how sensor array and sensing sensitivity affect lung health assessment with the resolution of detected nidus and optimising the sensor array by determining the number of sensors required, a guideline for designing HFCWO devices and assessing the HFCWO therapy efficacy on the patient for a smarter process through therapy feedback from identified nidus length may be provided.

3.6.1 Design Consideration of Imaging Hardware System

Two of the many deciding considerations in creating the acoustic imaging systems in this study can be sensor type and sensor costs. Different transduction techniques, such as condenser (MEMS microphones) and piezoelectric (digital stethoscope) transduction, can be used to record the acoustic images derived from acoustic lung signals. Piezoelectric sensors were often not mechanically durable and required hard, specialised contacts with the patient's skin, such as gels and vacuum seals [22, 29]. Due to their repeatable frequency response and high SNR, MEMS microphones are frequently employed to acquire lung sound signals and indirectly provide excellent acoustic imaging [113-116]. Additionally, flexible multi-sensor arrays, such as MEMS microphone arrays, are perfect for delivering a 2D visualisation assessment of the lungs in contrast to a single sensor, such as a digital stethoscope, which can only provide one region of data at a time [113-116].

MEMS microphones are also small, light, and inexpensive, costing only a few dollars, around USD 4, as opposed to a digital stethoscope, which may run between USD 300 and USD 500 [113-115]. In addition, MEMS microphones can be redesigned to accommodate various sensor sensings diameter requirements, such as 10 mm, 20 mm, or 50 mm, while the sensor sensing diameter is designed to partially integrate over the fixed surface area (50 mm) of the stethoscope head [116].

For the same detected minimal nidus length, several sensor number and sensitivity combinations can be perceived in Figure 3.10(a). A minimal nidus length of around 50 mm that can be detected, for instance, can be achieved using 6 pieces of 50 mm sensor sensing diameter or 16 pieces of 10 mm sensor sensing diameter. The detected nidus length assumes that the position of the sensor is spaced uniformly and covers the chest posterior area similar to how clinicians and doctors perform auscultation on the patient. Given that one MEMS microphone can cover a 10 mm sensing diameter and five MEMS microphones can cover a 50 mm sensing diameter [116], using a 10 mm sensor sensing diameter may cost the

customer roughly USD 64 as opposed to USD 120 with a 50 mm sensor sensing diameter. Similarly, a minimal nidus length of around 30 mm that can be detected, for instance, can be achieved using 20 pieces of 50 mm sensor sensing diameter or 48 pieces of 10 mm sensor sensing diameter. Using a 10 mm sensor sensing diameter may cost the customer roughly USD 192 as opposed to USD 400 with a 50 mm sensor sensing diameter [116]. In terms of the standard MEMS microphone physical size and the adult chest area, a maximum of roughly 1000 pieces of MEMS microphone with a 10 mm sensor sensing diameter can be fitted without physical devices overlapping onto the chest region [113-117]. The author anticipate that as sensor technology advances in terms of the physical size, allowing the number of sensors to multiply, the resolution of the detectable nidus length can also be enhanced, as depicted in Figure 3.10(a). Since the lung assessment imaging gold standard, such as chest X-ray, has a high operational cost (> USD 5000) and radiation exposure (health hazard), which indirectly leads to the unsuitability in frequent assessment, the detection of obstructed airways by acoustic imaging represents a crucial clinical need [29]. In the literature [22, 29, 30], an array of microphones was employed to produce an acoustic image that was comparable to a chest X-ray in terms of sensitivity, specificity, and intra- and inter-rater agreement. Besides, the resolution of the acoustic lung image in this research was primarily designed to enable frequent nidus detection by simple 2D image viewing and frequent evaluation of the efficacy of HFCWO therapy.

3.6.2 Limitation

With the current study, four critical points should be considered. First, this study focused on lung signals generated, while the separation of heart sound signals and lung sound signals was not considered. Hence, the signals obtained were assumed to be at the patients' posterior, similar to how a doctor and clinicians perform auscultation, significantly minimizing the interference from heart signals. Second, there will be variations in respiratory system model performance due to a range of factors such as the system network architecture: node position in the x- and y-axis location, and the physical airway model, e.g., Horsfield or Weibel airway model. The results presented in this research are based on the respiratory model's independent abilities to optimise both the number and position of acoustic sensors for obtaining useful acoustic information, and other unsupportable combinations of acoustic sensor's position is not taken into account, such as imbalanced position, e.g., an offset position from adjacent sensors. Third, the diameter of the obstructed lung region estimated from a circle's surface area is used to establish the length of the obstructed airway reported in Figure 3.9 and Figure 3.10. The airway geometry was assumed to be translated from a 3D

space to a 2D plane without any intersections. To prevent outliners from determining the nidus length, a carefully selected simulated obstructed area was used. The lung size [117] of the respiratory system model shown in Figure 3.2 is maintained at roughly 240 mm (height) by 100 mm (width), which is within 90% of the actual lung size. Finally, it is possible to locate the obstructed area in the simulated lung model precisely due to 1) only sensor distribution and sensor sensitivity area were considered in the simulated acoustic imaging sensor array design, and the actual sensor characteristics were excluded; 2) The model is believed to be interference-free from body movement, body temperature, ambient, and the ideal sound pressure can be captured directly through typical acoustic sensors utilised for capturing lung sound signals [113-116].

3.7 Summary

A spatial network of the respiratory system modelling is developed in this chapter, and sensor array design studies through acoustic lung imaging based on the model are conducted. The study results in a framework for the optimization of the HFCWO therapeutic technique that has shown: 1) The acoustic relationships and imaging characteristics between the sensing system and the location of nidus; and 2) How the sensor numbers and sensor sensing sensitivity affect the image dynamics at various locations within the chest area. The potential of assessing lung function with acoustic imaging has been validated through respiratory remodelling and obtained a similarity of 89% as compared to the acoustic image initiated from actual lung sound signals. Additionally, this study offered design guidelines for acoustic imaging systems or served as a performance assessment of already-in-use multimicrophone array-based acoustic imaging systems.

The research demonstrated using acoustic imaging to assess lung function and identify airway obstructions. The research focused on lung sounds, without consideration of separating heart sounds. Reference signals were assumed to be from the posterior to minimise heart sound interference, similar to doctors or clinicians performing actual auscultation. Variations in model performance are expected based on factors like node positioning and airway model architecture. Heart sound separation merits further study to strengthen model accuracy. The assumption on the projection of 3D to 2D imaging of obstructed regions needs further study to assess underestimation or overestimation.

Chapter 4   Enhancement of Acquired Lung Sound Signals Using a Hybrid Wavelet-based Approach

Modelling of noise-free lung airways as a spatial network and the effects of obstructed airways on acoustic imaging were demonstrated in Chapter 3. However, noises from ambient and recording electronics are present in actual lung sound recordings. Thus, a denoising algorithm is proposed to enhance the recorded lung sounds to improve the acoustic imaging for lung function assessment and to identify accurately the location of the pathology produced by the airways for smart therapy.

Chapter 4 is reproduced§ from [2, 6, 7], where the thesis author is the main author of the paper. Chapter 4 is organised as follows. The overview and state-of-the-art filters are presented in Section 4.1 and Section 4.2, respectively. This is followed by data model and the assumption, and the problem formulation in Section 4.3. Next, the proposed denoising technique is presented in Section 4.4. Section 4.5 presented the simulation results and discussions of WATV-Wiener filter parameters tuning, and denoising synthesised lung sound signals. Simulation results were compared and discussed with experimental results in Section 4.6, and the conclusion is presented in Section 4.7.

4.1 Overview

Respiratory sounds carry the signature of the health status of the lungs and can be used for diagnosing respiratory diseases. For example, auscultation serves as a reference point and is frequently used by doctors and clinicians to "listen" to weird lung sounds and patterns. While auscultation is widely adopted, it is not easy to use as issues such as variability and dependent on inter-listeners medical and diagnostic skills. In this regard, computer-based lung sound techniques are attractive as they eliminate the subjective nature and provide a more reliable approach to assessing lung function [118-120]. However, in lung sound recording, noise source such as ambient noise is an inevitable interference that can obscure the existence of

---

interesting sound trends. Interference obstructs the computer-based lung sound algorithm's applicability or results in undesirable false positives; thus, noise reduction or denoising is crucial in lung sound signal processing.

To address these issues, an indirect and optimal integration of WATV filter and wavelet-based empirical Wiener (WATV-Wiener) filter to smoothen the denoised signal (see Figure 4.1) and significantly improve the SNR and RMSE of the denoised signal, which are crucial for an accurate assessment was proposed in this research. SNR, in this case, reflects the denoised signal strength in relation to noise without compromising the frequency components of interest contained in the lung sound signal. Literature has confirmed that clinicians were able to distinctly identify airway diseases such as asthma, COPD, and fluid around the lungs (pneumonia) from captured interesting signal waveform characteristics such as wheeze and crackle [120-122] compared to pre-denoised data, typically on conditions that the SNR is enhanced in the order of 4–20 dB [119, 123-125]. RMSE results reflect the filter capability in denoising and retaining significant characteristics of lung sound. Inefficient parameter selection resulting in overly suppressed denoised signal may result in high SNR, despite the filter introducing obvious distortions resulting in undesirable RMSE results. As a result, RMSE is also a crucial criterion for determining if the denoising filter keeps the desired waveform characteristics of interest.

In addition, a comprehensive investigation was conducted on ideal parameters selection to facilitate the optimisation of the proposed WATV-Wiener technique, particularly in the lung sound signal domain, as only parameters estimates were available in the literature [126, 127], and no case studies on how the parameters adjustment affected the filter performance were performed or discussed.

To thoroughly evaluate the WATV-Wiener filter, the proposed filter was compared with a range of state-of-the-art lung sound signal denoising techniques, which had achieved either optimal SNR or RMSE performance, or achieved good results in both SNR and RMSE in [123, 126, 128-131], and [127]. The bandpass (BP) filter [128], Hard- and Soft- thresholding filter [130], Serial filter [123], and Savitzky-Golay (SG) filter [129] have shown good SNR performance, while the total variation (TV) filter [131] and WATV filter [127] have shown good RMSE results in the literature. In simulation and experimental studies, WATV-Wiener and the seven filters mentioned above are applied to both healthy lung sound signals and lung sound signals containing crackle and wheeze, and the performance is evaluated in terms of RMSE and SNR improvement. In comparison with the BP filter, Hard and Soft

thresholding filter, Serial filter, SG filter, and TV filter in denoising noisy lung sound signals, the optimised WATV-Wiener technique achieved better RMSE results by 0.2–0.7 V in both simulation and experiment studies. In addition, compared with the seven filters as mentioned earlier, the WATV-Wiener achieved better SNR performance by 12.69 ± 5.05 dB and 16.92 ± 8.51 dB in simulation- and experimental-studies, respectively. Through the efficient parameters identified in the parameter tuning evaluation, the WATV-Wiener filter achieved optimal RMSE results regardless of the low or high noise variance in the lung sound signals — showing the capability in preserving signal characteristics from noise and further improving SNR.
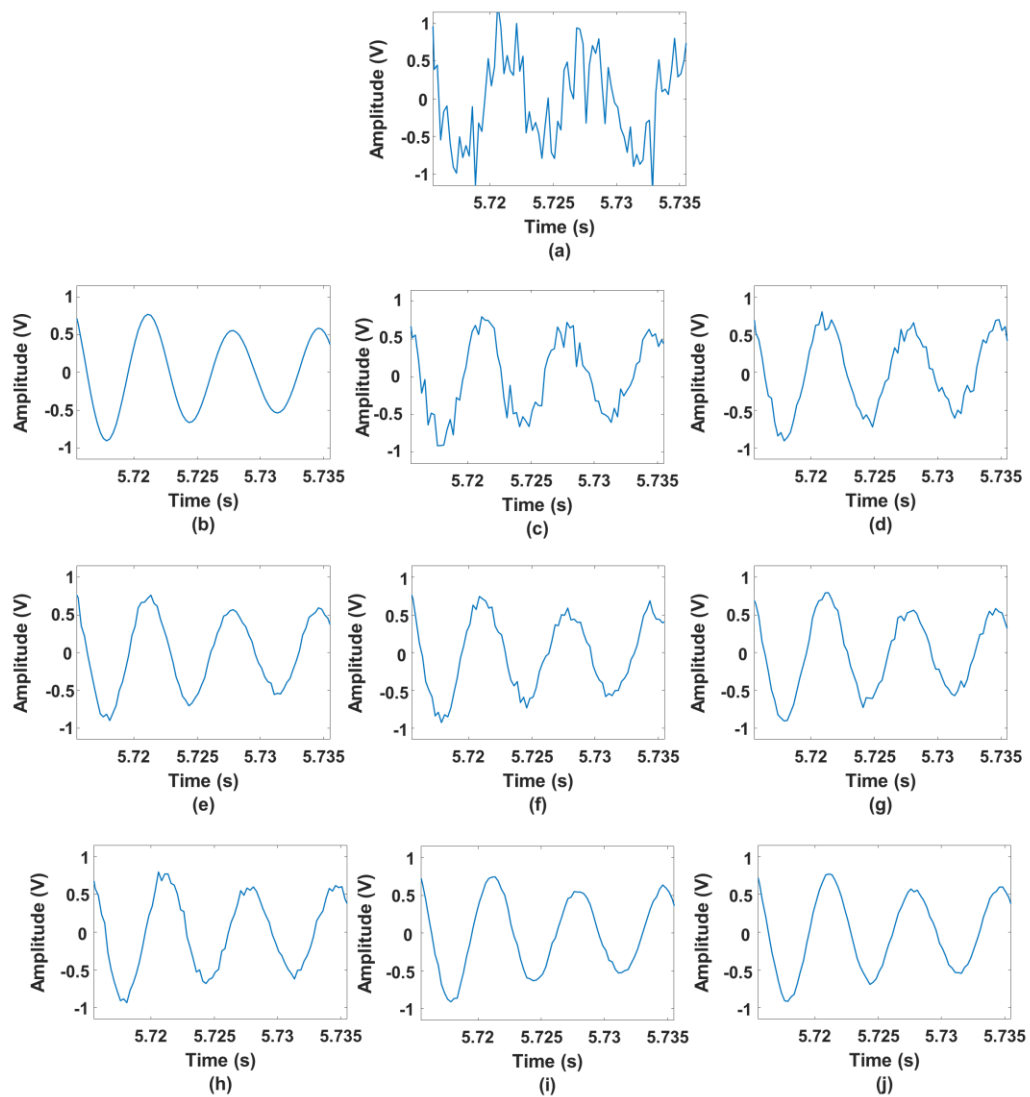
Figure 4.1 **Comparing (a) noisy signal, (b) noise-free signal, and the output of normalised denoised lung sound signal typically for lung health assessment and diagnostic through (c) Bandpass filter; (d) Hard thresholding filter; (e) Serial filter; (f) Soft thresholding filter; (g) Savitzky-Golay filter; (h) Total variation filter; (i) WATV filter; and (j) Proposed filter – WATV-Wiener filter.**

4.2 State-of-the-Art Lung Sound Denoising Techniques

In the literature [121, 132], including Chapter 2, and Chapter 3, adventitious lung sounds are indicators of lung dysfunctions, and they can be related to airway obstruction and various pulmonary diseases such as asthma, COPD, pneumonia, and sputum production. The adventitious lung sounds can be grouped as crackles and wheezes [121, 133]. Coarse crackles are non-continuous, non-musical, explosive, and have a typical frequency of 350–950 Hz and a duration of 10–15 ms. Contrarily, wheezes are continuous, musical, oscillatory, have a typical frequency range between 100 and 1000 Hz, and a duration of 100 ms. Hence, differentiating the adventitious lung sound signals from noise, as shown in Figure 4.2, is critical for improving the lung function assessment.
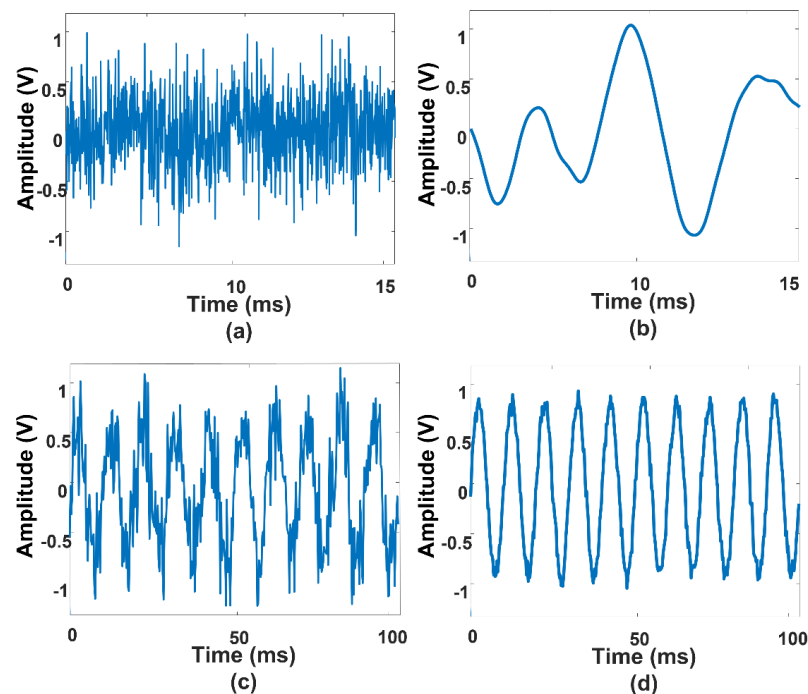
Figure 4.2   Typical recorded lung sounds and the interesting waveform trend and characteristics for lung health assessment. (a) Noisy lung sounds recording with crackle; (b) Crackle waveform; (c) Noisy lung sound recording with wheeze, and (d) Wheeze waveform.

The straightforward approach to mitigating external interference is linear high-pass or BP filtering with a specific cut-off frequency [128]. SG filter, a finite impulse response (FIR) filter, was proposed to denoise and smoothen the lung sound signal from noise [129]. An FIR-based filter, particularly the BP filter, can reduce unwanted noise in the low and high frequency ranges from the observed signal; however, the lung sound and noise interference

may have spectral overlap in the low or the passband frequency range [120, 123, 134]. A combination of a chain of filters: FIR-based BP filter, a wavelet-based filter, and a least mean square adaptive filter was proposed (Serial) in [123] to overcome the problem in FIR-based filter in reducing unwanted noise from lung sound signals.

Classical wavelet-based universal soft thresholding (Soft), universal hard thresholding (Hard), or wavelet transform methods are a practical signal denoising approach when the actual noise-free signal is practically unknown [123, 130, 135-138]. Wavelet transform assumes the "nonstationary" region, typically lung signal, produces significant wavelet transform coefficients (amplitude) over many wavelet scales. The "stationary" region, typically noise, decays quickly with increasing scale without affecting the signal quality. The limitation of the classical wavelet transform is introducing artefacts such as spurious Gibbs oscillations and noise spikes around discontinuities [126]. Generally, when the noisy wavelet coefficients exceed the threshold, noise spikes occur in the denoised signal [126]. When the noisy wavelet coefficients are less than the threshold and inaccurately set to zero, spurious--Gibbs artefacts appear in the denoised signal [126]. TV denoising is introduced to improve the denoised signal by reducing the artefacts produced by wavelet transform [131]. However, TV denoising often produces undesirable staircase artefacts.

An alternative approach is to perform empirical Wiener filtering in the wavelet transform domain [139]. Since the actual signal is practically unknown as different individuals exhibit different adventitious lung sound characteristics, Wiener filtering becomes empirical [140]. Wavelet-based empirical Wiener filter considers both significant (signal) and insignificant (noise) wavelet coefficients for scaling/denoising. An acceptable signal estimate for Wiener filter construction is critical in the wavelet-domain Wiener filtering [139-142]. The wavelet-domain empirical Wiener filtering uses two different wavelet transform bases (two/dual-stage transform): 1) Wavelet transform discards small coefficients (noise) and retains significant coefficients (signal) for denoising noisy signal and 2) Design of the empirical Wiener filter where the filter brings back insignificant coefficients (noise) for consideration and scales them by minimizing the mean square error (MSE) [139-142]. Sandeep et al. [139] showed that the empirical Wiener filter improved wavelet denoising and outperformed other thresholding denoising algorithms. Wavelet transform decorrelate signal, and Wiener filter filtering of individual transform coefficients improved the signal estimate [139-142]. However, the limitation of wavelet-domain empirical Wiener filtering is that the approach requires two different wavelet transform bases. The effect on denoising the signals differs with different combinations of wavelet bases [139-142].

The WATV filter approach was proposed in the literature [126] to overcome the artefacts produced during denoising by modifying a single objective function. In addition, the WATV filter indirectly eliminates the need to select the appropriate wavelet transform bases required in the wavelet-based empirical Wiener filter. However, WATV still presents artefacts [127] after denoising the signal, particularly in the lung sound signal containing crackle.

Inspired by [123, 126, 127, 139], a novel approach (WATV-Wiener) to denoising and filtering the noisy lung sound signals was proposed in this thesis, which integrated WATV and the wavelet-based empirical Wiener filter effectively and uniquely. Firstly, WATV was synthesised and fine-tuned through case studies and was used to achieve a set of adequate denoised signal wavelet coefficients, and then the wavelet-based Wiener filter was designed to smooth the artefacts produced by the WATV denoising process. Additionally, the combination and integration of WATV and the Wiener filter have not been investigated and reported in the literature [123, 126, 127, 139], particularly in the acoustic lung signal domain.

4.3 Numerical Modelling and Problem Formulation

The lung sound model is based on the airflow transmission to the chest wall by the technique in the communication system and signal processing [143-145]. The lung sound model contains crackles and wheezes.

The lung sound is modelled as the flow source (airflow) hitting the airway [143-145]. When the airflow hits the airway, the lung sound is modulated by amplitude and frequency,

$$x_a(t) = x_s(t) m_a(t) m_f(t), \qquad (4.1)$$

where $x_a(t)$ is the output of airflow hitting on the airway, $x_s(t)$ is the airflow; the amplitude and frequency modulation functions are denoted as $m_a(t)$ and $m_f(t)$, respectively. The modulated airflow $x_a(t)$ is accompanied by noise $v_a(t)$ when it penetrates the airway wall, given as $x_f(t)$,

$$x_f(t) = x_a(t) + v_a(t), \qquad (4.2)$$

The noise from the sensor was also transferred, as is customary when noise from electronic devices is fed into the recording system [143-145],

$$x_r(t) = x_f(t) + v_f(t),$$

(4.3)

where $x_r(t)$ is the airflow transmitted out of the chest wall or the modulated signal with noises, and $v_f(t)$ is the noise transferred from the sensor, such as an electronic stethoscope. Noise is also produced by the ambient and other factors such as speech and cough during the lung sound recording,

$$y_r(t) = x_r(t) + v_e(t),$$

(4.4)

Where $y_r(t)$ is the airflow that is captured by the sensor with noise, and $v_e(t)$ is the noise caused by ambient. Substituting (4.1)–(4.3) into (4.4), the received lung sound containing noise is presented as,

$$y_r(t) = x_s(t) m_a(t) m_f(t) + v_a(t) + v_f(t) + v_e(t).$$

(4.5)

A reasonable assumption is that the noises are a zero-mean process having a probability density distribution that can be defined with mean and variance, uncorrelated with the transmitted lung sound $x_r(t)$, with varying SNR levels, similar to those classical signal denoising studies [126, 135, 141, 142]. Hence, the noises can be modelled as white Gaussian noise (WGN) [124, 127] and combined $v_a(t)$, $v_f(t)$, and $v_e(t)$. Therefore, (4.5) can be simplified to (4.6) similar to a linear system, where $y_r(t)$ is the received lung sound signal (output) containing WGN (error) $v_t(t)$ and the desired lung sound signal (input) $x_a(t)$ as in (4.1),

$$y_r(t) = x_a(t) + v_t(t).$$

(4.6)

From (4.6), the desired signal $x_a(t)$ is contaminated by noise $v_t(t)$ from the collisions of the airflow onto the airway, electronic devices, and ambient noise; thus, the noise have to be removed from the captured lung sound signal $y_r(t)$ through denoising. However, an inappropriate denoising method may introduce artefacts, particularly in the lung sound signal domain [127], which may lead to misinterpretation and affect the assessment. Thus, the

design of an optimal lung sound denoising technique is crucial for an accurate assessment [122, 146, 147].

4.4 WATV-Wiener Denoising Filter

A good denoised signal is achieved in [126], and [127] (low RMSE); however, defects such as the staircase effect still exist after denoising noisy lung sound signals [127], hence; the integration of the WATV-Wiener filtering technique was proposed to reduce ambient noise and smoothen the denoised signal further to achieve a better-denoised signal with higher SNR and insensitive to both high and low noise variance while maintaining the optimal RMSE performance.

The principle of the integrated filter is discussed in this section, starting with the synthesis of the WATV filter in Section 4.4.1, whereby the indirect approach of parameter tuning and selection will be discussed in Section 4.5.2, followed by the design of the empirical Wiener filter in Section 4.4.2. Lastly, the customised filter algorithm and block diagram are presented in Section 4.4.3.

4.4.1 Wavelet Threshold Total Variation Denoising

Wavelet transform W was first performed to (4.6) to achieve (4.7) [126], where n is denoted as the sample index, and the total number of samples N over a known time T is defined as $N = F_sT$, where F_s is the sampling frequency in this work,

$$\mathrm{W}y_r\left(n\right) = \mathrm{W}x_a\left(n\right) + \mathrm{W}v_t\left(n\right), \; n = 1, 2, \ldots N.$$

(4.7)

Equation (4.7) contains the entire signal coefficients $\mathrm{W}y_r(n)$ that contains dependable signal coefficients $\mathrm{W}x_a(n)$ and ambiguous signal coefficients $\mathrm{W}v_t(n)$. To accurately estimate the dependable signal coefficients from the signal coefficients $\mathrm{W}y_r(n)$ in (4.7), a 5-scale undecimated discrete wavelet transform W with two vanishing moments fulfilling the Parseval frame condition, and Daubechies filter (due to its translation-invariant property in denoising) with a low- and high-pass analysis filter was designed and applied onto the signal for denoising [126]. The "nonstationary" region of the lung sound signal produces significant wavelet transform coefficients (amplitude) over many wavelet scales. Most of the significant coefficients at each wavelet scale correspond to the desired lung sound signals, whereas the insignificant wavelet coefficients with small values, typically noise, are shrunk during

denoising. ω_c is denoted as the wavelet coefficients containing the signal x_t required for designing the empirical Wiener filter [126, 139],

$$\omega_c = \mathrm{W}x_t. \tag{4.8}$$

Thus, the estimation of signal x_t denoted as $\hat{x}_t$ can be obtained by inverse wavelet transform W^{-1} of wavelet coefficients ω_c once the estimated wavelet coefficients $\hat{\omega}_c$ is available [126],

$$\hat{x}_t = \mathrm{W}^{-1}\hat{\omega}_c. \tag{4.9}$$

The wavelet coefficients $\hat{\omega}$ in (4.9) can be identified in the following way: 1) split augmented Lagrangian shrinkage algorithm (SALSA) [131, 134] is applied to compute the wavelet coefficient in (4.10) with the condition that the wavelet coefficient between $1/2\|\mathrm{W}y_r - \omega_c\|_2^2 + \sum_{j,k_m} \lambda_j \phi(\omega_{c(j,k_m)}; \alpha_j)$ and $\beta\|DW^{-1}\omega_c\|_1$ are equal and 2) to achieve a balance between wavelet transform and TV denoising, they are controlled by a control parameter $0 < \eta < 1$ [126, 127]. The regularization parameter λ_j and TV parts β from (4.10), where σ is related to the WGN variance σ^2 in each wavelet scale j, is presented in (4.11) and (4.12), respectively [131]. From the regularization parameter λ_j above, the threshold shape controller is identified as $\alpha_j = 1/\lambda_j$.

$$\hat{\omega}_c(n) = \arg\min_{\omega_c}\left\{F(\omega) = \frac{1}{2}\|\mathrm{W}y_r - \omega_c\|_2^2 + \sum_{j,k_m} \lambda_j \phi(\omega_{c(j,k_m)}; \alpha_j) + \beta\|DW^{-1}\omega_c\|_1\right\}. \tag{4.10}$$

$$\lambda_j = 2.5\eta\sigma/2^{j/2} \tag{4.11}$$

$$\beta = (1-\eta)(\sqrt{N})/4\sigma \tag{4.12}$$

The indexed terms j and k are used to represent the scale and vanishing moment of the signal in the wavelet coefficients $\omega_{c(j,k_m)}$ respectively. The $\|DW^{-1}\omega_c\|_1$ can be defined as the total variation of signal estimation, where D is the first-order difference matrix. The single

indexed normalised wavelet coefficient is represented as, e.g., $\|x\|_1 = \sum_n |x_n|$, $\|x\|_2 = \sum_n |x_n|^2$. Doubly indexed normalised wavelet coefficient is denoted as, e.g., $\|\omega\|_2^2 = \sum_{j,k} |\omega_{j,k}|^2$.

4.4.2 Modified Empirical Wiener Filter

The obtained signal $\hat{x}_t$ is the estimated signal of the wavelet filter containing the lung sound of interest and dubious signal such as artefacts. The estimated reference signal $\hat{x}_a$ which is linearly related with $\hat{x}_t$, as shown in (4.13),

$$\hat{x}_a = \mathrm{W}^{-1} H \mathrm{W} \hat{x}_t. \tag{4.13}$$

The Wiener filter is designed to smooth the pilot estimation $\hat{\omega}_c$ in (4.10) to predict the remaining dubious coefficients; thus, the design of the Wiener filter in (4.14) estimates the entire signal coefficients consisting of both trustworthy and dubious coefficients,

$$H(n) = \frac{\hat{\omega}_c^2(n)}{\hat{\omega}_c^2(n) + \sigma^2}. \tag{4.14}$$

The coefficients estimate from (4.10) guarantees that the Wiener filter in (4.14) can further smooth the trustworthy coefficients in the pilot estimate of the wavelet coefficient $\hat{\omega}_c$ in (4.10) through the bias of the Wiener filter. Smoothing occurs when the wavelet coefficients $\hat{\omega}_c$ are larger than the noise variance σ^2. However, if the pilot estimate $\hat{\omega}_c$ is small or similar to the noise variance σ^2, the denoised signal has biases, leading to a significant gain ($H < 1$) in the MSE sense. Thus, the author can identify if the denoised wavelet coefficient is overly stretched with the Wiener filter by comparing WATV-Wiener and WATV RMSE results.

The estimated denoised wavelet coefficients $\hat{\omega}_c$ is applied to empirical Wiener filter design in (4.13) and (4.14) for smoothing and mitigating the artefacts by minimizing the RMSE to design an improved weighting profile in (4.14) [139].

4.4.3 WATV-Wiener Denoising Algorithm

Inspired by [126, 139], a unified wavelet threshold denoising filter (WATV) is first customised to reduce the interference noise, achieving an adequate denoised signal

coefficient from the lung sounds by estimating all wavelet coefficients (reliable and unreliable) concurrently. The estimated signal coefficient is fed into the empirical Wiener filter for smoothing by minimizing the denoised signal overall mean square error in the process of inverse filtering. WATV denoising strategy estimates all wavelet coefficients in (4.7) concurrently by computing the optimal single objective function in (4.10) to provide an estimate of x_a, denoted as x_t in (4.8) with the underlying understanding that dependable signal coefficients will survive thresholding and zeros most of the ambiguous signal coefficients. $\hat{x}_t$ is denoted as the pilot estimate related via (4.8) and (4.9) with the fundamental explanation that $\hat{x}_t$ contains estimates of dependable signal coefficients $\hat{\omega}_c$ and the modified empirical Wiener filter in (4.13) smooths $\hat{x}_t$ from artifacts output from the WATV filter. The signal coefficient $\hat{\omega}_c$ is treated as approximate maximum posteriori estimation of variance to design an empirical Wiener filter H in (4.14) to smooth the remaining ambiguous signal coefficients from $\hat{\omega}_c$ which resulted from the artifacts produced from WATV denoising strategy, and thus output an estimated desired signal $\hat{x}_a(n)$ through the signal coefficient $\hat{\omega}_c$ [126, 127, 139-141]. The proposed technique is summarised in Figure 4.3.
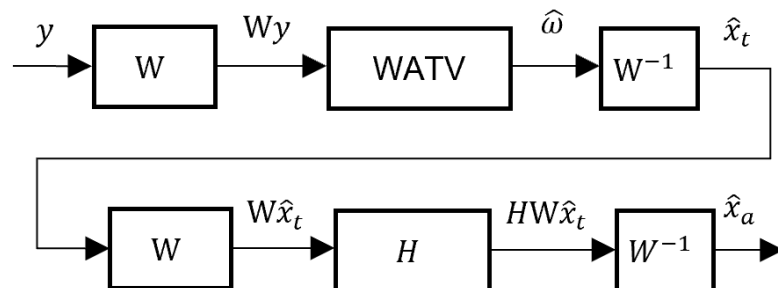
Figure 4.3   **Hybrid technique of WATV and wavelet-based empirical Wiener filtering.**

From Figure 4.3 and (4.7)–(4.14), the estimated denoised signal $\hat{x}_t$ is applied from WATV to obtain an adequate signal coefficients estimate $\hat{\omega}_c$ instead of deciding on two wavelet transform bases to obtain an optimal empirical Wiener filter [126, 127, 139-141]. The Wiener filter further reduces the ambiguous signal coefficient that produces artefacts from the WATV. The approach has been simplified into a linear system instead of the dual wavelet transform and smooths the signal through the additional empirical Wiener filter. The pseudocode of the proposed WATV-Wiener algorithm is shown in Figure 4.4.

Input: Noisy data (y_r); Number of vanishing moment (k_m); Regularization parameter (λ_j); TV parts (β); Step size (μ); Number of wavelet scale (j); Number of iterations ($niter$), Threshold function (θ) Wavelet transform (W); Wavelet coefficient (ω_c).

Output:

1: Initialisation: $\omega_c = W y_r$;

2: Identifying wavelet coefficient in (4.10) by iteratively minimizing with respect to ω_c and u with variable splitting and augmented Lagrangian approach.

3: $u = \omega_c$; $d = \omega_c$; $c = 0$;

4: Iteration till convergence between $\boldsymbol{\omega_c}$ and $\boldsymbol{u}$.

5: **For** $i = 1{:}niter$

6: $p_{j,k} = [W y_r + \mu(u - d)]/(1 + \mu)$

7: Finding the wavelet coefficient ω_c for all j, k_m with the input from $\theta, p, \lambda_j, \mu$, $a_j = 1/\lambda_j$

8: $\omega_{c(j,k)} = \theta\big(p_{j,k}; \lambda_j/(1+\mu); a_j\big)$

9: $c = d + \omega_c$

10: Total variation denoising (tvd) requires data input from c, length of the data input (N) and TV parts

11: $d = W[W^{-1} v_t - tvd(W^{-1}c; N; \beta/\mu)]$

12: $u = c - d$

13: $d = d - (u - \omega_c)$

14: **end For**

15: Denoised wavelet coefficient ($\widehat{\omega}_c$), where the signal $\hat{x}_t = W^{-1}\widehat{\omega}$

16: Empirical Wiener filter design for smoothing: H

17: $H = \widehat{\omega}_c{}^2/\big(\widehat{\omega}_c{}^2 + \sigma^2\big)$

18: Smooth denoised output: $\hat{x}_a = W^{-1} H W \hat{x}_t$

Figure 4.4   **WATV-Wiener algorithm.**

4.5 Lung Sound Modelling and Simulation Studies

The modelling of both healthy and adventitious lung sound signals x_s shown in (4.1) is expressed in Section 4.5.1 [143-145], followed by the optimisation and evaluation of filter parameters affecting the overall proposed filter performance in the SNR sense, which were demonstrated in Section 4.5.2. In Section 4.5.3, the simulated noisy lung sound signals shown in Figure 4.5 were fed into the optimised WATV-Wiener filter, and seven other state-of-the-art filters that had shown good SNR or RMSE results in the literature for denoising and performance comparison in terms of SNR and RMSE [123, 126-131]. The sampling frequency is set to $F_s = 4000$ Hz in this research, and performed 500 simulation runs on denoising lung sound signals at each noise level. Analyses were performed offline through MATLAB R2019b in the simulation studies.
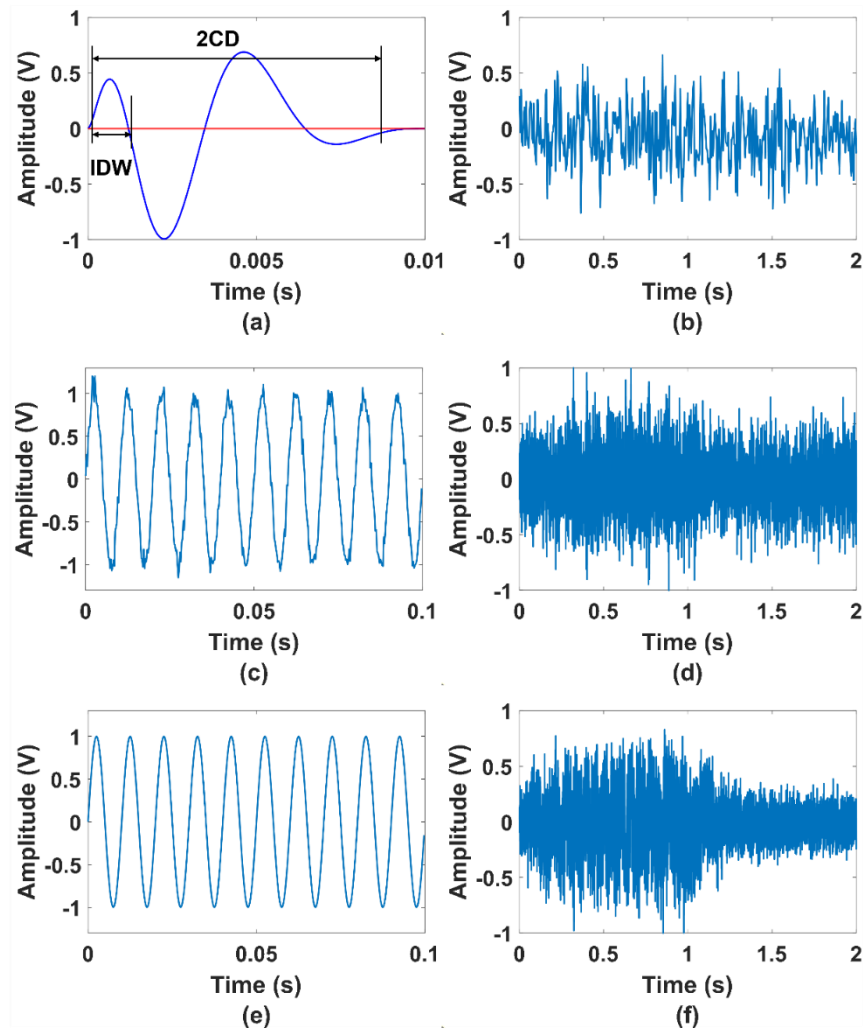
Figure 4.5 **Simulated lung sound signals transmitted out of the chest wall, corrupted with additive WGN as the noise component $v(t)$. (a) Simulated airflow source crackle; (b) Lung sound signal containing crackle transmitted onto chest wall with additive WGN; (c) Simulated airflow source wheeze; (d) Lung sound signal containing wheeze transmitted onto chest wall with additive WGN; (e) Simulated healthy lung sound; and (f) Healthy lung sound signals are transmitted onto the chest wall with additive WGN.**

RMSE and SNR were utilised as performance metrics after denoising the observed lung sound signal y_r in (4.6). The RMSE is determined by employing the amplitude of denoised and noise-free signals and expressing the differences in root mean square sense shown in (4.15). SNR is defined by finding the ratio of denoised signal peak amplitude to noise peak amplitude and expressed the ratio using the logarithmic decibel scale in (4.16), where x_e is the noise-free simulated signal, y_s is the simulated noisy signal, and d is the denoised signal.

$$\text{RMSE} = \sqrt{\text{mean}\left[\left(d - x_e\right)^2\right]}, \tag{4.15}$$

$$\text{SNR}=20\left[\log\left(\frac{d}{y_s - x_e}\right)\right],$$ (4.16)

4.5.1 Synthesis of Lung Sound with Crackle and Wheeze, and Healthy Lung Sound

To obtain both adventitious and healthy lung sound shown in (4.1) and depicted in Figure 4.5(a), Figure 4.5(c), and Figure 4.5(e), airflow source $x_s(n)$ is first modulated by the frequency modulation m_f cosine wave in (4.17) with an amplitude of 1 V, and frequency of $F = 400$ Hz, followed by the amplitude modulation m_a sawtooth wave in (4.18) with an amplitude of 1 V amplitude, and frequency of $F = 400$ Hz [143, 144]. The noise v_t from (4.2)–(4.6) and shown in Figure 4.5(b), Figure 4.5(d), and Figure 4.5(f) is presented last in this 4.5.1.

$$m_f(n) = \cos\left(2\pi\left(F/F_s\right)n\right),$$ (4.17)

$$m_a(n) = \frac{1}{2} - \frac{1}{\pi}\sum_{k_a=1}^{5}\frac{1}{k_a}\sin\left(k_a\pi\frac{F}{F_s}n\right),$$ (4.18)

where k_a is the order of harmonics of amplitude modulation.

Employing the equations proposed in [148], adventitious airflow (crackle) transmitted to the airway is simulated using (4.19) and (4.20). The crackling signal $x_s(n)$ is presented as two periods, and the crackle modulation function in (4.20) is employed to shift the energy of $x_s(n)$ to the initial part of the shape. Figure 4.5(a) presented the simulated crackle, with initial deflection width (IDW) = 1.2 ms and two cycle duration (2CD) = 9.8 ms [144, 148],

$$x_s(n) = \left[\sin\left(4\pi n^\alpha\right)\right]m_c(n), \ \alpha = \frac{\log(0.25)}{\log(0.12)},$$ (4.19)

$$m_c(n) = 0.5\left\{1+\cos\left[2\pi\left(n^{0.5}-0.5\right)\right]\right\}.$$ (4.20)

Synthesis of wheeze as airflow source $x_s(n)$ [145] and then transmitted to the airway $x_a(n)$ is presented in (4.21). The airflow source $x_s(n)$ for wheeze was simulated as a pure sine wave with 1 V amplitude, $F = 100$ Hz, and WGN at 50 µW [145]. The simulated wheeze is presented in Figure 4.5(c),

$$x_s(n) = \sin\left(2\pi\left(F/F_s\right)n\right) + v_w(n),$$

(4.21)

where $v_w(n)$ is the WGN for wheeze airflow source. The synthesis of healthy lung sound signals is shown in (4.22) [145], similar to wheeze in (4.21) except for the insertion of WGN and presented in the simulated healthy lung sound in Figure 4.5(e),

$$x_s(n) = \sin\left(2\pi\left(F/F_s\right)n\right).$$

(4.22)

The modulation's accompanying noises $v_a(n)$ were inserted into the acoustic signals in (4.19), (4.21), and (4.22) that penetrate to the airwall shown in (4.2), with WGN power level and SNR at 0.6 dBm and 0.01 dB [145], respectively. The parameters chosen demonstrated that the proposed communication model corresponds with the physiological characteristics of the actual lung sounds [145]. Finally, the microphone received sound combined with the WGN $v_f(n)$, power at 10^{-6} dBm, as is usually the case in electronic communication [143-145]. From the above noise parameters, in an uncontrolled environment, the electronic noise $v_f(n)$ is dominated by the noise produced internally by the airway wall and ambient interference. However, in a quiet and controlled environment, the situation of the electronic noise may have a different impact on the simulation studies. Thus, the noise power is included in the simulation studies, consistent with the literature simulation studies [143-145].

The WGN is generated at various SNRs and were employed as the noise component $v_t(t)$ in (4.6), similar to [127] and [145]. The SNR values is varied between 0 dB and 20 dB with a 2 dB increment rate resulting in 11 noise levels. Each noise level on the individual simulated lung sound signals is superimposed, which gave the observed physiological signals $y_r(t)$ in (4.6) and presented in Figure 4.5(b), Figure 4.5(d), and Figure 4.5(f), with a specific SNR. From Figure 4.5, the similarity between the simulated signal and the actual noisy signal captured in an uncontrolled environment with an electronic stethoscope and microphones in the literature [123, 135] can be observed.

4.5.2 Tuning of Parameters for Optimising the WATV-Wiener Filter

The simulations were tailored to optimise the overall filter performance by modifying three parameters η, σ, and N that influence the TV parts β and regularization parameter λ_j from (4.10) to (4.12). In (4.10), both β and λ_j control the pilot estimation of the denoised wavelet coefficients in the proposed technique. As the pilot estimation affects the designing of the empirical Wiener filter and the overall filter performance; hence, the pilot estimation of the denoised wavelet coefficients is critical. The parameter η estimates were available in the literature; however, no case studies on how the parameter adjustment affects the filter performance, particularly in the lung sound signal domain, were attempted or discussed [126, 127]. In addition, the literature has not discussed the filter's SNR performance in recovering signals of interest from noisy lung sound signals [126, 127]. Thus, to evaluate the effect of the parameter η on the overall filter, the performance of the denoised noisy lung sound signals will be compared in the SNR sense.

In the initial investigation into optimizing SNR performance, three possible simulation case studies were evaluated through adjusting η, while keeping $\sigma = 10$ and the total number of samples $N = 4000$. In the first demonstration, the author kept $0.76 < \eta < 1$, e.g., $\eta = 0.80$, $\eta = 0.90$, which resulted in $\sum \lambda_j > \beta$. Next, the author adjusted $0 < \eta < 0.76$ to a lower value, e.g., $\eta = 0.2$, $\eta = 0.5$, resulting in $\beta > \sum \lambda_j$. Lastly, the author balanced both $\beta \approx \lambda_j$ with $\eta = 0.76$. The mean SNR improvement with respect to the ratio between TV parts and regularization parameter in the three explored scenarios were demonstrated in Figure 4.6. The SNR performance of the filter is at the lowest when $\beta > \sum \lambda_j$, with a ratio < 1, and achieved the best SNR performance when $\sum \lambda_j = 3\beta$, at $\eta = 0.90$.

The author has identified that the condition $\eta = 0.90$ as a baseline for optimising the SNR performance from the results in Figure 4.6. An additional observation from the TV parts β in (4.12) and the regularization parameter λ_j in (4.11) wherein they were also determined by the total number of sample N. Typical lung sound signals comprised of minimally two respiratory cycles with time $T \approx 4$ s, $F_s = 4000$ Hz in the literature [120, 135, 145]. Hence, the author adjusted the total number of samples N to the lung sound signals to determine if N affects the overall filter performances. The mean SNR performance with respect to N with the parameters in the initial investigation, e.g., $\eta = 0.90$, $\sum \lambda_j / \beta = 3$ is presented in Figure 4.7.
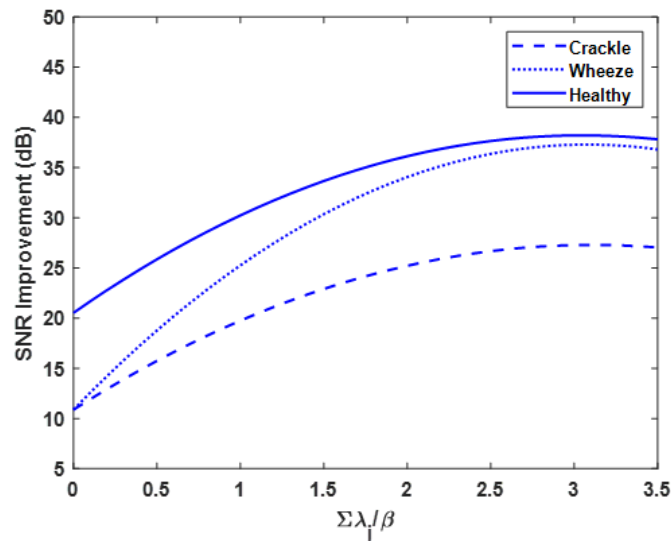
Figure 4.6 **Impact of the ratio of TV parts and regularization parameters on the SNR performance of the WATV-Wiener filter.**

The performance of the WATV-Wiener filter was not affected by the total number of samples presented in Figure 4.7 in terms of SNR performance compared to Figure 4.6 and showed a similar SNR performance trend at the ratio $\sum \lambda_j = 3\beta$, with $\eta = 0.90$ regardless of number of signal samples.
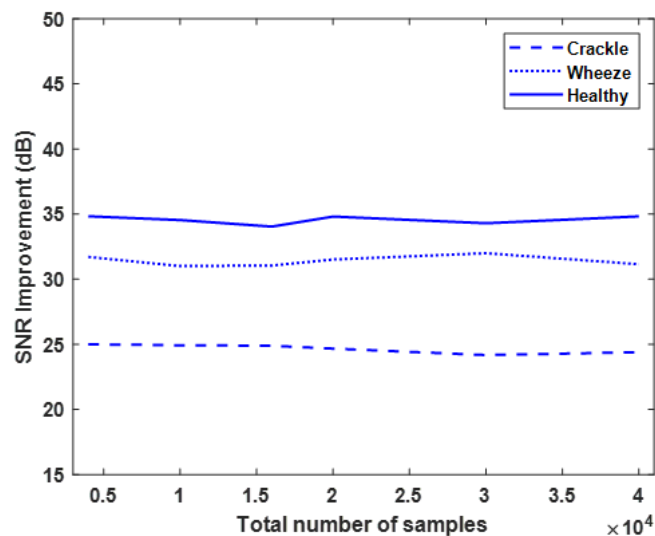
Figure 4.7 **Impact of baseline parameter $\eta = 0.90$ on the various total number of samples N in terms of the denoising SNR performance.**

As the parameter η range between 0 and 1, the author has identified $0.9 < \eta < 1$ as a baseline parameter from Figure 4.6 and Figure 4.7 discussed above. The remaining question is, what

is the optimal parameter range in η for the filter? Thus, to present the optimizing of parameter η from the baseline parameters identified from the case studies, the author set different possible combinations of parameter η, e.g., $\eta = 0.90$, $\eta = 0.95$, and $\eta = 0.99$ to evaluate the optimal SNR performance of the overall filter on different noisy lung sound signals and presented the result in Figure 4.8. An optimal SNR parameter is achieved, as observed from Figure 4.8. WATV-Wiener filter obtained higher improved SNR by 3–8 dB with $\eta = 0.95$ compared with [126] and [127] estimated parameter, and the initial investigation $\eta = 0.90$, and the SNR performance is similar for both $\eta = 0.95$ and $\eta = 0.99$, with a variation of 1 dB. In addition, WATV-Wiener performed better in terms of SNR with the single setting of $\sum \lambda_j > \beta$ with $0.95 \leq \eta < 1$ compared to the other case settings shown in Figure 4.6–Figure 4.8.

From the case studies, optimal SNR results were obtained in Figure 4.6–Figure 4.8; the author recommend the following optimised parameters for denoising typical lung sound signals by tuning $\sum \lambda_j = 3\beta$ with $0.95 \leq \eta < 1$.
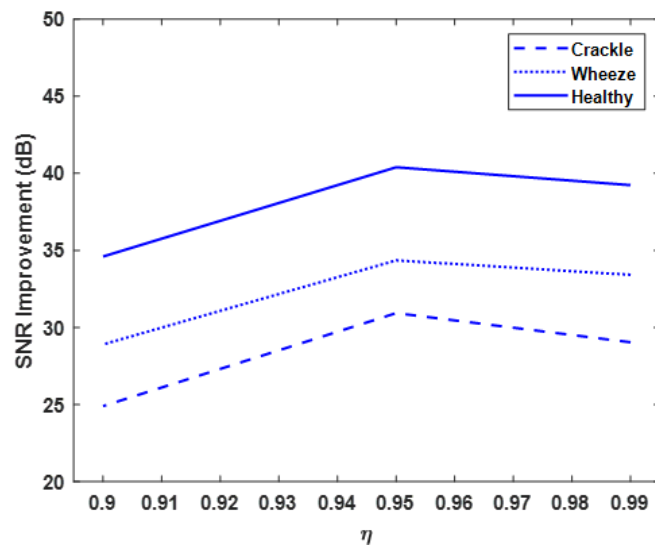
Figure 4.8   **The impact of parameter η on the WATV-Wiener filter denoising SNR performance.**

Ultimately, the denoised signal ought to retain waveform characteristics of interest without overly deforming the lung sound signals. Thus, the author set the ideal parameter $0.95 \leq \eta < 1$ to denoise noisy lung sound signals with different noise variances and presented the RMSE result in Figure 4.9. The proposed filter achieved consistent RMSE results with different noise variance in the system in Figure 4.9, showing robustness to the noise variance.
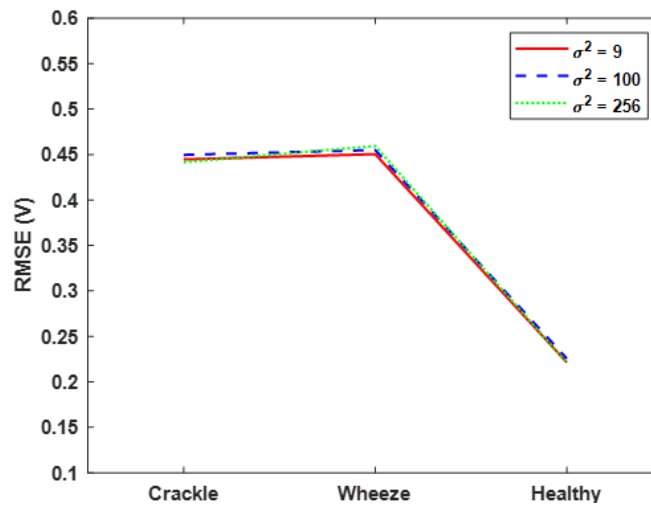
Figure 4.9   Average RMSE of denoised lung sound signals with various noise variance in the lung sound signals.

4.5.3 WATV-Wiener Filter Fine-tuned Parameters Performance Evaluation and Discussion

Optimal quantitative findings such as SNR of certain prior denoising approaches may seem promising, but the inappropriate selection of parameters, e.g., in the wavelet thresholding, may result in a high SNR, albeit evident artefacts are introduced in the signal processing. Thus, RMSE is essential in identifying that the denoising filter retains the frequencies of interest and waveform characteristics. In the literature, WATV is an optimal denoising filter in the RMSE sense [126, 127, 149]. The research goal is to denoise the signal without affecting the waveform characteristics while improving the SNR; thus, with the parameters identified in the optimal tuning study, $0.95 \leq \eta < 1$, the WATV-Wiener filter was compared with other established lung sound signal filters in the literature [123, 126, 128-131], and [127] and presented the mean RMSE and SNR results in Figure 4.10(a)– Figure 4.10(c), and Figure 4.10(d)–Figure 4.10(f), respectively. The simulated lung sound signals have the following parameters: noise variance $\sigma^2 = 9$, $F_s = 4000$ Hz, and the total number of samples $N=16000$.

WATV denoising filter is optimal in terms of RMSE from the observation in Figure 4.10(a)– Figure 4.10(c), achieving mean RMSE of 0.43 V, 0.47 V, 0.21 V in adventitious lung sound signals containing crackle and wheeze, and healthy lung sound signals, respectively, consistent with the findings in the literature [126, 127, 149]. WATV-Wiener shadows WATV sharply, within ±0.02 V, or within 10% in the absolute relative change in terms of optimal RMSE, and performed better by 0.2–0.7 V compared to remaining filters, i.e., BP,

Soft, Hard, Serial, and TV. From Figure 4.10(d)–Figure 4.10(f), WATV-Wiener obtained the best mean improved SNR of 38.09 ± 0.80 dB, 41.03 ± 0.79 dB, 47.56 ± 0.73 dB in crackle, wheeze, and healthy lung sound signals, respectively. From the results in SNR and RMSE, the BP filter has the lowest SNR performance and worse RMSE results; the reason could be due to denoised lung sound signals containing overlapping noise spectral. The finding in RMSE is consistent with the literature where a single linear infinite impulse response or FIR-based filter may not be sufficient to denoise a noisy signal, and the noise affects the waveform characteristics [128, 135].

From the SNR and RMSE results in Figure 4.10, the WATV-Wiener filter can achieve optimal RMSE results similar to the optimal RMSE-sense WATV and further achieved higher noise removal in terms of SNR by another 5–20 dB compared to other established lung sound signals filters. From the RMSE and SNR results, WATV-Wiener showed it could retain waveform characteristics (low RMSE) while improving SNR from denoising various inputs of SNR lung sound signals, showing robustness to severe noise. The WATV-Wiener performance benefits achieved could be due to the optimised pilot estimation of the wavelet coefficient $\widehat{\omega}_c$ and smooth the pilot denoised wavelet coefficient with the complementing diagonal weighting matrix H from the empirical Wiener filter. As shown in Figure 4.8–Figure 4.10, without the optimal parameters in the pilot estimation of the denoised wavelet coefficient, the integration of the WATV filter and empirical Wiener filter may not have achieved optimal denoised lung sound SNR performance. WATV estimates the wavelet coefficients $\widehat{\omega}_c$ by considering both insignificant (noise) and significant (signal) coefficients, the author used the estimated signal estimates from WATV to design an empirical Wiener filter H to smooth and reduce the artifacts on the denoised signal. The empirical Wiener filter scales the coefficients by minimizing the MSE to design an improved weighting profile $H \approx 1$, with a WATV coefficient more significant than the noise variance, $\widehat{\omega}_c \gg \sigma^2$. Thus, pilot estimation of the denoised wavelet is critical to improving the proposed filter's weighting profile. The proposed hybrid technique can decrease the denoised signal's bias and achieve an optimal filter in SNR performance. Under the condition of the noise variance σ^2 is greater than the estimated denoised signal $\widehat{\omega}_c{}^2$, the weighting profile will contribute to the gain in wavelet coefficient resulting in a lower SNR performance.
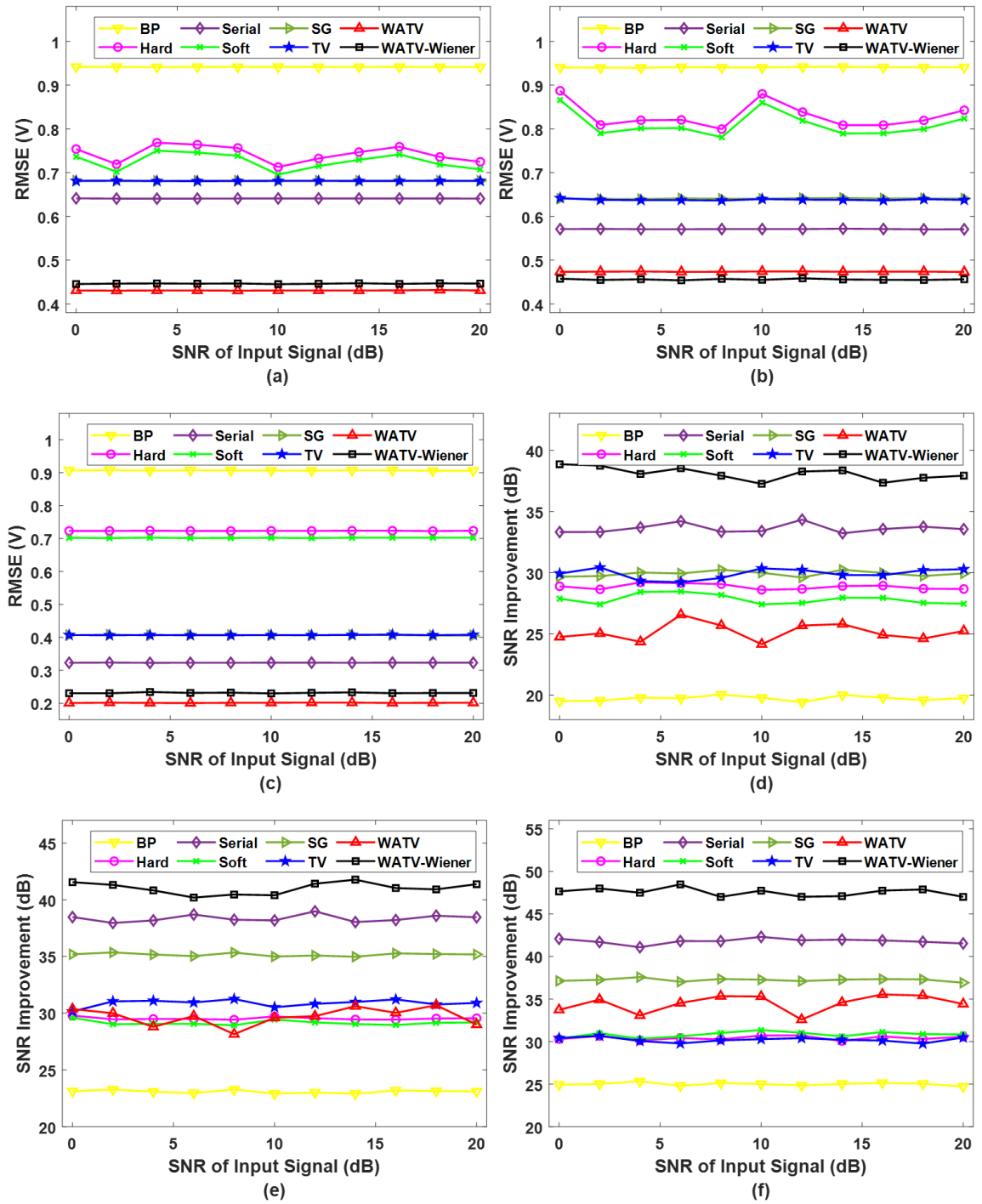
Figure 4.10 Average RMSE (a)-(c) and SNR improvement (d)-(f) of denoised healthy and adventitious lung sound signals to various SNR values of the input signal. (a), (d) Lung sound signal containing crackle; (b), (e) Lung sound signal containing wheeze; and (c), (f) Healthy lung sound signal.

4.6 Experimental Studies

To ensure the denoising performance stability of the WATV-Wiener filter between the simulation studies and actual respiratory sound, the WATV-Wiener filter was quantitatively compared with other prominent filters in the literature, similarly to the simulation studies, in the denoising experiment studies [123, 126-131].

Healthy volunteers was shortlisted in the experimental studies with their verbal consent and no history of respiratory diseases in the past 1 month. 10 healthy lung sound signals was collected from volunteers with the system presented in Section 4.5.1. and evaluated the system SNR performance compared to a commercial product used for capturing lung sound signals. The experiment was performed in an uncontrolled environment with an average 59 ± 0.54 dBA sound pressure level, similar to a hospital noisy intensive care unit, where emergency alarms, communications, and critical care are often happening [150].

Due to the pandemic situation globally, the author could not get actual respiratory patients for the experiment. Hence, 17, 10, and 13 unhealthy lung sound signals containing crackle, wheeze, or both crackle and wheeze (mixed) were shortlisted from an open-access respiratory database [104], respectively. The respiratory database [104] contained adventitious lung sound signals (crackle, wheeze) from volunteers diagnosed with COPD, asthma, and respiratory tract infection. The respiratory database [104] captured volunteers' respiratory sounds by digital stethoscope or an array of MEMS microphones in a clinical or home setting, with qualified independent reviewers annotating the signals. The signals also contain cough, speech, and throat clearing. The shortlisted respiratory signals have a minimum sampling frequency of $F_s = 4000$ Hz, and a minimum recording time of $T = 10$ s. A total of 50 recordings from the captured healthy lung sound signals and the shortlisted respiratory signals are passed through the denoising filters to estimate the denoised signal's SNR output.

Before denoising, a bandpass filter ranging from 150 Hz to 1300 Hz has been applied to remove other major artefact events such as cough and throat clearing. All patients in the respiratory signal database had COPD with comorbidities, i.e., heart failure. Hence, signals below 150 Hz are excluded. A maximum of 1300 Hz was chosen as the upper bandpass limit in the article as $F_s = 4000$ Hz to avoid aliasing effects. In the literature, healthy, wheeze, and crackle frequency signal falls within the bandpass range of 150 Hz to 1300 Hz [120-122,

145]; thus, it should be sufficient to retain the interest frequency range and adventitious lung sound characteristics after denoising.

The estimated noise variance [151] is about $\sigma^2 = 0.05$ ($\sigma = 0.23$) from the healthy lung sound signal measurement in the experimental studies. The lung sound signals was resampled with a sampling frequency of $F_s = 4000$ Hz, and applied $\sigma = 0.23$, and the optimal parameter evaluated from the simulation studies, $\eta = 0.95$ to the experiment analysis as the sound pressure level for capturing the healthy lung sound signals and the database is similar. The static and ambient noise in the database may be different from the captured lung sound signals; however, the author has also demonstrated earlier that the WATV-Wiener filter is insensitive to noise variance in the simulation studies, achieving similar SNR and RMSE performance in both low and high noise variance with $0.95 \leq \eta < 1$.

The computation of RMSE for the captured lung sound signals in was presented (4.23), the SNR for the captured lung sound signals, and the database in (4.25) and (4.26), respectively,

$$\text{RMSE}_{system} = \sqrt{\text{mean}\left[\left(d - x_n\right)^2\right]},$$ (4.23)

where d denotes the amplitude of denoised lung sound signals, x_n represents the amplitude of noise-free lung sound signals given in (4.24),

$$x_n = a_s - a_n,$$ (4.24)

where the captured lung sound signals with noise and captured ambient noise without lung sound signals are denoted as a_s and a_n, respectively. The computation of SNR in (4.25) and (4.26) is similar to (4.16), defining SNR by finding the ratio of denoised signal peak amplitude to noise peak amplitude and expressing the ratio using the logarithmic decibel scale.

$$\text{SNR}_{system} = 20\left[\log 10\left(\frac{d}{a_n}\right)\right],$$ (4.25)

where a_n is the noise peak amplitude from the system electronic static noise and ambient noise without lung sound signals, and d denotes the filter denoised signal peak amplitude. There is a slight modification for the computation of database SNR in (4.26) as noise is unavailable; thus, "noise" is defined as subtracting the denoised signal from the noisy signal,

$$ \text{SNR}_{database} = 20 \left[\log 10 \left(\frac{d}{f_y - d} \right) \right], \tag{4.26} $$

where, f_y is the noisy signal peak amplitude from the database, and d is the denoised signal peak amplitude.

4.6.1 Acoustic Signal Acquisition

The motivation to assemble an acoustic sensor-based MEMS for capturing lung sounds is that a MEMS sensor is cheaper, a few dollars per piece compared to an electronic stethoscope, hundreds of dollars, particularly when an array of sensors is required to capture the acoustic signals. The author assembled the system shown in Figure 4.11 to record the lung sound signals, and the design specifications are similar to [118-120, 152], and [150]. The primary module of the equipment is a high SNR microelectromechanical system (MEMS) microphone with a frequency response between 50 Hz and 20 kHz. The sampling frequency of the MEMS microphone is 44100 Hz, and the MEMS sensor consists of a signal conditioning function, an analogue-to-digital converter, decimation and anti-aliasing filters, power management, and an industry-standard 24-bit time-division multiplexing interface.
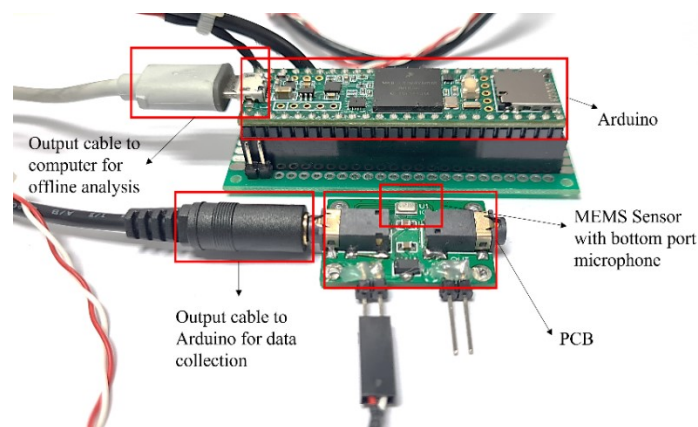
Figure 4.11   Lung sound recording equipment.

3M electronic stethoscope has "proprietary" ambient noise reduction technology that eliminates an estimated 85% of ambient background noise interference without eliminating critical lung sounds. Therefore, the author benchmarks the system performance against a 3M electronic stethoscope. The SNR computation for the system and 3M electronic stethoscope can be expressed as,

$$\text{SNR} = 20\log\left(\frac{\bar{a}_s}{\bar{a}_n}\right),$$
(4.27)

where, $\bar{a}_s = \sum (a_s - a_n)/\text{J}$ represents the mean peak amplitude of the signal, and $\bar{a}_n = \sum a_n/\text{J}$ is the mean peak value of the collected noise without lung sound signal from the MEMs sensor and 3M electronic stethoscope. a_s is the peak amplitude of the collected lung sound signal with noise, a_n is the peak value of the collected noise without lung sound signal, and $\text{J} = 10$ is the number of collected signals. An estimated SNR of 71.63 dB and 68.73 dB was obtained from the system and 3M electronic stethoscope, respectively. The sensor device can perform similarly to a commercial 3M electronic stethoscope in terms of SNR.

4.6.2 Experiment Results and Discussion

The denoised experimental lung sound signals RMSE and SNR was summarised in Figure 4.12 and Figure 4.13, respectively. The frequency spectrum of the denoised experimental lung sound signals is presented in Figure 4.14, where the mean frequency of interest is about 405 ± 10.57 Hz. From Figure 4.12, WATV-Wiener achieved a similar optimal RMSE of 0.1933 V compared to the optimal WATV filter in the RMSE sense at 0.1938 V, achieving an absolute relative change of about 0.26%. In addition, a similar trend from the simulation studies can be observed, particularly in the BP filter, where noise presence in the overlapped spectral may affect the overall filter signal quality, resulting in a high RMSE result of 0.99 V. Altogether, the WATV-Wiener filter achieved better and optimal RMSE results by about 0.1–0.8 V as compared to other filters such as BP filter, Hard filter, Serial filter, Soft filter, SG filter, and the TV filter.

Further evaluation of denoising filter performance from Figure 4.13 showed that the WATV-Wiener filter improved SNR by about 4–30 dB compared to other denoising filters, consistent with the simulation study findings (5–20 dB). As noise might be present in the denoised signal from BP filter as observed from the healthy lung sound RMSE results in Figure 4.12, which resulted in the large range of SNR improvement in adventitious lung

sound signals from Figure 4.13. WATV-Wiener improved SNR by about 44 dB in healthy lung sound signals, consistent with the SNR results in the simulation studies.
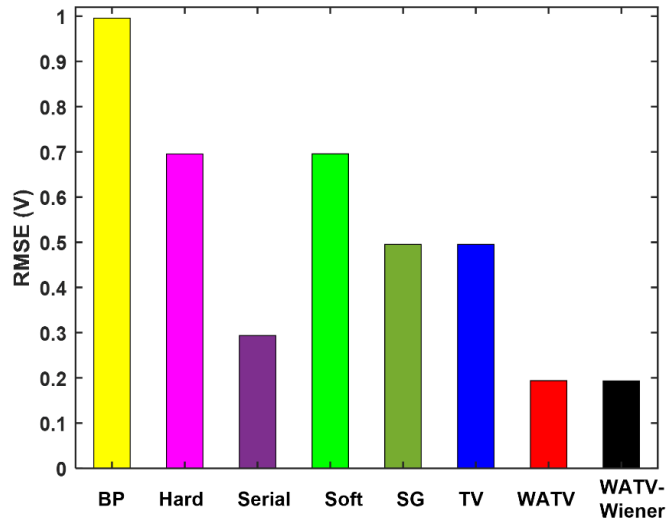
Figure 4.12 **Denoised filter RMSE performance in captured healthy lung sound signals.**
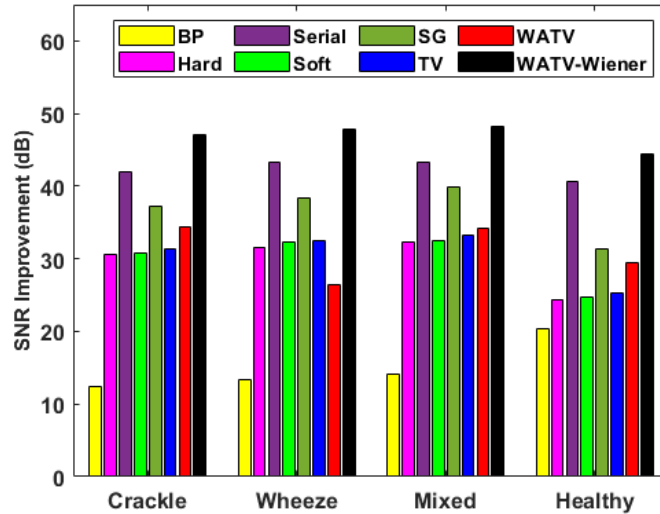
Figure 4.13 **Denoised filter SNR performance in actual healthy lung sound signals, and adventitious lung sound signals containing crackle, wheeze, or mixed of both crackle and wheeze.**
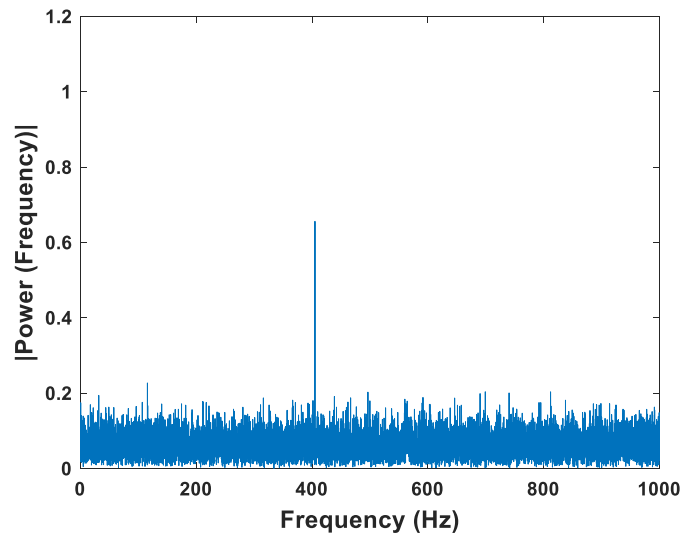
Figure 4.14   Single-sided frequency spectrum of a denoised lung sound signal.

It is known that denoising continuous piecewise signal, e.g., healthy, and wheeze is more straightforward than denoising noncontinuous piecewise signal, e.g., crackle; however, the author has achieved similar performance in terms of improved SNR, about 49 dB between crackle and wheeze in the experimental studies. From the experimental results, the WATV-Wiener filter functions better than the WATV filter in denoising noisy signals achieving optimal RMSE, and improving the SNR, and the noise variance has minimal effect on WATV-Wiener.

The proposed denoising filter achieved better (optimal) RMSE results by 0.1–0.8 V in the actual healthy lung sound signals than other filters, similar to the simulation studies (0.2–0.9 V). Moreover, the proposed denoising filter achieved similar improved SNR for healthy lung sound signals between the simulation studies and experiment at about 3–20 dB with the optimal parameters. It can also be seen from the data in Figure 4.13 that the improved SNR of about 4–30 dB was attained for adventitious (crackle, wheeze, mixed) lung sound signals. The improved SNR in the experiment studies (4–30 dB) is higher than the improved SNR in the simulation studies (5–20 dB) could be attributed to the modified computation of SNR as shown in (4.26), where noise is defined as the differences between denoised lung sound signals and observed noisy lung sound signals. Although a difference of 10 dB in improved SNR for crackle and wheeze is observed between the experiment and simulation studies, the minimal difference can be further reduced if noise data is available in the database. "Noise data" is typically available in practice and usually referred to as using a sensor to capture the static electronic interference and ambient noise without lung sound signals, similar to the system's captured noise a_n in (4.25), and in the literature [120, 123, 135].

The optimal results obtained by the WATV-Wiener filter could be 1) due to the advantage of wavelet-based denoising in noncontinuous piecewise signal, and 2) the optimal integration of two ideal filters, particularly in the RMSE sense, by addressing different challenges faced individually, e.g., WATV eliminates the requirement of selecting two different wavelet transform bases compared to empirical Wiener filter, but introduces artefacts, and empirical Wiener filter (known for eliminating artefacts through minimizing MSE) to remove the artefacts introduced by WATV [126, 131, 139].

In denoising actual lung sound signals, the WATV-Wiener filter algorithm comprises two primary filters: a bandpass filter ranging from 150 Hz to 1300 Hz and an integration of WATV and Wiener filter. Each step of the filter handles different components of noises. The FIR bandpass filter reduces most high- and low-frequency noises such as cough, speech, and environment, which accounts for most of the noises in actual lung sound signals. However, with the overlapped noise frequency, a single linear filter cannot eliminate all the noise in the stopband [128, 135]. The WATV-Wiener filter segments the signal into different frequency regions in the wavelet domain and estimates all wavelet coefficients, both reliable and unreliable, in parallel, minimizing the denoised signal overall mean square error in the process of inverse filtering. The remaining high-frequency and low-frequency noises and environmental noise that has overlapping frequencies with signals of interest and are not removed by the bandpass filter are reduced without distortion of the lung sounds, as shown in the results from Figure 4.12 and Figure 4.13.

In addition, the WATV-Wiener filter can identify the signal acoustic features of lung sounds in terms of RMSE, as shown in Figure 4.12. Thus, the WATV-Wiener filter is helpful for further pattern recognition research and can help clinicians identify the condition of the patient's lungs based on observed acoustic features. Moreover, the WATV-Wiener filter enables the investigation and auscultation of several lung sounds that were previously inapplicable due to the weak acoustic features. The respiratory characteristics are often too weak to determine the condition of the lungs because of the inadequate ideal (noise-free) signal measuring environment. For instance, the WATV-Wiener filter helps expose the signals in relation to noise without compromising the characteristics of interest in the lung sound signals and makes denoised signals contain strong enough features in the judgment of lung conditions in terms of SNR, as shown in Figure 4.13.

4.6.3 General Discussion

However, some limitations must be considered with this research. Firstly, on account of the overlapping frequency between lung sound signals and heart sound signals. This work focused on denoising environmental noises, while the separation of heart sound signals and lung sound signals was not considered. To obtain reference lung sound signals, the lung sound signals from both the measurement system and the shortlisted lung sound signals from the respiratory database were recorded on the patient's posterior to ensure that the heart sound signal will be minimal and does not interfere significantly with the lung sound signal. Additionally, 150 Hz – 1300 Hz BP filtering was applied to the actual lung sound signals to eliminate the lower heart sound frequency. While these frequency bands contain the majority of interesting lung sound characteristics, there can still be prominent unwanted heart sounds inside the frequency band. Therefore, to more accurately replicate the frequency overlap between heart sound signals and lung sound signals and assess the WATV-Wiener filter robustness in sound separation methods between lung and heart signals, pure and unfiltered reference lung and heart sound signals would be required.

The second correlated limitation is with the signal quality estimation of the respiratory database shown in (4.26). Although (4.26) strives to evaluate the denoised signal power in relation to noise quantitatively, it was not error-free. As noise is unavailable, the assumption for noise was made by subtracting the denoised signal from the original noisy signal. Hence, the differences between denoised lung sound signals SNR results from the respiratory database and the simulation studies can be explained with this limitation. The overall performance of the WATV-Wiener filter does not directly consider if significant portions of the heart sound components are also being removed to obtain noise-free sounds. In the general utilization of the algorithm, the frequency domain of pulmonary sounds is relatively stable. The normalization wavelet method based on the signal power against noise significantly improves the integration of the WATV-Wiener filter. Besides, the integration of the WATV-Wiener filter proposed in this work shows a good effect in denoising without distortion.

4.7 Summary

A controlled environment for capturing lung sound signals is not practical. The signals often contain interference such as ambient noise, leading to inaccurate lung health assessments. Hence, denoising is critical. Artefacts may be introduced when an unsuitable denoising filter

is applied, particularly in the lung sound signals domain. Thus, a novel denoising wavelet-based approach by unifying the WATV filter and empirical Wiener filter denoising noisy lung sound signals was proposed in this chapter. In contrast to parameter approximation akin to the literature, optimal filter parameters through case studies were established. Furthermore, the analysis from the case studies provided a new understanding of filter parameters affecting the overall filter denoising performance, particularly in the SNR domain. Subsequently, optimal RMSE performance is accomplished regardless of noise variance and verified in the simulation and experiment studies, ensuring the filter conserves waveform characteristics while denoising lung sound signals. Additionally, SNR improvement by about 12.69 ± 5.05 dB and 16.92 ± 8.51 dB was fulfilled and validated via simulation and experiment studies, respectively, compared with other accepted lung sound signals denoising filters in the literature. The research has demonstrated optimal denoising of noisy lung sound signals and further smoothing of the denoised signal achieving optimal RMSE results and improved SNR.

The thesis focused on denoising simulated and experimentally environmental noises, but did not consider separating heart and lung sounds. The signal quality estimation method aimed to quantify noise reduction but relied on assumptions by subtracting the denoised signal from the noisy signal to estimate noise. This may explain differences in SNR results between the simulation and experiment studies. Although the proposed denoising filter does not directly consider the heart sound signal interference, the integration of WATV and Wiener filter produces denoised signals without distortion. Overall, the limitations centre on the inability to fully separate heart and lung sounds for reference signals and the reliance on assumptions in the noise estimation method.

Chapter 5   An Acoustic System of Sound Acquisition and Image Generation for Frequent and Reliable Lung Function Assessment

Chapter 5 depicts the instrumentation aspects of a medical assessment tool developed in this research that measures changes in the distribution of lung sounds through acoustic imaging. Although there have been experimental studies on the identification of the nidus, these researches [11, 93] concentrated on acoustic sound detection rather than acoustic imaging and did not take into account the impact of sensor sensitivity or sensor number [8, 11, 93]. Additionally, in order to support: 1) The respiratory system modelling, acoustic imaging, and sensor array design with regards to locating nidus in Chapter 3; and 2) The performance of the denoising filter in Chapter 4, an experimental investigation on locating nidus using an acoustic imaging system transmuted from lung sounds with the addition of a denoising algorithm was designed and built to precisely identify the location of the pathology produced by the airways for enabling smart therapy.

Chapter 5 is reproduced[**][††] from [5, 10], where the thesis author is the main author of the paper. Chapter 5 is organised as follows. The overview and a focused acoustic imaging systems review on lung function assessment are described in Section 5.1 and Section 5.2, respectively. The hardware data acquisition and the design setup are presented in Section 5.3. The performance index and setup of the proposed system signal acquisition in relation to noise, and the accuracy of acoustic imaging are presented in Section 5.4. The experimental results and discussions are presented in Section 5.5. The summary is presented in Section 5.6.

5.1 Overview

Chest X-rays or CT are used usually during periodical medical visits to check the patient's lung function. As a result, adapting medical therapy to each patient's unique medical

---

[**] © 2023 IEEE. Reprinted, with permission, from [10] C. S. Lee, M. Li, Y. Lou, and R. Dahiya, "Design of a robust lung sound acquisition system for reliable acoustic lung imaging," presented at 2023 IEEE International Ultrasonics Symposium, Montreal, Quebec, Canada, Sep 03, 2023.

[††] Under IEEE Sensors consideration [5] C. S. Lee, M. Li, Y. Lou, Q. H. Abbasi, and M. A. Imran, "An acoustic system of sound acquisition and imaging generation for frequent and reliable lung function assessment," submitted to IEEE Sensors Journal, June 02, 2023.

progression is challenging. The therapy result may be strengthened by frequent or continuous observation of lung functions throughout the patient's everyday tasks [17, 18].

An uncomplicated technique for frequent lung function assessment is acoustic imaging. Acoustic imaging may enhance healthcare delivery to patients with lung diseases, resulting in early detection of the condition worsening, adjusting to the therapy and achieving a higher quality of life, and decreased hospitalisation rates [19, 20]. Thus, a need has arisen for portable devices with acceptable accuracy, cost, and simple setup to monitor essential parameters such as locating airway obstructions (nidus) and tidal volume changes over time.

Acoustic imaging systems such as VRI [22, 24, 36] employ an array of digital stethoscopes alike, recording the respiratory signals and converting the multiple signals from the array of digital stethoscopes to acoustic images for lung function assessment. The visual representation enhances clinical relevance by providing localised data on breath sounds between various lung locations [22, 24, 36]. Although there is a positive quantitative data link between VRI and lung problems, such as smoking index and the build-up of excess fluid between layers of the pleura outside the lungs [22, 24, 36], there is no positive data correlation in locating obstructed airways (nidus) between VRI and airway-related diseases, such as asthma and COPD [22]. Hence, biometric sensors, such as digital stethoscopes used for capturing lung sound and later converting to acoustic images for lung function assessment, still need to be developed significantly [29]. Additionally, studies in [29] and [116] find no accurate, non-invasive, affordable, or simple-to-use biometric sensor to measure changes in the airways. An accurate data representative, such as acoustic lung signals and images of the patient's lung function, is vital in this study. Therefore, designing a portable, low-cost, and efficient lung sound acquisition platform is needed for reliable lung function assessment via acoustic lung imaging.

Chapter 5 proposed a wearable acoustic lung imaging system translated from reliable lung signals. To the author's best knowledge, the proposed system, presented in Figure 5.1, comprising of various sensing and functional components, including an onboard computer and an array of daisy-chained MEMS microphones (see Figure 5.1(b)) packaged into a standalone or wearable mobile device for the assessment of lung function via acoustic imaging translated from lung sounds captured from the array of MEMS microphones have not been investigated. The suggested system is straightforward to operate, and no specialised training is required to interpret the assessment results. A denoising algorithm [2] specifically created to enhance captured lung sounds by actively suppressing unwanted interfering noise

from the environment, including noises with a spectral signature that coincide with the body sounds, is integrated into the proposed system (see Figure 5.1(c)) and has outperformed commercial digital stethoscopes, such as Thinklabs One [38] and Littmann 3200 [37], in terms of RMSE and SNR by 0.15 and 8 dB, respectively. Thinklabs One [38] and Littmann 3200 [37] were selected as a benchmark in this study due to their filtering capabilities and improved ability to acquire acoustic signals. The SNR describes the signal quality and strength with respect to the environment noise while maintaining the lung signal frequency of interest, while RMSE findings show the system's ability to retain critical characteristics of lung sound post-signal processing. RMSE is unitless as normalised digital amplitude was utilised in the computation. Compared to the commercial digital stethoscopes, the loss ratio for the proposed system is around 5 dB compared to about 10 dB in terms of the sensor area sensing sensitivity power spectral mapping, so the quality of signals collected is less sensitive by the position of the sensor on the chest area. In terms of sensor-detecting sensitivity mapping, the microphone array maximises measurement sensitivity and uniformity.

An experimental study on identifying airway blockage via imaging was carried out using the proposed system, and the results were supported and correlated by the sensor distribution and acoustic imaging resolution findings in Chapter 3. Waterbags with various diameter sizes between 50 mm and 80 mm were placed on the posterior of a healthy volunteer to mimic the airway obstruction, akin to the literature [30, 31, 153], to illustrate the effect of presenting accurately obstructed lung images from captured lung sounds. Multichannel respiratory signals were captured with the proposed system, equipped with an array of MEMS microphones with the array design recommendation from [8, 9], and the imaging output translated from lung signals from the proposed system and commercial digital stethoscopes were analysed [8, 9]. The proposed system is about 10% more accurate in detecting airway obstruction as compared to commercial digital stethoscopes through acoustic imaging translated from captured lung signal. Hence, capturing accurate acoustic signals is critical in determining lung function. Furthermore, the identified airway obstruction with the proposed system correlates closely (92%) to the modelling and simulation design work in [8] and [9]. The proposed acoustic imaging system can be used for various potential purposes, including home-based screening for respiratory disorders by clinicians located elsewhere than the patients, gating controls for radiological imaging procedures, and reducing infection concerns associated with intra-hospital patient transportation to the equipment and lower machine operating expenses [19, 20, 52, 154].
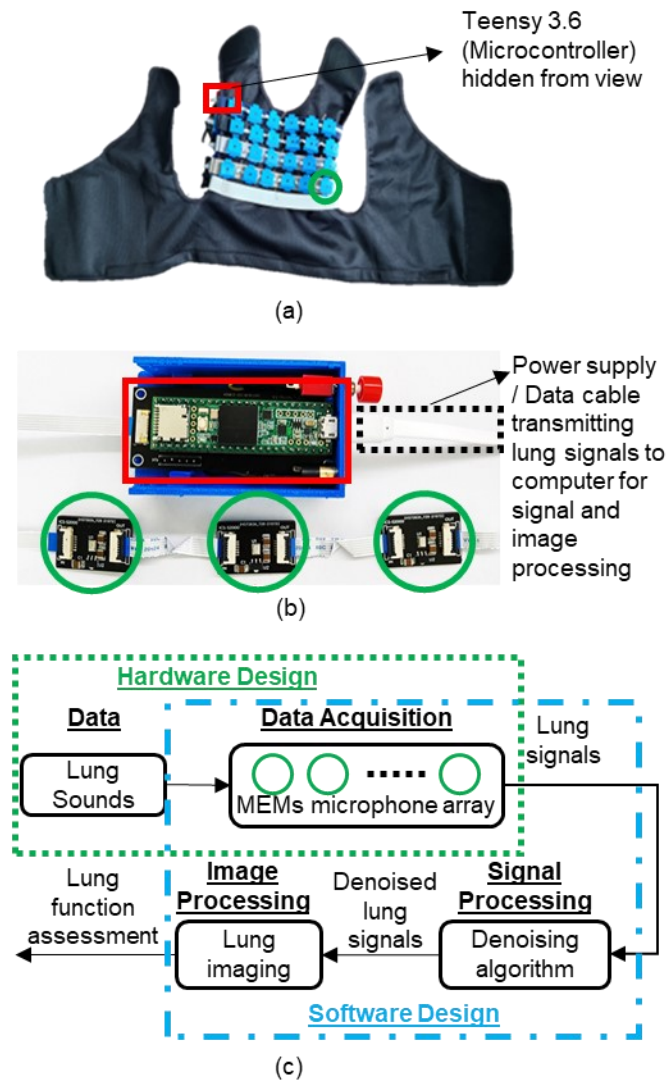
Figure 5.1   The overview of the proposed acoustic imaging system for self-assessment of lung function. (a) An array of wearable MEMS sensors denoted as ○ for simultaneous acoustic lung signal acquisition interconnected with flexible printed circuit cable. (b) Sub-system data acquisition and control unit consisting of a microcontroller and daisy-chained multimicrophone array (without cover). (c) The data flow and the acoustic imaging sub-system.

Chapter 5 is organised as follows: A concise literature review on lung function assessment is described in Section 5.2. The hardware data acquisition and the design setup are presented in Section 5.3. The system and its sub-system performance such as signal acquisition in relation to noise, and the accuracy of acoustic imaging are presented in Section 5.4. The experimental results and discussion are presented in Section 5.5. Lastly, Section 5.6 presents the summary.

5.2 Acoustic Imaging Systems Review

Although chest X-rays and CT are dubbed as the gold standard technique for lung function assessment due to their accuracy and reliability method, it is time-consuming, expensive (> USD 5000) and complicated to operate, and can only be performed in medical settings (patient-to-equipment approach) [29]. Moreover, chest X-rays and CT require medically trained personnel to interpret the assessment results and expose patients to harmful radiation, making frequent lung function assessments impractical.

Acoustic imaging through analysis of the captured acoustic signal from an array of sensors at multiple locations is an alternative for lung function assessment and has an equipment-to-patient approach, particularly for cases where the patient's movement is restricted or discouraged due to disabilities, pandemic, or inaccessibility to facilities rendering traditional techniques unfavourable. Acoustic signals and imaging providing intuitive assessment results have been proposed as a potential means for frequent monitoring and early assessment of lung function [21, 29, 30, 35, 36, 153]. Chapter 3 demonstrated the capability of acoustic signals and imaging for detecting and locating airway obstruction via remodelling and simulation. The lung disorders' location and severity can be identified via acoustic imaging transmuted from the captured lung sounds via an array of digital sensors at different locations [8, 21, 24, 29, 30, 35, 153]. Capturing robust acoustic signals produced from the patient's chest wall is a critical requirement for assessing lung function via acoustic imaging.

In the quantitative forms of acoustic signal representation, VRI employs an array of digital stethoscopes alike, records the vibration energy generated during breathing, and converts the breath sounds to an image for lung function assessment [22, 24, 36]. Digital stethoscopes such as the Thinklabs One [38] and Littmann 3200 [37] are a few examples developed with filtering capability for computerised analysis and signal quality enhancement to eliminate subjectivity in interpreting results, unpredictability, and inconsistency between listeners and susceptibility to airborne ambient noise. However, these systems are still susceptible to dynamic noise in most real-world settings [116] and are expensive (> USD 300) [37, 38] as a single unit. Background conversation and other environmental disturbances are frequent in many settings, and patient movement taints the sound signal captured by the stethoscope. The denoising function becomes critical in lung-sound signal processing, as the captured lung sounds can affect the acoustic imaging assessment. An additional vacuum seal is required for the VRI digital stethoscopes sensor alike to achieve proper contact with the

patient's body, making the device interfering and impractical to integrate with other body sensor networks or respiratory therapy devices for frequent home-based monitoring. Furthermore, remote monitoring or home-based assessment through digital stethoscopes requires advanced patient compliance and position accuracy.

5.3 System Design

Figure 5.2 depicts the workflow for the system's acquisition of acoustic signals through an array of MEMS microphones and ends with acoustic lung images converted from lung sounds. Compactness, dependability, and usability were the three design priorities for the hardware. The proposed distinctive programmable system illustrated in Figure 5.2's block diagram consists of an array of MEM microphones and was designed to address two known limitations with digital stethoscopes: 1) robustness in noisy environments; and 2) accurate acoustic imaging representation. The MEMS microphone module captures the acoustic signals originating from the air hitting the airway wall (airflow) and converts the airflow to acoustic (electrical) signals, which can then be communicated to the microcontroller as digital data. Section 5.3.1 and Section 5.3.2, respectively, each describes the hardware and software system design.
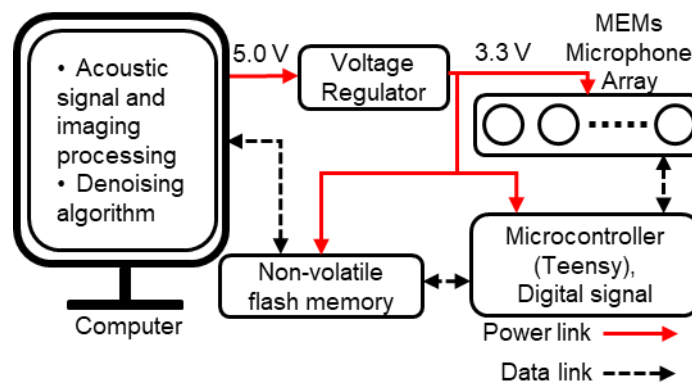
Figure 5.2   **The overview block diagram of the system setup.**

5.3.1 Hardware Design

The following sub-sections discuss the hardware components utilised for the proposed system, the data acquisition module, and the design of the acoustic sensor array, as shown in Figure 5.1(c).

5.3.1.1 Hardware Components

A digital time-division multiplexing (TDM) and daisy chained enabled ICS-52000 (TDK, USA) [155] output bottom port microphone was utilised in the proposed system design to capture lung sound. The ICS-52000 is soldered onto a printed circuit board (PCB) with a voltage regulator and capacitors (see Figure 5.3), as the manufacturer recommends. The ICS-52000 features a broad frequency response from 50 Hz to 20 kHz, covering the typical lung sound frequency range [30, 123, 153, 156]. Digital TDM microphone was selected as the 24-bit industry-standard TDM interface enables an array of up to 16 ICS-52000 microphones to be daisy chained to a single digital signal processor, and without the use of an audio codec in the system — reducing the number of physical components and computation power. The MEMS microphone's characteristics were selected so that its lung signal acquisition capabilities are comparable to those of a commercial digital stethoscope [29, 35, 37, 38, 84, 153].
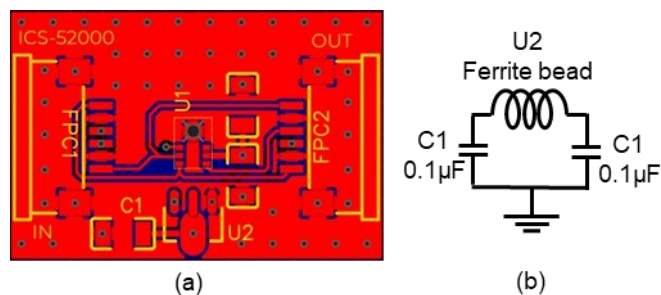
Figure 5.3 **(a) PCB design for ICS-52000 and its electrical components and connections, where U1 represents ICS-52000, and FPC denotes flexible printed circuit cables to transmit the data from U1 to the microcontroller. (b) The voltage regulator connection for ICS-52000 is represented as U2**

Teensy 3.6 (PJRC, USA), a 32-bit, 180 MHz ARM Cortex-M4 core equipped, was selected as the microcontroller for the MEMS microphone due to the compact design that can be easily integrated into a wearable device, and it is an all-inclusive processor configured for a customised solution that offers flexibility in programming, adjusting parameters, and updating algorithms. A digital signal processing solution is chosen in the proposed system design as it is programmable so that the signal processing parameters can be individualised. The Teensy 3.6 board assembly for the system hardware design is presented in Figure 5.4, where Teensy 3.6 is soldered to a PCB for stability that has a voltage regulator converting 5 V to 3.3 V supplied to the MEMS microphones, and a 100 kΩ pulldown resistor at the serial

data (SD) output to discharge the output line during the microphones' three-state logic on the data bus.

5.3.1.2 Data Acquisition System Design

The word select (WS) signal synchronises ICS-52000 microphones, ensuring that acoustic signals recorded from several microphones using the same clock will be sampled simultaneously. A delay to the start of the frame sync WS signal is implanted to the ICS-52000 MEMS microphone sensor by enabling WS output on the clock master by 512 ms after the serial clock (SCK) is activated. The delay allows the internal circuits of the microphone to initialise properly before beginning the synchronization sequence with other microphones in the TDM array. Figure 5.5 demonstrates an example of an array of MEMS microphones connected on a single data bus, in which the slave serial data port's format is TDM.
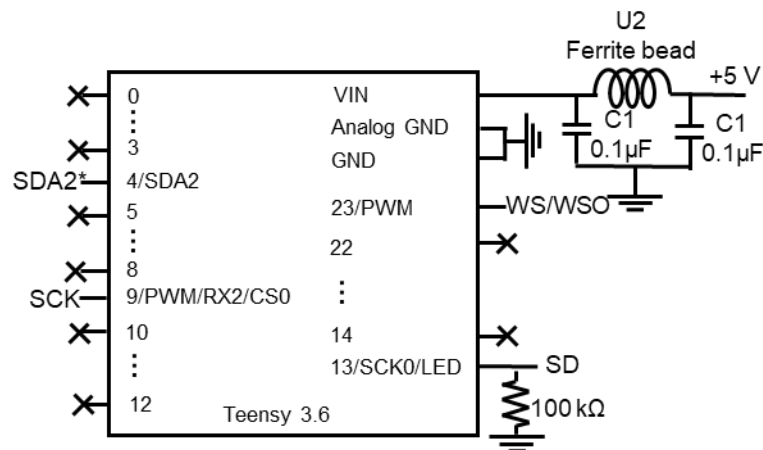
Figure 5.4   Digital pins utilised on Teensy 3.6 board for this study. Digital pin 4 (SDA2) is only required when multiple Teensy 3.6 board is required (see Figure 5.6). For other digital pins usage and details, refer to [157].

The WS clock master from the microcontroller drives the WS signal of the first MEMS microphone. The array of MEMS microphones was daisy-chained, allowing the first MEMS microphone WS output (WSO) to drive the WS of the second MEMS microphone, etc. The first TDM slot will be used to output data from the ICS-52000, the second TDM slot will be used to output data from the next microphone in the chain, etc. The word length output data is 24 bits/channel, and the data word format is the most significant bit first and 2's complement. The frequency of SCK utilised in the proposed system design employing 5–8

MEMS microphones in a chain is given as $256 \times f_{WS}$, where WS frequency (f_{WS}) is about 8000 Hz [155].
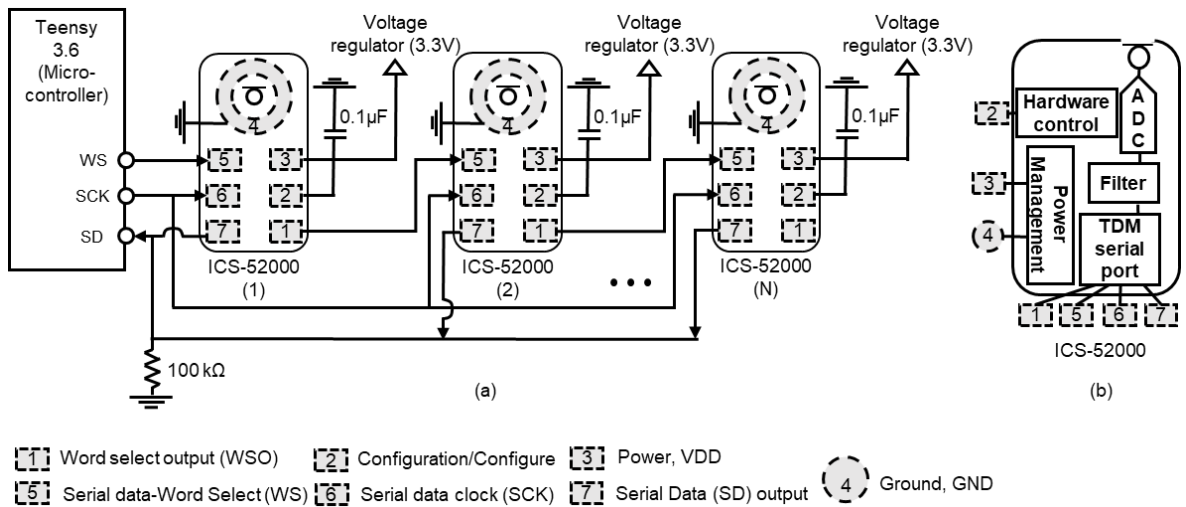
Figure 5.5 **Overview of the connections between daisy-chained MEMS microphone and microcontroller. (a) System block diagram of digital pin connections for an array of MEMS microphones. (b) ICS-52000 digital pin and its modules.**

The design of an array of microphones can assess lung function via acoustic imaging, translated from the multichannel lung sound signals, similar to VRI [21, 35] and Chapter 3. From Figure 5.5, the ICS-52000 package incorporates a MEMS microphone sensor with a sensitivity tolerance of ± 1 dB, allowing high-performance microphone arrays and eliminating the requirement for system calibration; signal conditioning, such as digital filter removing unwanted low-frequency noise from the direct current and synchronised sampling of all microphones in an array of acoustic signals enabling accurate array processing; an analogue-to-digital converter; decimation and anti-aliasing filters; and power management.

5.3.1.3 MEMS Microphone Array Design

The practicality of designing an acoustic imaging system regarding the number of sensors and sensor sensing diameter needed to achieve the desired minimum detectable obstructed airway (nidus length) is shown in Figure 3.10. With more sensors, the detectable minimal nidus length could be resolved more precisely due to the larger overlap of the sensor sensitivity area, e.g., with the same sensing diameter of 50 mm, a detected nidi length of 73 mm requires about 4 sensors and nidi length of 25 mm requires about 24 sensors on one side of the chest.

As up to 16 ICS-52000 can be daisy chained in an array with one microcontroller, Figure 5.6 demonstrates an array of Teensy 3.6 board connections for an acoustic signal acquisition system or acoustic imaging system [21, 24, 30, 31, 35, 36] requiring more than 16 MEMS microphones [8, 9].

The Teensy 3.6 and ICS 52000 MEMS microphones connections are demonstrated in Figure 5.4, Figure 5.5, and Figure 5.6. Flexible printed circuit (FPC) connectors and cables were utilised to connect Teensy 3.6 to the external microphones due to its lightweight interconnection enabling the system wearability, as illustrated in Figure 5.1, and Figure 5.3. The standard USB type A-USB micro interface was utilised to transfer MEMS microphones data to the memory card 115,200 bit/s baud rate and then to the computer for digital acoustic signal analysis. Arduino sketchbook v1.8.13 was used as the programming software activating Teensy 3.6 microcontroller in acquiring acoustic signals through the array of MEMs microphones. Real-time computerised lung sound analysis, adjustments to digital signal processing, and usability improvements can all be implemented on the same hardware platform owing to the flexibility of the programmability.

(Master)   (Salves)   • • •   (Salves)
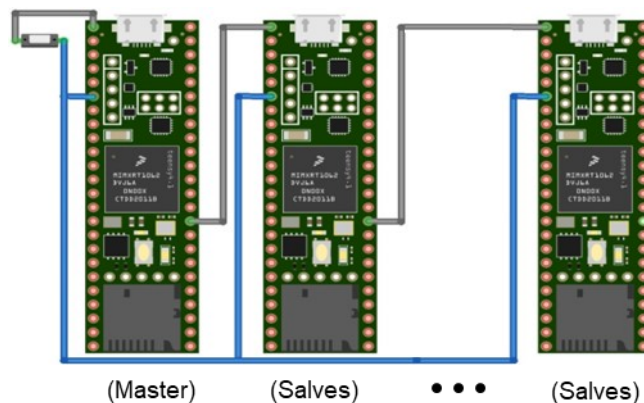
Figure 5.6   Teensy 3.6 boards connection for multiple arrays of a maximum of 16 MEMS microphones each, with the first Teensy 3.6 board as a control (master) with a master switch, and the subsequent Teensy 3.6 boards as salves. Grey represents the ground connection, and blue represents the interconnection of digital pin 4 (SDA2).

5.3.2 Software Design

The following sub-sections illustrate the software data acquisition module, signal processing module and acoustic lung image processing from the acquired lung signal, as presented in Figure 5.1(c).

5.3.2.1 Data Acquisition Software Design

The overall block diagram of software design, including the data acquisition module, is illustrated in Figure 5.7. Through the connected serial port, the microcontroller waits for the computer to send a data transmission command to collect acoustic signals via MEMS microphones. The collected data is then stored in the non-volatile flash memory when the acoustic signals from the MEMS microphones come in. The collected digital data is saved in XLS format with separate columns according to the individual MEMS microphone digital data in an array.
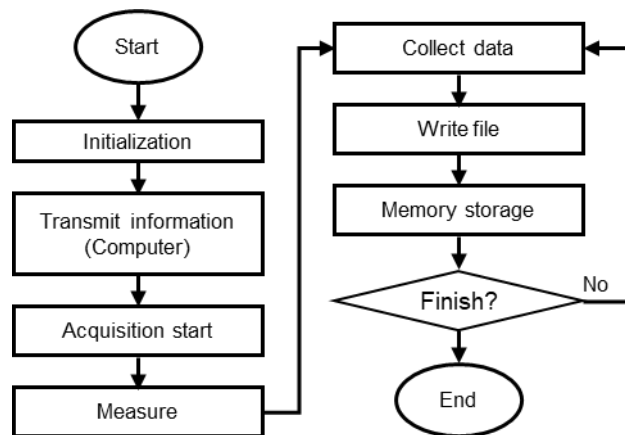
Figure 5.7   Software overall flowchart for the acquisition of acoustic signals.

5.3.2.2 Signal Processing Denoising Method

Figure 5.8 shows the proposed system's input and output flow of the acoustic signal. The input signal sampling frequency F_S of the system is 8000 Hz. From Figure 5.8, an ICS-52000 in-built digital low pass filter [155], and the denoising algorithm from Chapter 4 are applied to suppress the inference, such as ambient- and patient-generated noise to enhance the acquired lung signal through MATLAB 2019b.

Delivering denoised signals from ambient noise while carefully avoiding the cancellation of auscultation patterns that are diagnostic of the disease, such as crackling that can easily pass for noise, is one of the primary concerns of implementing denoising in acoustic lung sound recording systems. The simple addition of an active noise-cancelling filter or typical finite impulse response filter [2, 29, 135] to an acoustic MEMs microphone does not adequately solve these concerns [123]. Hence, a novel denoising method from Chapter 4 [2] is included in the proposed system design, as shown in Figure 5.2 and Figure 5.8. This approach is

optimum at removing external noise while retaining the desired signal. An empirical Wiener filter and a unified wavelet threshold denoising filter (WATV) are combined in the approach. Before attempting to achieve a sufficient denoised signal coefficient from the lung sounds, WATV is first modified to lessen the interference noise. This is accomplished by simultaneously calculating both reliable and unreliable wavelet coefficients. By minimizing the denoised signal overall mean square error by inverse filtering, the estimated signal coefficient is sent into the empirical Wiener filter for smoothing. The algorithm has been validated and given in-depth details before in [2] and has been tested on actual lung sound signals collected from patients with respiratory disorders in a noisy clinical environment.
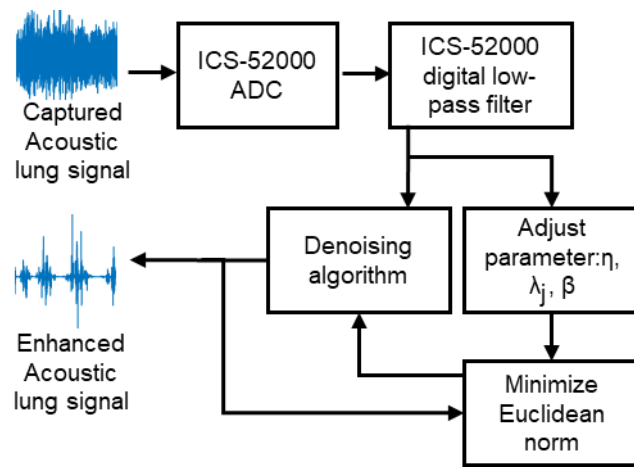
Figure 5.8 **Software flowchart for signal collection and integrated post-processing denoising.**

5.3.2.3 Image Processing

Using an image processing approach from Section 3.3.3 Acoustic Image Generation (3.15) [8, 9, 21], the acquired lung signals are then transformed into acoustic images for analysis in MATLAB 2019b. The lung signal intensity $\bar{P}$ at each sensor location i in a x- and y-axis coordinate plane is computed by accumulating the acquired signals P over a known time t interval from t_1 to t_k. The acoustic lung imaging Q projected from lung signals comprises of acoustic signal $\bar{P}(x, y, t_1, t_k)$ and interpolation function $h(x, y)$. Hermite interpolation polynomial is applied to estimate sound intensity outside of the sensor position on the chest area, as the high spatial resolution is required for the limited number of sensors that can be placed onto the chest wall [31]. The highest, lowest, and in-between values are determined as maroon, white, and grey. Each acoustic signal is normalised, and acoustic images are then displayed as the output collected from the intensity (amplitude) of the sound signal.

5.4 System Performance Evaluation

In terms of acquiring robust and accurate lung signals, the proposed system's lung signal acquisition unit is compared with commercially available digital stethoscopes, Littmann 3200, and Thinklabs One, which are integrated with cutting-edge denoising technologies to precisely measure the system design standards [37, 38]. Littmann 3200 and Thinklabs One digital stethoscopes were selected due to their unique design and setting that impact the transmitted sound's characteristics and improve acoustic signal collection performance [37, 38]. The homogeneity of the transducing mechanism, quality preservation of transmitted lung sounds, and robustness to unwanted ambient noise are three critical factors in measuring the system's performance. Hence, RMSE, SNR, and sensing sensitivity are crucial performance indicators for measuring how well sensors capture accurate lung sound signals in relation to noise.

A concise experimental verification was performed to identify airway obstruction and the findings in Chapter 3 airway remodelling and simulation studies. All system performance analyses and results were performed in MATLAB 2019b. The lung sound acquisition and imaging setup are described in Section 5.4.1. Section 5.4.2 covers the performance index of the sub-system data acquisition, such as the sensor sensing sensitivity, acquired signals quality, and identification of nidi through imaging translated from the acquired lung signals.

5.4.1 Acoustic Signals and Nidi Imaging Acquisition

The following subsections describe the simulation and experimental setup for acquiring acoustic lung signals and lung imaging in this study.

5.4.1.1 Acoustic Signals Acquisition

A lung sound signals simulator is preferable for repeatability when multiple devices and systems are required to evaluate the acquired signal in regard to noise performance [123]. A consistent comparison between multiple devices can be obtained when various variables in the actual signals recording, such as the patient's internal body movement sound and ambient noise profiles in the real world, are repeatable. Hence, 10 unhealthy lung sound signals with crackles and wheezing from patients diagnosed with asthma, or COPD, and 10 healthy lung signals of 15 seconds duration, recorded from the posterior of patients' chest, were selected from a respiratory database [104]. Then, each lung sound signal was independently played

via a customised lung sound simulator at an output level similar to that of actual auscultation [116].

The customised lung sound simulator (see Figure 5.9) utilised a 15 mm thick silicone material (Baoblaze, USA) that closely resembled a human's skin, fat, and muscle layers and was placed on the top of a S1 Pro portable Bluetooth speaker system (BOSE, USA). The S1 Pro portable Bluetooth speaker system resembles a typical adult chest wall in terms of its overall size and has a frequency response within the acoustic frequencies of interest ranging from 62 Hz to 17 kHz. To simulate actual recording, the signal acquisition is carried out in a setting with an average sound pressure level of 59 ± 0.54 dBA, which is comparable to a typical noisy clinical environment [150]. To maintain a consistent ambient noise power during each device assessment, the environmental noise was monitored using an omnidirectional sensitive and high SNR MP34DT04 MEMs microphone (STMicroelectronics, Switzerland). The setup allows the author to test the suggested system directly against several other digital stethoscopes in a wide range of lung sound and background noise combinations.

Figure 5.9   **Lung sound simulator for consistent and repeatable lung signal output.**

The filtering and denoising capabilities of individual digital stethoscopes were considered to achieve reasonable signal acquisition performance comparison. Littmann 3200 digital stethoscope filter option was set to "Extended mode," which amplifies sounds from 20–2000 Hz per the suggested setting by the manufacturer [37]. The filtered lung sound signals are saved digitally in accompanying computer software. Thinklabs One digital stethoscope filter option was set to "Filter setting 3–4," recommended for lung sound signals, and the digital

lung sound signals are transmitted to the accompanying digital device for analysis. All digital acoustic signals recording were resampled to 8000 Hz to standardise signals analysis.

5.4.1.2 Acoustic Imaging Generation

Various diameters of waterbag were positioned on the lung sound simulator right middle, as illustrated in Figure 5.10, to emulate the obstructed area in the airway [30, 153, 158] and to compare the nidus detection capability of the proposed system and the two digital stethoscope through imaging translated from the captured lung signals. For repeatability and consistency in the acoustic imaging acquisition, the customised lung sound simulator played healthy lung sound from the respiratory database [104] and used a waterbag for airway obstruction as there are various recording locations from the respiratory database [104], such as the trachea, lateral, and anterior, and the exact unhealthy or obstructed lung sound position is unknown. The experiment is then repeated on a healthy volunteer with a waterbag attached to the posterior combined with the acoustic sensor design findings in Chapter 3 [8, 9] to locate the nidi length via imaging.
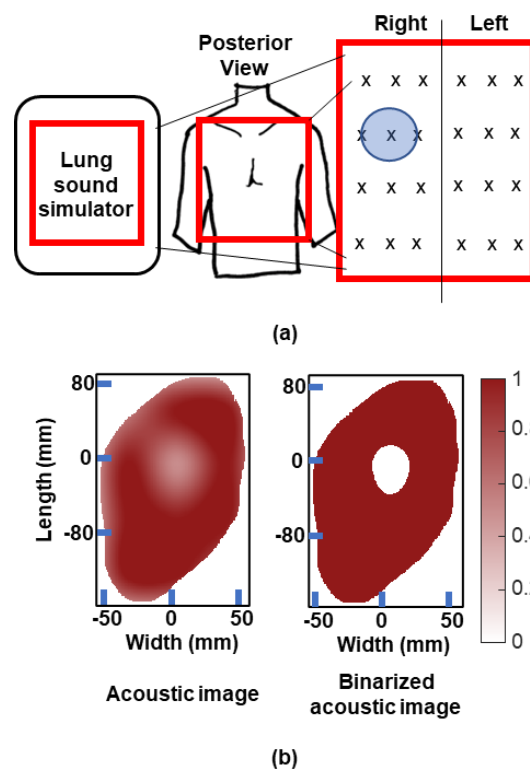
Figure 5.10 **The experimental and acquisition of acoustic imaging setup. (a) The schematic diagram of the experimental setup for capturing lung sound signals and nidus detection in the airways with waterbags. x denotes the positions of the acoustic sensors, such as MEMS and digital stethoscopes. The circular block presents an obstruction in the airways. (b) Binarised acoustic imaging with Hermite interpolation function for experimental results analysis.**

Sensors were placed on the lung sound simulator without overlapping and with equal spacing as shown in Figure 5.10(a). Acoustic imaging was generated [8, 9] with the recording of lung sounds from the proposed system, and the two digital stethoscopes without the waterbag were used as healthy reference images. As 3M Littmann and Thinklabs One can only provide a single data point, the breathing phase was used to synchronise [156, 159] and form an array of lung sound signals and converts the lung sound signals into acoustic imaging (see Figure 5.11), similar to the typical acoustic imaging system [21, 30, 35].
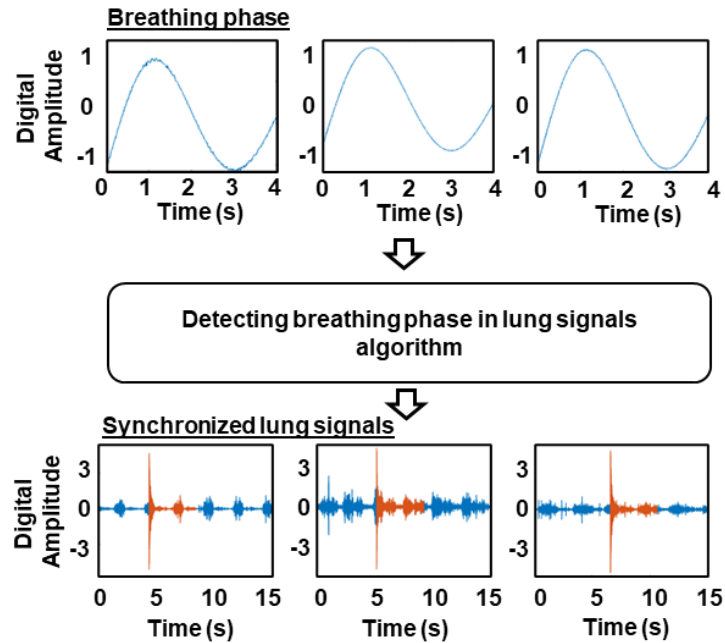
Figure 5.11   Synchronising of an array of lung signals captured at different time via breathing phase. Blue denotes the asynchronous lung signals captured due to single-point data. Red represents the synchronised lung signals via the breathing phase.

5.4.2 Sensing Sensitivity, Signal Acquisition, and Identification of Nidi Performance Index

The following subsection presents the performance metrics for sensor sensing sensitivity, acquired signal quality, and identifying nidi length through imaging translated from the acquired lung signals.

5.4.2.1 Sensing Sensitivity Performance Index

The devices and system signal pickup surface's sensitivity can be assessed by the sensor sensing sensitivity area. Figure 5.12 depicts the setup for the sensitivity area measurement. In order to evaluate the sensitivity sensing area, the proposed system and the commercial

digital stethoscopes were mounted directly on top of a 20 mm thick sound absorbing sheet (-25 dBA) with alternating 3-by-3 array of 6 mm hole diameter, similar to the sensor sensitivity study in [116].
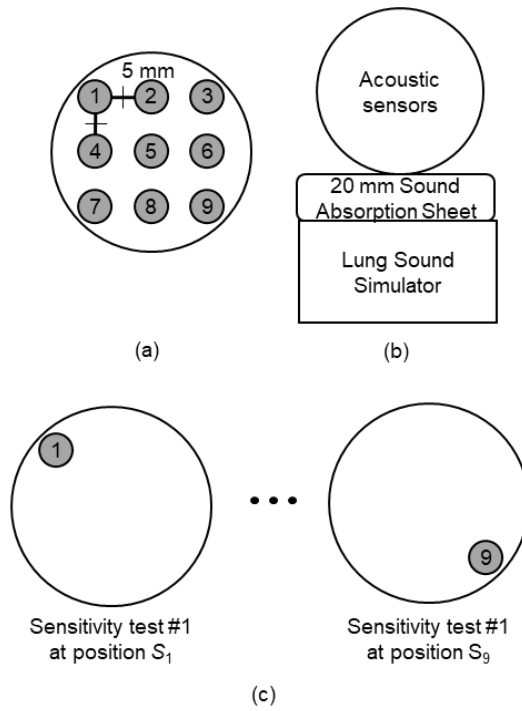
Figure 5.12 **The surface sensitivity performance setup with a single position capturing of acoustic signals at each interval, S_1, S_2, …, S_9. (a) Overview of sound absorption sheet with alternating 3-by-3 array. (b) The sensor sensing sensitivity test setup. (c) Example of alternating the sensitivity test.**

Throughout the course of the sensor sensing sensitivity assessment, output signals $y_{iu}(n)$ are recorded for each position $i = [1, …, 9]$ and white noise $x_w(n)$ with a constant power is consecutively played from each hole diameter of the position shown in Figure 5.12 for $u = [1,.., 10]$ test.

The spectrum power of each output signal $y_{iu}(n)$ was calculated for frequencies between 100 Hz and 2000 Hz – the typical respiratory frequencies range, and the majority of the relevant lung sound signals are concentrated [116, 156]. The spectrum power from each output signal was compared to the centre output signal $y_{5u}(n)$ position. The average spectrum power for each position i is determined as,

$$\overline{S}_i = \frac{\left(\sum_{u=1}^{10} S_{iu}\right)}{10} \qquad \qquad (5.1)$$

where the spectral power of the recorded signals $S_{iu}(n)$ is averaged across all u tests. The logarithmic ratio $S = 10\log(\overline{S}_i/S_5)$ is then used to compare the average power from the intermediate point $\overline{S}_5$ to each $\overline{S}_i$. The logarithmic ratio shows the effect of the position of input signals on the acquired signal [116].

5.4.2.2 Signal Acquisition Performance Index

RMSE and SNR were utilised as quantitative performance indices for indicating signal precision and noise robustness. RMSE is determined by employing the normalised digital amplitude of denoised signal, the normalised digital amplitude of actual signal, and expressing the signals differences in root mean squared sense as shown in (4.23) and (4.24), where the result closer to 0 indicates the better performing the device is. SNR performance index can be expressed as (4.27) by finding the ratio and expressing the ratio using a logarithmic decibel scale between the normalised digital amplitude of captured signal and the normalised digital amplitude of noise, where a larger value indicates better signal strength acquired in relation to noise.

5.4.2.3 Acoustic Imaging Performance Index

The identification of nidi through imaging transmuted from acquired lung signals using Section 3.3.3 Acoustic Image Generation (3.15) is compared across the proposed system and the digital stethoscopes, where smaller differences in identified nidi when compared to the nidi true area indicate better accuracy. Through local first-order image statistics [112] around each pixel, the resulting unhealthy acoustic image area with airway blockage is converted into a binary image with a locally adaptive image threshold as 0s and all other values to 1s, as shown in Figure 5.10. Healthy high-intensity data areas are represented by 1s, whereas 0s represent obstructed low-intensity data areas in the binary image. The blockage (missing pixels) in the airway can be found by comparing the pixels between the healthy and unhealthy acoustic imaging areas. The nidus length [112] can then be calculated using the missing pixel's area using Section 3.5 (3.18).

5.5 Results and Discussion

The sub-system performance, e.g., the acquired signal quality and the sensor sensing sensitivity between the proposed system data acquisition and digital stethoscopes, are presented in Section 5.5.1 and Section 5.5.2, respectively. The identification of nidi through translating the acquired signals into imaging is shown in Section 5.5.3.

5.5.1 Signal Accuracy and Noise Robustness

Figure 5.13 displays the estimated SNR values (averaged across all trials, lung sounds, and noise signals) for each evaluated digital stethoscope along with the proposed system. Lower SNR values indicate deteriorated signal quality and substantial noise contamination. Conversely, higher SNR suggests low noise contamination and increased signal accuracy with the reference signal.

From Figure 5.13, all three devices presented noise robustness in terms of the SNR of the input signal, similar to the trend in [116], particularly for digital stethoscopes, Littmann 3200, and Thinklabs One. The two digital stethoscopes and the proposed system feature advanced filtering to reduce interference, such as ambient noise and body movement from the lung sound signals [2, 37, 38]. An estimated SNR of about 25 dB, 18 dB, and 17 dB was attained from the proposed system, Littmann 3200 and Thinklabs One, regardless of the low- or high-SNR of input signals as presented in Figure 5.13. Based on the overall measured SNR in Figure 5.13, the proposed system exceeds the competition in terms of SNR in a noisy environment, due to the flexibility in implementing and optimizing the denoising algorithm [2] into the system architecture.

The mean RMSE results of the proposed system and the digital stethoscopes are presented in Figure 5.14. RMSE measures the sensor's ability to acquire accurate signals and maintain major aspects of lung sound. Low values of the RMSE result indicate a low difference in signals captured and desired signals, whereas high values of the RMSE result show a certain level of error in the acquired signal. Overly suppressed filtered signal through the unoptimised and generic filter may result in high SNR, despite the filter introducing obvious distortions resulting in high RMSE results [2]. Hence, a balance between noise suppression (SNR) and signal accuracy (RMSE) is crucial for a lung sound acquisition system.
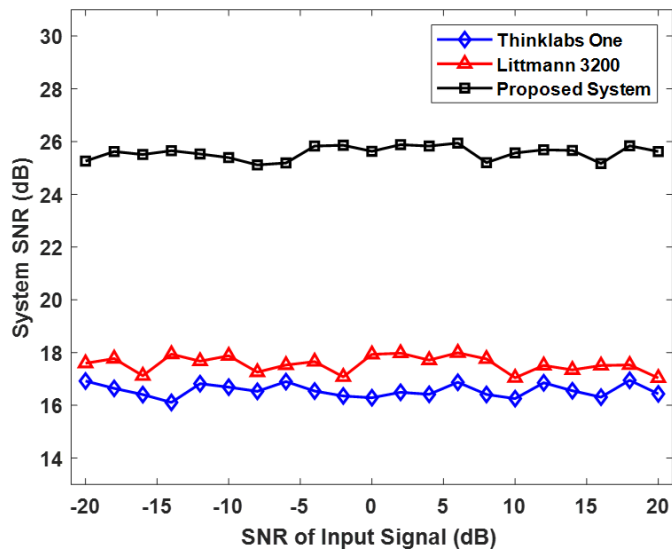
Figure 5.13 The mean SNR performance between various sensors capturing lung sound signals in a noisy environment.

In contrast to the two digital stethoscopes, the proposed system can precisely capture the intended signal in terms of RMSE in a noisy environment, as shown in Figure 5.14. The proposed system achieved better RMSE results by around 0.15 compared to the digital stethoscopes with the implementation of the optimised denoising algorithm in [2]. The proposed system showed a high level of noise reduction while retaining the desired characteristics of the signal of interest, as demonstrated in Figure 5.13 and Figure 5.14.
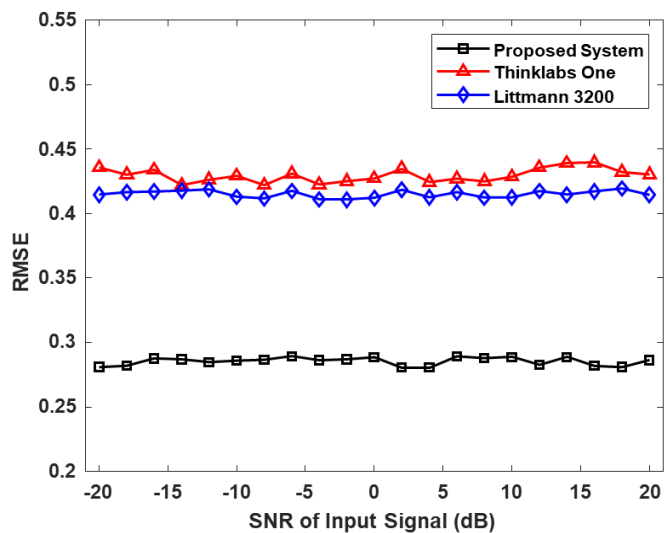
Figure 5.14 The mean RMSE result between various sensors capturing lung sound signals in a noisy environment.

With the addition of a denoising algorithm from Chapter 4, as illustrated in Figure 5.13 and Figure 5.14, the proposed system has proven to be robust to noise and has captured more precise and desirable lung sound signals in terms of SNR and RMSE findings, respectively.

5.5.2 Sensor Sensitivity

From Figure 5.15, the proposed system surface sensitivity area was compared to the two commercial digital stethoscopes and illustrated output spectral power as a function of the sound signal location in decibels with respect to the sensor's centre position.

Digital stethoscopes lose their dynamic range substantially as the lung sound signals move outward, with a loss of about 10 dB, and are most sensitive at the centre of the stethoscope head, possibly due to the sensor sensing design [37, 38, 116]. The proposed system demonstrated a uniform sensing sensitivity across the sensing surface in terms of positional output spectral power to acquire lung sound.

Despite having a lower overall surface size than the two digital stethoscopes, the proposed system have a more uniform sensing sensitivity area of about >20 mm compared to the digital stethoscopes, which have uniform sensing areas of <10 mm. The proposed system provides a more uniform surface sensitivity in recording lung sound signals with a power spectral loss of approximately 5 dB (see Figure 5.15) compared to the power spectral loss of about 10 dB from the two digital stethoscopes. The findings in Figure 5.15 are consistent with the study in [116], especially with regard to positional output spectral trends in digital stethoscopes.
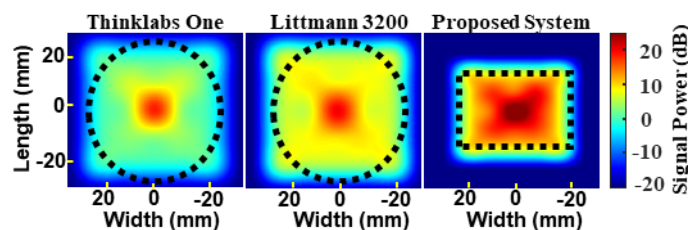
Figure 5.15   Sensing sensitivity (dB) area compared to the power at the centre position of various sensors. Thinklabs One digital stethoscope head (left), Littmann 3200 (centre), and the proposed system (right).

Figure 5.16 further highlights the performance variations in acquiring lung sound signals and the power loss at particular points. From Figure 5.16, position S_9, far from the centre S_5,

was selected to demonstrate the power loss or sensitivity at a specific point on the proposed system and the digital stethoscopes. The proposed system maintains signal power at about 5 dB, relative to the centre and across the frequencies of interest, in contrast to the two digital stethoscopes, which show a significant loss in power (down to 10 dB less) in Figure 5.15 and Figure 5.16. The results of this study on commercial digital stethoscopes support earlier findings that were presented in [116].
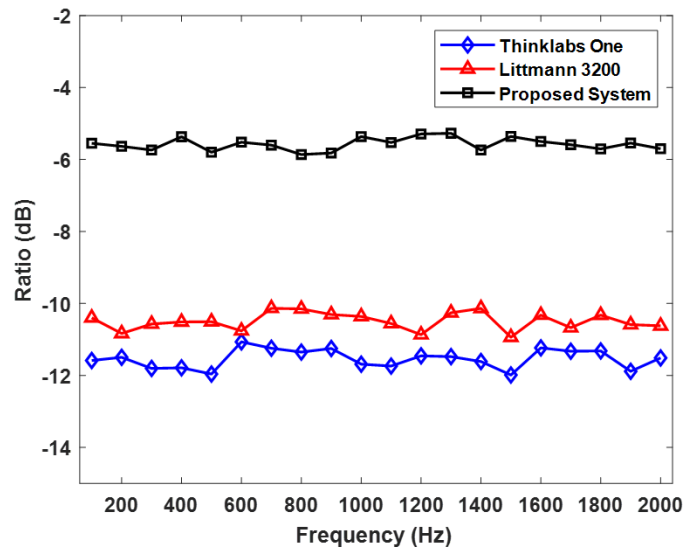
Figure 5.16   The spectrum power ratio between the hardware system and the two digital stethoscopes from position S_9 in relation to the central position S_5, with 0 dB signifying equal signal power made from both positions.

The sensitivity of the proposed system's sensor area makes it such that the exact location of the sensor on the body is not necessary to achieve the maximum amplitude. The other key benefit of the proposed system is that it enables better sound and data gathering for practice by healthcare practitioners with limited training.

5.5.3 Acoustic Imaging

The proposed system and the digital stethoscopes are utilised for experimental study. With the typical adult chest surface area and the proposed sensor design, this study uses 12 and 16 sensor numbers [9] on a healthy volunteer with a waterbag attached to the posterior to record lung sounds. The waterbag's surface diameter of about 46 mm and 65 mm, the minimal detectable nidus length from the modelling study in Chapter 3 [14], was utilised.

Figure 5.17 presented binarised acoustic imaging of obstructed airways translated from the captured lung signals with the proposed system and the commercial digital stethoscopes, simulated with a 50 mm waterbag. The standardised imaging algorithm presented in Section 3.3.3 Acoustic Image Generation (3.15) was applied to the captured signals from the system and the commercial digital stethoscopes, as the commercial digital stethoscopes do not produce imaging as an output. Figure 5.18 demonstrates the accuracy of detecting various obstructed areas via acoustic imaging. Various waterbag diameters, ranging from 50 to 80 mm, simulated the airway's obstructed area [30, 153, 158]. 50 to 80 mm waterbag diameters were selected due to the typical size that can be identified with acoustic imaging systems [9] employing the number of sensors from 12 to 24 [21, 29, 30, 153] and the typical adult lung size limit [117]. From Figure 5.17 and Figure 5.18, the proposed system outperforms the two digital stethoscopes in terms of the detected nidus length through acoustic imaging in Section 3.3.3 Acoustic Image Generation (3.15) translated from lung signals, regardless of the number of sensors deployed. The proposed system achieved 92% accuracy in detecting the actual nidus length. In contrast, the two digital stethoscopes attained from 80 to 85% of accuracy in the detection of actual nidus length, potentially due to the acquired lung sound signals and the robustness to noise as the reliability of lung sound signals translate to the closeness of acoustic imaging [8, 9, 21, 30].
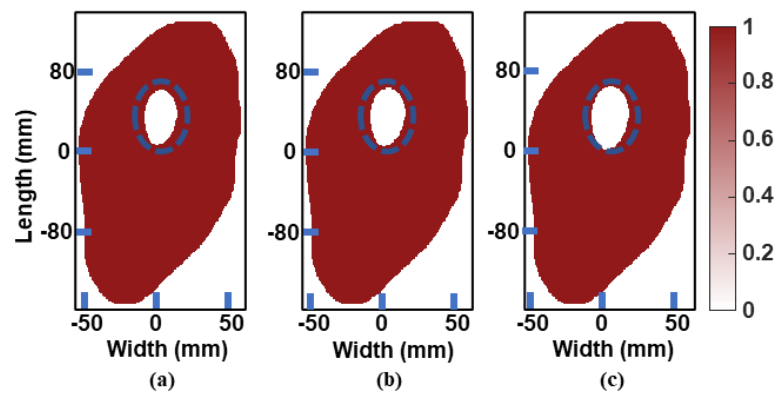
Figure 5.17   Acoustic imaging of obstructed airway translated from acquired lung signals with Hermite interpolation function and with 50 mm nidus length via the waterbag simulation, where the encircled dotted line indicates the actual waterbag size. (a) Thinklabs One, (b) Littmann 3200, and (c) the proposed system.
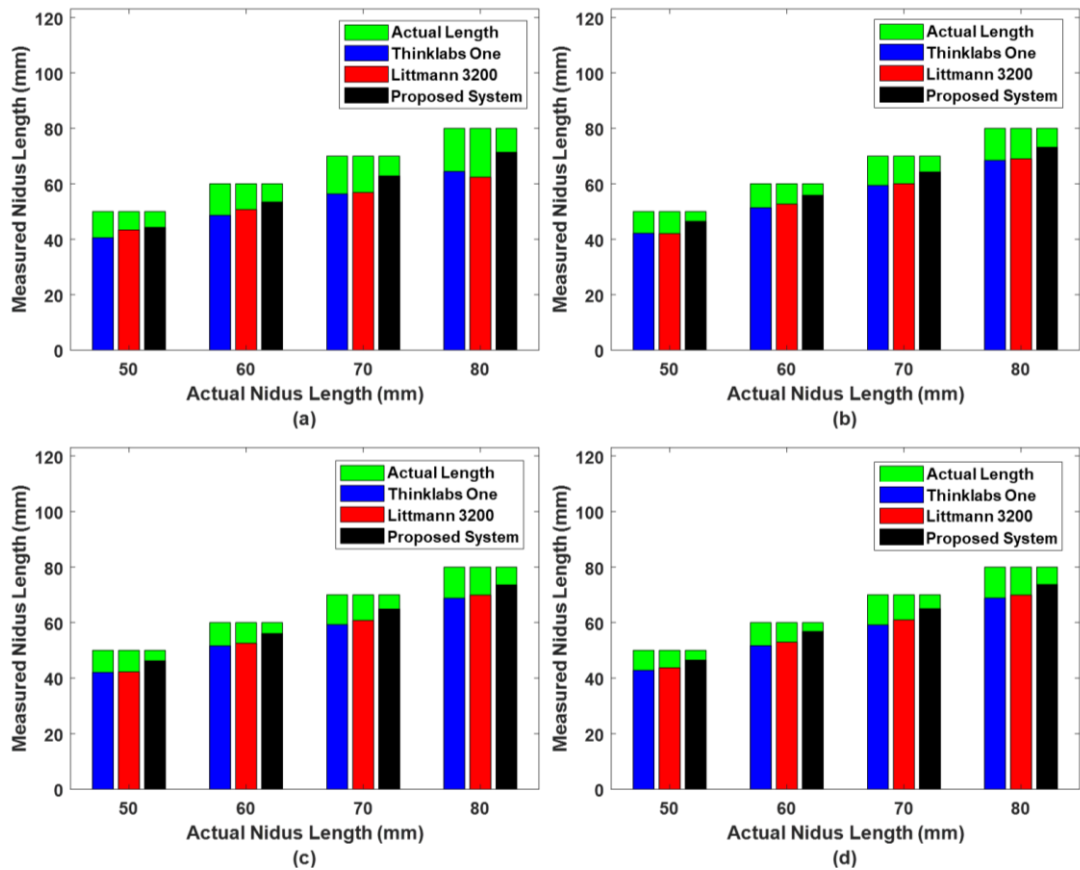
Figure 5.18 **Comparison between the proposed system and digital stethoscopes in detecting nidus through acoustic imaging with (a) 12, (b) 16, (c) 20, and (d) 24 sensors number.**

Figure 5.19 demonstrated the nidus length detected with acoustic imaging on a healthy volunteer posterior with waterbag-simulated airway obstruction. The detected obstructed airway – minimum nidus length, is the shortest (higher resolution) with 16 sensors, whereas the minimum nidus length increases (lower resolution) with the decrease in sensor numbers, showing a similar trend compared to the modelling study in Chapter 3 [9].

The minor discrepancies in the nidus length results in both the proposed system and digital stethoscopes, as presented in Figure 5.18 and Figure 5.19, between this experimental investigation and the modelling study in Chapter 3 [9], may have been due to the airway models and the drawings employed. There are various airway models, including Horsfield, Weibel, and airway models based on animals. However, nidus detection was shown to be possible with acoustic imaging in this work and has corresponded with the modelling studies in Chapter 3 [8, 9]. Moreover, the nidus length is determined by the diameter of the obstructed lung area, which is assumed to be a perfect circle by the results in Figure 5.19.
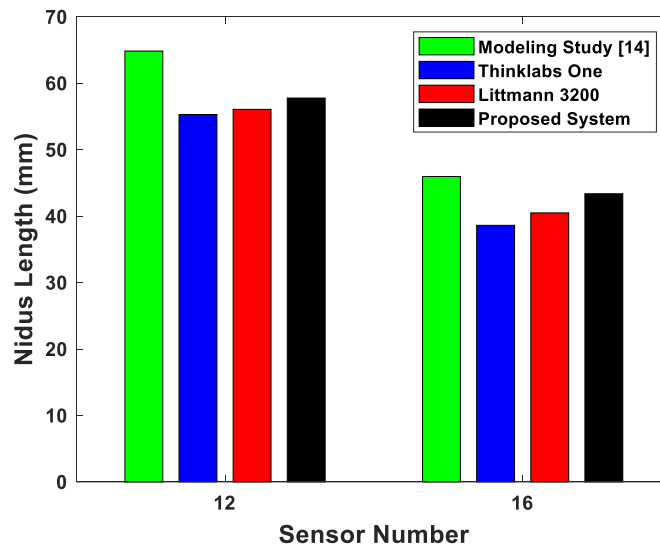
Figure 5.19   The relation between the modelling study in Chapter 3 [9] and experimental validation on the minimal nidus length that can be observed at a fixed number of sensors on one side of the lung.

5.5.4 General Discussion

Although the sensor sensitivity of the proposed system is neutral to the precise placement on the body, the minimum requirement of the array of acoustic sensor design is necessary for a reliable imaging output. The observed nidus length assumes that the sensor position is consistently spaced and covers the posterior region of the chest, much to how clinicians and medical professionals perform auscultation on patients. E.g., detecting an 80 mm nidus length with a single sensor is not possible as a single sensor could not pinpoint the area of obstruction, while using minimally 12 sensors to detect an 80 mm nidus length with the sensor sensing area is possible [8, 9] as the sensor can be uniformly spaced and covers the area of chest posterior with overlapping sensor sensing region.

There will likely be some variation in system performance, and should be taken into consideration due to several variables, such as physical product design, system architecture in terms of software and hardware acquisition, and signal filtering. The independent characteristics of the digital stethoscopes and the proposed system were used to calculate the quality performance outcomes in this study.

The separation of heart sounds from lung sounds was not taken into consideration in this study due to the emphasis on minimizing external interferences, such as environmental noises. The filter option was carefully adapted for the shortlisted digital stethoscopes in this

study, highlighting lung signals' frequency of interest. The shortlisted lung sounds from the respiratory database, and recorded experimental lung sounds were signals from the volunteer's posterior to ensure that the heart sounds would be minimal and would not significantly interfere with the lung sounds.

The various lung sound acquisition systems and the proposed system should not be ranked in absolute terms based solely on signal accuracy and noise robustness. Similarly, the performance attained in this study should not be interpreted as showing how well a healthcare-trained professional can diagnose a patient using the proposed system without extended research. What has been shown and validated in this study is each system's variability in response to acquiring signals with external interference, such as ambient noise, speech, and cough.

5.6 Summary

This work is vital for a system that maps lung sound distribution or acoustic intensity signal into images for an accurate lung function assessment. Chapter 5 develops a wearable, extensible, and robust system of lung sound acquisition and acoustic imaging, which overcomes the limitations of current digital stethoscopes and produces more accurate acoustic images for continual lung function assessment. The proposed system is low-cost, ranging from USD 120 to 280, for a typical 12 to 24 acoustic sensors array [21, 24, 30, 31, 35, 36] recording lung sound simultaneously at different locations, as compared to digital stethoscopes [37, 38] USD 300, with only single data point collection, excluding the cost of the computer for analysis. The objective criteria utilised in Chapter 5 show how well the systems preserve the characteristics of lung sound signals while minimizing external interferences. The proposed system outperforms the digital stethoscopes in terms of RMSE by around 0.15 and SNR by around 8 dB. Additionally, the proposed system has demonstrated a superior sensing sensitivity region regarding the recorded signal power spectrum compared to two well-known digital stethoscopes. The acoustic lung signals were converted into acoustic lung images for experimental investigation and analysis. The nidus detection results via acoustic imaging in the experimental study was validated and supported by the sensor distribution and acoustic imaging resolution modelling studies in Chapter 3 [8, 9].

Although the experimental study interference was comparable to a typical noisy clinical environment, at an average sound pressure level of 59 ± 0.54 dBA, the current experimental

study is performed at a well-controlled/simulated additive noise conditions and may have oversimplified environments in the actual busy clinical setting, where healthcare settings that are loud and rowdy result in unforeseen non-additive noise pollution. Moreover, the selections of digital stethoscopes in this study are not intended to be a representation of all digital stethoscopes available commercially, nor expressing opinions concerning their performances in noisy settings.

Chapter 6   Conclusions and Recommendations

6.1 Conclusions

This thesis aimed to establish the feasibility of assessing lung functions via acoustic imaging by locating nidus, enabling smart respiratory therapy through frequent and continual monitoring of lung functions. The suitability of the equipment-to-patient acoustic imaging approach to provide an early and frequent assessment of lung functions and enable targeted airway therapy, namely when movement is restricted in the community, and the limited accessibility to the equipment was illustrated in this thesis, as most studies have focused on the patient-to-equipment approach, and mainly on a non-acoustic approach. Important information about alterations between healthy and unhealthy conditions in the airway structure caused by CRD, injury or foreign objects such as tumours pressing on the airway can be identified with sound transmission in the respiratory system; however, less attention has been paid to the mechanisms of sound transmission in the respiratory system and the correlation between lung sound changes and lung structure. Additionally, the acoustic imaging systems setup, including the sensor number and sensing area, has been empirical, making acoustic imaging hard for lung function assessment.

The potential and limitations of bedside/portable acoustic imaging in the continual and frequent assessment of lung function were described in Chapter 2. Bedside/portable acoustic imaging has shown the potential to achieve similar results as the traditional imaging modality with the small number of selected studies in Chapter 2. Furthermore, acoustic imaging has the potential for home-based usage as no medical interpretation of the results is required. From the literature findings in Chapter 2, further acoustic imaging research, especially the direction in converting lung sound into images for assessment is required, since there is no gold standard for measuring the obstructed airway regionally and frequently for bedside/portable acoustic imaging.

A novel airway model was first developed to study the sound pressure in the airway, airway structural conditions with CRD conditions, such as asthma and COPD, and the optimisation of the acoustic imaging system, as presented in Chapter 3. The computed airway model is validated against actual lung sound recording and achieved 89% similarity. The proposed airway model results are as expected, e.g., when airways thicken, the airflow impedance increases, leading to a decrease in the overall intensity of the acoustic lung imaging. Simulation studies based on the model are used to analyse the practicality and the extreme

design of the acoustic imaging system on the resolution of the located nidus. For instance, a practical system design with sensor numbers between 35 and 4 may recognise nidus length anywhere between 20 and 73 mm. On the other hand, an extreme system design with more than 1000 sensors can recognise greater nidus resolution at under 10 mm. Additionally, this model can be utilised to offer recommendations for acoustic imaging system design and assess the number of sensors and sensing diameter in current acoustic imaging systems. The geographic detection of nidus length allows for analysing of HFCWO therapy results.

Next, ambient noise is an inevitable interference that can obscure the existence of interesting sound trends in lung sound recording. Interferences can result in undesirable false positives; hence, noise reduction or denoising is crucial in lung sound signal processing. A unique WATV-Wiener filter was proposed in Chapter 4 that significantly enhances the captured signal quality while preserving the critical characteristics of a lung sound signal. The WATV-Wiener hybrid technique proposed here considers the noisy signal's significant and insignificant (noise) wavelet coefficients. An intensive analysis of selecting and fine-tuning the WATV-Wiener filter parameters was performed. Through a series of simulation and experimental studies, the proposed WATV-Wiener filter is less sensitive to the variation of SNR values of the input signal.

Lastly, a wearable, extensible, and robust lung sound acquisition and acoustic imaging system was developed in Chapter 5, capturing accurate lung sounds in a noisy environment and producing more accurate acoustic images for continual lung function assessment. The developed system is integrated with the denoising filter proposed in Chapter 4. The system is low-cost, ranging from USD 120 to 280, for a typical 12 to 24 acoustic sensors array [21, 24, 30, 31, 35, 36] recording lung sound simultaneously at different locations, as compared to digital stethoscopes [37, 38] USD 300, with only single data point collection. The system has demonstrated the preservation of lung sound signals of interest while minimizing external interferences. The system has demonstrated a superior sensing sensitivity region regarding the recorded signal power spectrum. The lung signals were then converted into acoustic lung images for experimental investigation and analysis. The nidus detection results via acoustic imaging in the experimental study were validated and supported by the sensor distribution and acoustic imaging resolution modelling studies in Chapter 3.

In summary, this thesis identified the potential of assessing lung function via acoustic imaging (Chapter 2), presented an airway model and optimise acoustic sensor array design through simulation (Chapter 3), developed an optimal denoising filter to remove unwanted

ambient noise from lung sound signals (Chapter 4), and lastly, designed a robust lung sound acquisition and acoustic imaging system through software and hardware development (Chapter 5) that can produce reliable lung function assessment. From the findings in this thesis, acoustic monitoring can be performed with highly accurate and inexpensive sensors, making early and continual lung function assessment via acoustic devices suitable for hospital and home monitoring of CRD.

6.2 Recommendations

The results of this thesis show that acoustic lung imaging transmuted from acquired lung sounds is a promising technique for early and continual assessment of lung function, locating nidus regions, and enabling smart respiratory therapy. The following recommendations are suggested for future research in this area:

1) The impact of controlled lung sound generation on lung function assessment via lung sounds and acoustic imaging can be explored. Volunteers or patients were asked to breathe normally in this thesis, i.e., inhalation and exhalation were non-controlled during the lung sound recording, including respiratory sounds shortlisted from the database. This approach is useful for research that focuses on improving lung sound acquisition detected at the chest wall in noisy environments such as clinics and homes. Although requesting patients with CRD to hold their breath may not be practical, the direct effect of breath-holding can be investigated. Additionally, the combination of sounds generated from the chest and an external sound source input via the mouth can be explored. Respiratory sound signals and impedances can be recorded at the chest wall with an external input sound source into the trachea and branching network of airways via the mouth, as the external sound must pass through the same airway path to reach the chest wall. The external input sound source, such as frequencies, may be specifically tailored to the research to increase frequency response, frequency range, and intensity of the captured signal.

2) Towards a more functional and multi-scale airway model for airway impedance response and lung function assessment via acoustic imaging. In this thesis, assumptions and generalisations have been made for the lung mechanical simulations – controlled by more complex biological principles. A lung model with different volumes, in terms of the lung's length, width, and height, at different respiratory cycle stages would be necessary for studies of complete respiratory cycles over the

examination duration. Additionally, movement of the ribcage during the respiratory cycle can be explored. Integrating these biological conditions into airway mechanical modelling and simulations may yield results close to the actual functional response of the lungs. Other physical airway trees, such as the Weibel airway model's airway generations (layer), branching angles characteristics, airway diameters, and lengths, can be explored and validate its performance.

3) Effect of signal and image processing. Future research should examine the hardware system's processing power in detail and consider real-world usage scenarios, such as respiratory conditions, to verify the system's signal quality. This thesis centred around reducing external noise, such as ambient noise pollution and human speech. The addition of heart sound interference, which can be a standalone topic on its own, can be investigated to compare the filter performance.

The generation of acoustic imaging is based on the mean airway impedance response or sound pressure within a known sensing area. An experiment can be performed to determine a weighted ratio between a sensor sensing diameter and the distance away from the sound source. Incorporating an additional weighted ratio to individual airway segments may potentially enhance and improve the computation of acoustic imaging with the proposed model. A more precise understanding of sensors sensing area, airway-generated signals and pathology correlations could also lead to becoming a relevant and useful diagnostic tool.

4) Mobile and intuitive lung function assessment, particularly for non-healthcare trained personnel. The use of an array of sensors is a remarkable way to increase SNR and offer localisation information that motivates more research. There are various external sensor actuation techniques depending on the system and location. It is best to choose an actuator based on its size (which affects portability, price, and comfort), intensity at the desired frequencies, and current draw (which impacts battery life). In addition to monitoring, the ideal system would provide an additional study into how disease-related changes in lung parameters. Wireless lung sounds data transmission, and cloud storage are becoming commonplace in medical equipment outside of hospitals. By enabling clinicians or doctors to acquire real-time information on acoustic indicators of a patient's lung function and modify the course of therapy as necessary, wireless lung sounds data transmission and storage has the potential to expand and develop the area of telemedicine. This is possible with the

help of popular mobile app solutions. Although the approach is already available in some digital stethoscopes [37, 38], the approach has yet to be established for multi-sensor recording systems. Hence, the approach offers greater monitoring capabilities and the context for patient treatment regarding various demographics and diseases.

Appendix A: Search Strategies and Point allocation

A1   Search strategies.

Scopus

Step	Search query	Results
#1	ALL (bedside AND acoustic AND lung AND imaging OR bedside AND acoustic AND pulmonary AND imaging OR bedside AND acoustic AND respiratory AND imaging OR portable AND acoustic AND lung AND imaging OR portable AND acoustic AND respiratory AND imaging OR bedside AND acoustic AND pulmonary AND imaging AND respiratory AND diseases) AND NOT tumor OR cancer OR cardiac OR animal	92

Pubmed/Medline

Step	Search query	Results
#1	(((((((("bedside"[All Fields] OR "bedsides"[All Fields]) AND ("acoust"[All Fields] OR "acoustical"[All Fields] OR "acoustically"[All Fields] OR "acoustics"[MeSH Terms] OR "acoustics"[All Fields] OR "acoustic"[All Fields]) AND ("lung"[MeSH Terms] OR "lung"[All Fields]) AND ("image"[All Fields] OR "image s"[All Fields] OR "imaged"[All Fields] OR "imager"[All Fields] OR "imager s"[All Fields] OR "imagers"[All Fields] OR "images"[All Fields] OR "imaging"[All Fields] OR "imaging s"[All Fields] OR "imagings"[All Fields])) OR ((("bedside"[All Fields] OR "bedsides"[All Fields]) AND ("acoust"[All Fields] OR "acoustical"[All Fields] OR "acoustically"[All Fields] OR "acoustics"[MeSH Terms] OR "acoustics"[All Fields] OR "acoustic"[All Fields]) AND ("lung"[MeSH Terms] OR "lung"[All Fields] OR "pulmonary"[All Fields]) AND ("image"[All Fields] OR "image s"[All Fields] OR "imaged"[All Fields] OR "imager"[All Fields] OR "imager	4

s"[All Fields] OR "imagers"[All Fields] OR "images"[All Fields] OR "imaging"[All Fields] OR "imaging s"[All Fields] OR "imagings"[All Fields]) OR (("bedside"[All Fields] OR "bedsides"[All Fields]) AND ("acoust"[All Fields] OR "acoustical"[All Fields] OR "acoustically"[All Fields] OR "acoustics"[MeSH Terms] OR "acoustics"[All Fields] OR "acoustic"[All Fields]) AND ("eur med j respir"[Journal] OR "respiratory"[All Fields]) AND ("image"[All Fields] OR "image s"[All Fields] OR "imaged"[All Fields] OR "imager"[All Fields] OR "imager s"[All Fields] OR "imagers"[All Fields] OR "images"[All Fields] OR "imaging"[All Fields] OR "imaging s"[All Fields] OR "imagings"[All Fields])) OR (("portability"[All Fields] OR "portable"[All Fields] OR "portables"[All Fields]) AND ("acoust"[All Fields] OR "acoustical"[All Fields] OR "acoustically"[All Fields] OR "acoustics"[MeSH Terms] OR "acoustics"[All Fields] OR "acoustic"[All Fields]) AND ("lung"[MeSH Terms] OR "lung"[All Fields]) AND ("image"[All Fields] OR "image s"[All Fields] OR "imaged"[All Fields] OR "imager"[All Fields] OR "imager s"[All Fields] OR "imagers"[All Fields] OR "images"[All Fields] OR "imaging"[All Fields] OR "imaging s"[All Fields] OR "imagings"[All Fields])) OR (("portability"[All Fields] OR "portable"[All Fields] OR "portables"[All Fields]) AND ("acoust"[All Fields] OR "acoustical"[All Fields] OR "acoustically"[All Fields] OR "acoustics"[MeSH Terms] OR "acoustics"[All Fields] OR "acoustic"[All Fields]) AND ("eur med j respir"[Journal] OR "respiratory"[All Fields]) AND ("image"[All Fields] OR "image s"[All Fields] OR "imaged"[All Fields] OR "imager"[All Fields] OR "imager s"[All Fields] OR "imagers"[All Fields] OR "images"[All Fields] OR "imaging"[All Fields] OR "imaging s"[All Fields] OR "imagings"[All Fields])) OR (("bedside"[All Fields] OR "bedsides"[All Fields]) AND ("acoust"[All Fields] OR "acoustical"[All Fields] OR "acoustically"[All Fields] OR "acoustics"[MeSH Terms] OR "acoustics"[All Fields] OR "acoustic"[All Fields]) AND ("lung"[MeSH Terms] OR "lung"[All Fields] OR "pulmonary"[All Fields]) AND ("image"[All Fields] OR "image s"[All Fields] OR "imaged"[All Fields] OR "imager"[All Fields] OR "imager s"[All Fields] OR "imagers"[All Fields] OR "images"[All Fields] OR "imaging"[All Fields] OR "imaging s"[All Fields] OR "imagings"[All

| | Fields]))) AND ("respiration disorders"[MeSH Terms] OR ("respiration"[All Fields] AND "disorders"[All Fields]) OR "respiration disorders"[All Fields] OR ("respiratory"[All Fields] AND "diseases"[All Fields]) OR "respiratory diseases"[All Fields]) NOT ("cysts"[MeSH Terms] OR "cysts"[All Fields] OR "cyst"[All Fields] OR "neurofibroma"[MeSH Terms] OR "neurofibroma"[All Fields] OR "neurofibromas"[All Fields] OR "tumor s"[All Fields] OR "tumoral"[All Fields] OR "tumorous"[All Fields] OR "tumour"[All Fields] OR "neoplasms"[MeSH Terms] OR "neoplasms"[All Fields] OR "tumor"[All Fields] OR "tumour s"[All Fields] OR "tumoural"[All Fields] OR "tumourous"[All Fields] OR "tumours"[All Fields] OR "tumors"[All Fields]) NOT ("cancer s"[All Fields] OR "cancerated"[All Fields] OR "canceration"[All Fields] OR "cancerization"[All Fields] OR "cancerized"[All Fields] OR "cancerous"[All Fields] OR "neoplasms"[MeSH Terms] OR "neoplasms"[All Fields] OR "cancer"[All Fields] OR "cancers"[All Fields]) NOT ("heart"[MeSH Terms] OR "heart"[All Fields] OR "cardiac"[All Fields]) NOT ("animals"[MeSH Terms:noexp] OR "animal"[All Fields]) | |

ScienceDirect

Step	Search query	Results
#1	bedside acoustic lung imaging OR bedside acoustic pulmonary imaging OR bedside acoustic respiratory imaging OR portable acoustic lung imaging OR portable acoustic respiratory imaging OR bedside acoustic pulmonary imaging NOT tumor NOT animal NOT cardiac	346

Web of Science

Step	Search query	Results

| #1 | (((((((((TS=(bedside acoustic lung imaging)) OR TS=(bedside acoustic pulmonary imaging)) OR TS=(bedside acoustic respiratory imaging)) OR TS=(portable acoustic lung imaging)) OR TS=(portable acoustic respiratory imaging)) OR TS=(bedside acoustic pulmonary imaging)) AND TS=(respiratory diseases)) NOT TS=(tumor)) NOT TS=(cancer)) NOT TS=(cardiac) | 30 |

*TS denotes topic

SciELO Preprints

Go to https://preprints.scielo.org/index.php/scielo/preprints

Step	Search query	Results
#1	bedside acoustic lung imaging OR bedside acoustic pulmonary imaging OR bedside acoustic respiratory imaging OR portable acoustic lung imaging OR portable acoustic respiratory imaging OR bedside acoustic pulmonary imaging and respiratory diseases NOT tumor OR cancer OR cardiac	0

Google Scholar

Step	Search query	Results
#1	bedside acoustic lung imaging OR bedside acoustic pulmonary imaging OR bedside acoustic respiratory imaging OR portable acoustic lung imaging OR portable acoustic respiratory imaging -tumor -OR -cancer -OR -cardiac	24

A2   Newcastle-Ottawa Scale adapted for cross-sectional studies.

Selection (max 5 stars ★★★★★):

1. Representativeness of the sample:

    a. Truly representative of the average in the target population. ★ (all subjects or random sampling)

    b. Somewhat representative of the average in the target group. ★ (non-random sampling)

    c. Selected group of users/convenience sample.

    d. No description of the derivation of the included subjects.

2. Sample size:

    a. Justified and satisfactory (including sample size calculation). ★

    b. Not justified.

    c. No information provided.

3. Non-respondents:

    a. Comparability between respondents and non-respondents' characteristics is established, and the response rate is satisfactory. ★★

    b. Unsatisfactory recruitment rate, no summary data on non-respondents.

    c. No information provided

4. Ascertainment of the exposure (risk factor):

    a. Validated measurement tool. ★★

b. Non-validated measurement tool, but the tool is available or described. ★

c. No description of the measurement tool.

Comparability (Maximum 2 stars):

1) The subjects in different outcome groups are comparable, based on the study design or analysis. Confounding factors are controlled.

a. The study controls for the most important factor (select one). ★

b. The study control for any additional factor. ★

Outcome (Maximum 3 stars):

1. Assessment of outcome:

a. Independent blind assessment using objective validated laboratory methods. ★★

b. Unblinded assessment using objective validated laboratory methods. ★★

c. Used non-standard or non-validated laboratory methods with gold standard. ★

d. No description/non-standard laboratory methods used.

2. Statistical test:

a. Statistical test used to analyse the data clearly described, appropriate and measures of association presented including confidence intervals and probability level (p value). ★

b. Statistical test not appropriate, not described or incomplete.

Cross-sectional Studies: Very Good Studies: 9-10 points. Good Studies: 7-8 points. Satisfactory Studies: 5-6 points. Unsatisfactory Studies: 0 to 4 points

This scale has been adapted from the Newcastle-Ottawa Quality Assessment Scale for cohort studies to provide quality assessment of cross-sectional studies [67].

Bibliography

[1]   C. S. Lee, M. Li, Y. Lou, and R. Dahiya, "Lung imaging system for targeted therapy," U.S. Application No. 20230104486, Oct 05, 2022.

[2]   C. S. Lee, M. Li, Y. Lou, and R. Dahiya, "Restoration of Lung Sound Signals Using a Hybrid Wavelet-Based Approach," *IEEE Sensors Journal,* vol. 22, no. 20, pp. 19700-19712, 2022.

[3]   C. S. Lee, Y. Lou, M. Li, Q. H. Abbasi, and M. A. Imran, "Locating nidi for high-frequency chest wall oscillation smart therapy via acoustic imaging of lung airways as a spatial network," in *IEEE Access*, doi: 10.1109/ACCESS.2023.3317443.

[4]   C. S. Lee, M. Li, Y. Lou, Q. H. Abbasi, and M. A. Imran, "Acoustic lung imaging utilized in continual assessment of patients with obstructed airway: A systematic review," *Sensors*, vol. 23, no. 13, p. 6222, Jul. 2023.

[5]   C. S. Lee, M. Li, Y. Lou, Q. H. Abbasi, and M. A. Imran, "An acoustic system of sound acquisition and imaging generation for frequent and reliable lung function assessment," Submitted to *IEEE Sensors Journal*, Jun 02, 2023.

[6]   C. S. Lee, M. Li, Y. Lou, and R. Dahiya, "A hybrid approach of wavelet-based total variation and Wiener filter to denoise adventitious lung sound signal for an accurate assessment," in *2022 IEEE International Conference on Consumer Electronics (ICCE)*, 2022, pp. 1-6.

[7]   C. S. Lee, M. Li, Y. Lou, and R. Dahiya, "Selecting efficient parameters thresholds for a hybrid wavelet-based total variation and Wiener filter for denoising lung sound signals," in *2022 6th International Conference on Imaging, Signal Processing and Communications (ICISPC)*, 2022, pp. 106-110.

[8]   C. S. Lee, M. Li, Y. Lou, and R. Dahiya, "Modeling and Simulation of Pulmonary Acoustic Signal and Imaging for Lung Function Assessment," *2023 IEEE International Conference on Consumer Electronics (ICCE)*, Las Vegas, NV, USA, 2023, pp. 01-06.

[9]   C. S. Lee, M. Li, Y. Lou, and R. Dahiya, "The Effect of Sensor Array Design on Acoustic Imaging for Enhancing High-Frequency Chest Wall Oscillation Therapy," Presented at the *20th IEEE International Multi-Conference on Systems, Signals & Devices (SSD)*, Mahdia, Tunisia, 20-23 Feb 2023, 2023.

[10]   C. S. Lee, M. Li, Y. Lou, and R. Dahiya, "Design of a robust lung sound acquisition system for reliable acoustic lung imaging," Presented at the *2023 IEEE International Ultrasonics Symposium*, Montreal, Quebec, Canada, Sep 03, 2023.

[11]   Z. Dai, Y. Peng, H. A. Mansy, R. H. Sandler, and T. J. Royston, "Experimental and computational studies of sound transmission in a branching airway network embedded in a compliant viscoelastic medium," *Journal of sound and vibration,* vol. 339, pp. 215-229, 2015.

[12]   J. J. Fredberg and A. Hoenig, "Mechanical response of the lungs at high frequencies," *Journal of Biomechanical Engineering,* vol. 100, no. 2, pp. 57-66, 1978.

[13]   R. H. Habib, R. B. Chalker, B. Suki, and A. C. Jackson, "Airway geometry and wall mechanical properties estimated from subglottal input impedance in humans," *Journal of Applied Physiology,* vol. 77, no. 1, pp. 441-451, 1994.

[14]   C. M. Ionescu, P. Segers, and R. D. Keyser, "Mechanical properties of the respiratory system derived from morphologic insight," *IEEE Transactions on Biomedical Engineering,* vol. 56, no. 4, pp. 949-959, 2009.

[15]   D. W. Kaczka and R. L. Dellacá, "Oscillation mechanics of the respiratory system: applications to lung disease," *Critical reviews in biomedical engineering,* vol. 39, no. 4, pp. 337-359, 2011.

[16]   A. L. James, P. D. Paré, and J. C. Hogg, "The mechanics of airway narrowing in asthma," *American Review of Respiratory Disease,* vol. 139, no. 1, pp. 242-246, 1989.

[17]   M. McIlwaine, J. Bradley, J. S. Elborn, and F. Moran, "Personalising airway clearance in chronic lung disease," *European Respiratory Review,* vol. 26, no. 143, p. 160086, 2017.

[18]   F. M. E. Franssen *et al.*, "Personalized medicine for patients with COPD: where are we?," *International journal of chronic obstructive pulmonary disease,* vol. 14, pp. 1465-1484, 2019.

[19]   C. Ohashi, S. Akiguchi, and M. Ohira, "Development of a remote health monitoring system to prevent frailty in elderly home-care patients with COPD," *Sensors*, vol. 22, no. 7. doi: 10.3390/s22072670

[20]   S. Janjua, D. Carter, C. J. D. Threapleton, S. Prigmore, and R. T. Disler, "Telehealth interventions: remote monitoring and consultations for people with chronic obstructive pulmonary disease (COPD)," *Cochrane Database of Systematic Reviews,* no. 7, 2021.

[21]   D. Bing, K. Jian, S. Long-feng, T. Wei, and Z. Hong-wen, "Vibration response imaging: a novel noninvasive tool for evaluating the initial therapeutic effect of noninvasive positive pressure ventilation in patients with acute exacerbation of

chronic obstructive pulmonary disease," *Respiratory Research,* vol. 13, no. 1, p. 65, 2012/08/02 2012.

[22]   R. P. Dellinger, J. E. Parrillo, A. Kushnir, M. Rossi, and I. Kushnir, "Dynamic visualization of lung sounds with a vibration response device: A case series," *Respiration,* vol. 75, no. 1, pp. 60-72, 2008.

[23]   H. Jiang, J. Chen, J. Cao, L. Mu, Z. Hu, and J. He, "Evaluation of vibration response imaging (VRI) technique and difference in VRI indices among non-smokers, active smokers and passive smokers," *Medical science monitor : international medical journal of experimental and clinical research,* vol. 21, pp. 2170-2177, 2015.

[24]   C. Shi *et al.*, "Assessment of regional ventilation distribution: Comparison of vibration response imaging (VRI) with electrical impedance tomography (EIT)," *PLOS ONE,* vol. 9, no. 1, p. e86638, 2014.

[25]   G. Hahn, I. Sipinkova, F. Baisch, and G. Hellige, "Changes in the thoracic impedance distribution under different ventilatory conditions," *Physiological measurement,* vol. 16, no. 3A, p. A161, 1995.

[26]   I. Frerichs *et al.*, "Detection of local lung air content by electrical impedance tomography compared with electron beam CT," *Journal of applied physiology,* vol. 93, no. 2, pp. 660-666, 2002.

[27]   J. A. Victorino *et al.*, "Imbalances in regional lung ventilation: a validation study on electrical impedance tomography," *American journal of respiratory and critical care medicine,* vol. 169, no. 7, pp. 791-800, 2004.

[28]   M. Mineshita *et al.*, "The correlation between lung sound distribution and pulmonary function in COPD patients," *PLOS ONE,* vol. 9, no. 9, p. e107506, 2014.

[29]   A. Rao, E. Huynh, T. J. Royston, A. Kornblith, and S. Roy, "Acoustic methods for pulmonary diagnosis," *IEEE Reviews in Biomedical Engineering,* vol. 12, pp. 221-239, 2019.

[30]   M. Kompis, H. Pasterkamp, and G. R. Wodicka, "Acoustic imaging of the human chest," *Chest,* vol. 120, no. 4, pp. 1309-1321, 2001.

[31]   S. Charleston-Villalobos, S. Cortés-Rubiano, R. González-Camerena, G. Chi-Lem, and T. Aljama-Corrales, "Respiratory acoustic thoracic imaging (RATHI): Assessing deterministic interpolation techniques," *Medical and Biological Engineering and Computing,* vol. 42, no. 5, pp. 618-626, 2004.

[32]   M. Vicky, K. Minseok, and C. Se-woon, "Prospects of structural similarity index for medical image analysis," *Applied Sciences*, vol. 12, no. 8. p. 3754, Apr. 2022.

[33] S. K. Gupta, R. Pal, A. Ahmad, F. Melandsø, and A. Habib, "Image denoising in acoustic microscopy using block-matching and 4D filter," *Scientific Reports*, vol. 13, no. 1, p. 13212, Aug. 2023.

[34] W. Zhou, A. C. Bovik, H. R. Sheikh, and E. P. Simoncelli, "Image quality assessment: from error visibility to structural similarity," *IEEE Transactions on Image Processing,* vol. 13, no. 4, pp. 600-612, 2004.

[35] S. Lev *et al.*, "Computerized lung acoustic monitoring can help to differentiate between various chest radiographic densities in critically ill patients," *Respiration,* vol. 80, no. 6, pp. 509-516, 2010.

[36] M. Yigla, M. Gat, J.-J. Meyer, P. J. Friedman, T. M. Maher, and J. M. Madison, "Vibration response imaging technology in healthy subjects," *American Journal of Roentgenology,* vol. 191, no. 3, pp. 845-852, 2008.

[37] 3M Littmann Electronic Stethoscope Model 3200. [Online] Available: https://www.3m.com.sg/3M/en_SG/p/d/v000179163/ (accessed 13 Oct 2022)

[38] ThinklabsOne. [Online] Available: https://www.thinklabs.com/ (accessed 13 Oct 2022)

[39] H. Moosapour, F. Saeidifard, M. Aalaa, A. Soltani, and B. Larijani, "The rationale behind systematic reviews in clinical medicine: a conceptual framework," *Journal of Diabetes & Metabolic Disorders,* vol. 20, no. 1, pp. 919-929, 2021.

[40] S. Gopalakrishnan and P. Ganeshkumar, "Systematic reviews and meta-analysis: Understanding the best evidence in primary healthcare," *Journal of Family Medicine and Primary Care,* vol. 2, no. 1, 2013.

[41] J. Minov and S. Stoleski, "Chronic obstructive airways diseases: where are we now?," *Open Respir Med J,* vol. 9, pp. 37-8, 2015.

[42] A. C. DeGraff and A. Bouhuys, "Mechanics of air flow in airway obstruction," *Annual Review of Medicine,* vol. 24, no. 1, pp. 111-134, 1973.

[43] Forum of International Respiratory Societies, "The global impact of respiratory disease – second edition," Sheffield, European Respiratory Society 2017.

[44] World Health Organization Coronavirus Disease (COVID-19) Dashboard. Available: https://covid19.who.int/ (accessed on 18 May 2023)

[45] G. Leemans *et al.*, "The effectiveness of a mobile high-frequency chest wall oscillation (HFCWO) device for airway clearance," *Pediatric Pulmonology,* vol. 55, no. 8, pp. 1984-1992, 2020.

[46] RespIn 11 Bronchial Clearance System. Available: http://www.respin-usa.com/ (accessed on 18 May 2023)

[47]   The Monarch Airway Clearance System. Available: https://www.hillrom.com/en/products/the-monarch-airway-clearance-system/ (accessed on 18 May 2023)

[48]   H. Pinnock, C. Y. Hui, and J. F. M. van Boven, "Implementation of digital home monitoring and management of respiratory disease," *Current Opinion in Pulmonary Medicine*, vol. 29, no. 4, 2023.

[49]   M. Garg et al., "Radiation exposure and lifetime attributable risk of cancer incidence and mortality from low- and standard-dose CT chest: Implications for COVID-19 pneumonia subjects," *Diagnostics*, vol. 12, no. 12, p. 3043, Dec. 2022.

[50]   H.-M. Shi, Z.-C. Sun, and F.-H. Ju, "Understanding the harm of low-dose computed tomography radiation to the body (Review)," *Exp Ther Med*, vol. 24, no. 2, p. 534, Aug. 2022.

[51]   B. Fanara, C. Manzon, O. Barbot, T. Desmettre, and G. Capellier, "Recommendations for the intra-hospital transport of critically ill patients," *Critical Care,* vol. 14, no. 3, p. R87, 2010.

[52]   J J. Szem, H. Lynn, F. Eva, K. Sandip, K. John, and B. Philip, "High-risk intrahospital transport of critically ill patients: safety and outcome of the necessary "road trip"," *Critical Care Medicine*, pp. 1660-1666, 1995.

[53]   A. Marques *et al.*, "Improving access to community-based pulmonary rehabilitation: 3R protocol for real-world settings with cost-benefit analysis," *BMC Public Health,* vol. 19, no. 1, p. 676, 2019.

[54]   A. D'Andrea *et al.*, "Multimodality imaging in COVID-19 patients: A key role from diagnosis to prognosis," *World Journal of Radiology*, pp. 261-271, 2020.

[55]   J. Niu *et al.*, "Detection of sputum by interpreting the time-frequency distribution of respiratory sound signal using image processing techniques," *Bioinformatics,* vol. 34, no. 5, pp. 820-827, 2018.

[56]   M. Kolodziej, M. J. de Veer, M. Cholewa, G. F. Egan, and B. R. Thompson, "Lung function imaging methods in cystic fibrosis pulmonary disease," *Respir Res,* vol. 18, no. 1, p. 96, 2017.

[57]   B. W. Ramsey, "Use of lung imaging studies as outcome measures for development of new therapies in cystic fibrosis," *Proceedings of the American Thoracic Society,* vol. 4, no. 4, pp. 359-363, 2007.

[58]   S. Dubsky and A. Fouras, "Imaging regional lung function: a critical tool for developing inhaled antimicrobial therapies," *Adv Drug Deliv Rev,* vol. 85, pp. 100-9, 2015.

[59]   E. Lauwers, K. Ides, K. Van Hoorenbeeck, and S. Verhulst, "Outcome measures for airway clearance techniques in children with chronic obstructive lung diseases: a systematic review," *Respiratory Research,* vol. 21, no. 1, p. 217, 2020.

[60]   I. M. L. Augustin *et al.*, "Multidimensional outcome assessment of pulmonary rehabilitation in traits-based clusters of COPD patients," *PLOS ONE,* vol. 17, no. 2, p. e0263657, 2022.

[61]   A. L. Oliveira and A. S. Marques, "Outcome measures used in pulmonary rehabilitation in patients with acute exacerbation of chronic obstructive pulmonary disease: A systematic review," *Physical Therapy,* vol. 98, no. 3, pp. 191-204, 2018.

[62]   M. J. Page *et al.*, "The PRISMA 2020 statement: An updated guideline for reporting systematic reviews," *PLOS Medicine,* vol. 18, no. 3, p. e1003583, 2021.

[63]   A. Cooke, D. Smith, and A. Booth, "Beyond PICO: The SPIDER tool for qualitative evidence synthesis," *Qualitative Health Research,* vol. 22, no. 10, pp. 1435-1443, 2012.

[64]   A. M. Methley, S. Campbell, C. Chew-Graham, R. McNally, and S. Cheraghi-Sohi, "PICO, PICOS and SPIDER: A comparison study of specificity and sensitivity in three search tools for qualitative systematic reviews," *BMC Health Services Research,* vol. 14, no. 1, p. 579, 2014.

[65]   L.-L. Ma, Y.-Y. Wang, Z.-H. Yang, D. Huang, H. Weng, and X.-T. Zeng, "Methodological quality (risk of bias) assessment tools for primary and secondary medical studies: what are they and which is better?," *Military Medical Research,* vol. 7, no. 1, p. 7, 2020.

[66]   A. Moskalewicz and M. Oremus, "No clear choice between Newcastle–Ottawa scale and appraisal tool for cross-sectional studies to assess methodological quality in cross-sectional studies of health-related quality of life and breast cancer," *Journal of Clinical Epidemiology,* vol. 120, pp. 94-103, 2020.

[67]   R. Herzog, M. J. Álvarez-Pasquin, C. Díaz, J. L. Del Barrio, J. M. Estrada, and Á. Gil, "Are healthcare workers' intentions to vaccinate related to their knowledge, beliefs and attitudes? A systematic review," *BMC Public Health,* vol. 13, no. 1, p. 154, 2013.

[68]   Z. Jambrik *et al.*, "Usefulness of ultrasound lung comets as a nonradiologic sign of extravascular lung water," *The American Journal of Cardiology,* vol. 93, no. 10, pp. 1265-1270, 2004.

[69]   R. P. Dellinger *et al.*, "Regional distribution of acoustic-based lung vibration as a function of mechanical ventilation mode," *Critical Care,* vol. 11, no. 1, p. R26, 2007.

[70]   K. K. Guntupalli, R. M. Reddy, R. H. Loutfi, P. M. Alapat, V. D. Bandi, and N. A. Hanania, "Evaluation of obstructive lung disease with vibration response imaging," *Journal of Asthma,* vol. 45, no. 10, pp. 923-930, 2008.

[71]   K. Gorska *et al.*, "Comparison of endobronchial ultrasound and high resolution computed tomography as tools for airway wall imaging in asthma and chronic obstructive pulmonary disease," *Respiratory Medicine,* vol. 117, pp. 131-138, 2016.

[72]   N. San Sebastian Ruiz, I. Rodríguez Albarrán, I. Gorostiza, I. Galletebeitia Laka, C. Delgado Lejonagoitia, and F. Samson, "Point-of-care lung ultrasound in children with bronchiolitis in a pediatric emergency department," *Archives de Pédiatrie,* vol. 28, no. 1, pp. 64-68, 2021.

[73]   H. Jiang, J. Chen, J. Cao, L. Mu, Z. Hu, and J. He, "Application of vibration response imaging technology in patients with community-acquired pneumonia before and after the treatment," *Experimental and therapeutic medicine,* vol. 13, no. 6, pp. 3433-3437, 2017.

[74]   L. Ambroggio *et al.*, "Lung ultrasonography: A viable alternative to chest radiography in children with suspected pneumonia?," *The Journal of Pediatrics,* vol. 176, pp. 93-98.e7, 2016.

[75]   D. Anantham, F. J. F. Herth, A. Majid, G. Michaud, and A. Ernst, "Vibration response imaging in the detection of pleural effusions: A feasibility study," *Respiration,* vol. 77, no. 2, pp. 166-172, 2009.

[76]   L. Qing-xia *et al.*, "Vibration response imaging in idiopathic pulmonary fibrosis: A pilot study," *Respiratory Care,* vol. 59, no. 7, p. 1071, 2014.

[77]   Y. Tung-Chen *et al.*, "Correlation between chest computed tomography and lung ultrasonography in patients with Coronavirus Disease 2019 (COVID-19)," *Ultrasound in Medicine & Biology,* vol. 46, no. 11, pp. 2918-2926, 2020.

[78]   E. P. C. Giorno *et al.*, "Point-of-care lung ultrasound imaging in pediatric COVID-19," *The Ultrasound Journal,* vol. 12, no. 1, p. 50, 2020.

[79]   A. M. Musolino *et al.*, "Lung ultrasound in children with COVID-19: Preliminary findings," *Ultrasound in Medicine & Biology,* vol. 46, no. 8, pp. 2094-2098, 2020.

[80]   F. Rizzetto *et al.*, "Correlation between lung ultrasound and chest CT patterns with estimation of pulmonary burden in COVID-19 patients," *European Journal of Radiology,* vol. 138, p. 109650, 2021.

[81]   P. A. Modesti *et al.*, "Panethnic differences in blood pressure in Europe: A systematic review and meta-analysis," *PLOS ONE,* vol. 11, no. 1, p. e0147601, 2016.

[82] R. Raheja, M. Brahmavar, D. Joshi, and D. Raman, "Application of Lung ultrasound in critical care setting: A review," *Cureus,* vol. 11, no. 7, pp. e5233-e5233, 2019.

[83] D. Chiumello, S. Froio, B. Bouhemad, L. Camporota, and S. Coppola, "Clinical review: Lung imaging in acute respiratory distress syndrome patients - an update," *Critical Care,* vol. 17, no. 6, p. 243, 2013.

[84] M. Nissan and N. Gavriely, "A microcomputer based lung sounds analysis," *Computer methods and programs in biomedicine,* vol. 40, no. 1, pp. 7-13, 1993.

[85] J. Cook, M. Umar, F. Khalili, and A. Taebi, "Body acoustics for the non-invasive diagnosis of medical conditions," *Bioengineering*, vol. 9, no. 4, p. 149, Apr. 2022.

[86] J. Wedel, P. Steinmann, M. Štrakl, M. Hriberšek, Y. Cui, and J. Ravnik, "Anatomy matters: The role of the subject-specific respiratory tract on aerosol deposition — A CFD study," *Computer Methods in Applied Mechanics and Engineering*, vol. 401, p. 115372, Nov. 2022.

[87] AffloVest. "Moblie Airway Clearance Therapy." [Online] Available: https://afflovest.com/ (accessed 30 Aug 2023, 2023).

[88] N. R. Council, *Health risks from exposure to low levels of ionizing radiation: BEIR VII phase 2*. National Academies Press, 2006.

[89] Sciospec. "Electrical Impedance Tomography." [Online] Available: https://www.sciospec.com/eit/ (accessed 30 Aug 2023, 2023).

[90] M. H. Tawhai, P. Hunter, J. Tschirren, J. Reinhardt, G. McLennan, and E. A. Hoffman, "CT-based geometry analysis and finite element models of the human and ovine bronchial tree," *Journal of Applied Physiology,* vol. 97, no. 6, pp. 2310-2321, 2004.

[91] C. D. Murray, "A relationship between circumference and weights in trees and its bearing on branching angles," *Journal of General Physiology,* vol. 10, no. 5, pp. 725-729, 1927.

[92] S. Nousias, E. I. Zacharaki, and K. Moustakas, "AVATREE: An open-source computational modelling framework modelling Anatomically Valid Airway TREE conformations," *PLOS ONE,* vol. 15, no. 4, p. e0230259, 2020.

[93] B. Henry and T. J. Royston, "A multiscale analytical model of bronchial airway acoustics," *The Journal of the Acoustical Society of America,* vol. 142, no. 4, p. 1774, 2017.

[94] S. N. Sivanandam, *Electric Circuit Analysis*. Sangam Books Ltd, 2002.

[95] C. A. Whitfield, P. Latimer, A. Horsley, J. M. Wild, G. J. Collier, and O. E. Jensen, "Spectral graph theory efficiently characterizes ventilation heterogeneity in lung

airway networks," *Journal of The Royal Society Interface,* vol. 17, no. 168, p. 20200253, 2020.

[96]   S. Anzinger, J. Manz, C. Bretthauer, U. Krumbein, and A. Dehé, "Acoustic transmission line based modelling of microscaled channels and enclosures," *The Journal of the Acoustical Society of America,* vol. 145, no. 2, pp. 968-976, 2019.

[97]   S. Deumić, N. Crnčević, and I. Zolota, "Respiratory System Dynamical Mechanical Properties: Modeling in Time and Frequency Domain," in *CMBEBIH 2021*, 2021: Springer International Publishing, pp. 47-57.

[98]   F. B. Daniels, "Acoustical Impedance of Enclosures," *The Journal of the Acoustical Society of America,* vol. 19, no. 4, pp. 569-571, 1947.

[99]   J. J. Fredberg and J. A. Moore, "The distributed response of complex branching duct networks," *The Journal of the Acoustical Society of America,* vol. 63, no. 3, pp. 954-961, 1978.

[100]   A. H. Benade, "On the Propagation of Sound Waves in a Cylindrical Conduit," *The Journal of the Acoustical Society of America,* vol. 44, no. 2, pp. 616-623, 1968.

[101]   K. Horsfield, "Morphometry of airways," *Comprehensive Physiology,* pp. 75-88, 2011, https://doi.org/10.1002/cphy.cp030307.

[102]   I. B. Crandall, *Theory of vibrating systems and sound*. Creative Media Partners, LLC, 1927.

[103]   M. Sarkar, I. Madabhavi, N. Niranjan, and M. Dogra, "Auscultation of the respiratory system," *Annals of thoracic medicine,* vol. 10, no. 3, pp. 158-168, 2015.

[104]   B. M. Rocha *et al.*, "An open access database for the evaluation of respiratory sound classification algorithms," *Physiological Measurement,* vol. 40, no. 3, p. 035001, 2019.

[105]   J. Kosciuch, R. Krenke, K. Gorska, M. Zukowska, M. Maskey-Warzechowska, and R. Chazan, "Airway dimensions in asthma and COPD in high resolution computed tomography: Can we see the difference?," *Respiratory Care,* vol. 58, no. 8, p. 1335, 2013.

[106]   F. Deveci, A. Murat, T. Turgut, E. Altuntaş, and M. H. Muz, "Airway Wall thickness in patients with COPD and healthy current smokers and healthy non-smokers: Assessment with high resolution computed tomographic scanning," *Respiration,* vol. 71, no. 6, pp. 602-610, 2004.

[107]   N. Awadh, N. L. Müller, C. S. Park, R. T. Abboud, and J. M. FitzGerald, "Airway wall thickness in patients with near fatal asthma and control groups: assessment with

high resolution computed tomographic scanning," *Thorax,* vol. 53, no. 4, p. 248, 1998.

[108] H. A. Tiddens, P. D. Paré, J. C. Hogg, W. C. Hop, R. Lambert, and J. C. de Jongste, "Cartilaginous airway dimensions and airflow obstruction in human lungs," *American Journal of Respiratory and Critical Care Medicine,* vol. 152, no. 1, pp. 260-266, 1995.

[109] I. Orlandi *et al.,* "Chronic obstructive pulmonary disease: Thin-section CT measurement of airway wall thickness and lung attenuation," *Radiology,* vol. 234, no. 2, pp. 604-610, 2005.

[110] X. Xie, A. E. Dijkstra, J. M. Vonk, M. Oudkerk, R. Vliegenthart, and H. J. M. Groen, "Chronic respiratory symptoms associated with airway wall thickening measured by thin-slice low-dose CT," *American Journal of Roentgenology,* vol. 203, no. 4, pp. W383-W390, 2014.

[111] S. Asker, M. Asker, and B. Ozbay, "Evaluation of airway wall thickness via high-resolution computed tomography in mild intermittent asthma," *Respiratory Care,* vol. 59, no. 4, p. 550, 2014.

[112] D. Bradley and G. Roth, "Adaptive thresholding using the integral image," *Journal of Graphics Tools,* vol. 12, no. 2, pp. 13-21, 2007.

[113] Z. Duanmu *et al.*, "Design and implementation of an acoustic-vibration capacitive MEMS microphone," *AIP Advances,* vol. 12, no. 6, p. 065309, 2022.

[114] M. A. Shah, I. A. Shah, D.-G. Lee, and S. Hur, "Design Approaches of MEMS Microphones for Enhanced Performance," *Journal of Sensors,* vol. 2019, p. 9294528, 2019.

[115] S. A. Zawawi, A. A. Hamzah, B. Y. Majlis, and F. Mohd-Yasin, "A Review of MEMS Capacitive Microphones," *Micromachines (Basel),* vol. 11, no. 5, 2020.

[116] I. McLane, D. Emmanouilidou, J. E. West, and M. Elhilali, "Design and comparative performance of a robust lung auscultation system for noisy clinical settings," *IEEE Journal of Biomedical and Health Informatics,* vol. 25, no. 7, pp. 2583-2594, 2021.

[117] G. H. Kramer, K. Capello, B. Bearrs, A. Lauzon, and L. Normandeau, "Linear dimensions and volumes of human lungs obtained from CT images," *Health Physics,* vol. 102, no. 4, 2012.

[118] L. E. Ellington *et al.*, "Computerised lung sound analysis to improve the specificity of paediatric pneumonia diagnosis in resource-poor settings: protocol and methods for an observational study," *BMJ Open,* vol. 2, no. 1, p. e000506, 2012.

[119] A. Gurung, C. G. Scrafford, J. M. Tielsch, O. S. Levine, and W. Checkley, "Computerized lung sound analysis as diagnostic aid for the detection of abnormal lung sounds: A systematic review and meta-analysis," *Respiratory Medicine,* vol. 105, no. 9, pp. 1396-1403, 2011.

[120] E. Andrès, R. Gass, A. Charloux, C. Brandt, and A. Hentzler, "Respiratory sound analysis in the era of evidence-based medicine and the world of medicine 2.0," (in eng), *Journal of medicine and life,* vol. 11, no. 2, pp. 89-106, 2018.

[121] P. Forgacs, "Crackles and wheezes," *The Lancet,* vol. 290, no. 7508, pp. 203-205, 1967.

[122] N. Meslier, G. Charbonneau, and J. L. Racineux, "Wheezes," *European Respiratory Journal,* vol. 8, no. 11, p. 1942, 1995.

[123] F. Meng, Y. Wang, Y. Shi, and H. Zhao, "A kind of integrated serial algorithms for noise reduction and characteristics expanding in respiratory sound," *International journal of biological sciences,* vol. 15, no. 9, pp. 1921-1932, 2019.

[124] D. Emmanouilidou, E. D. McCollum, D. E. Park, and M. Elhilali, "Adaptive noise suppression of pediatric lung auscultations with real applications to noisy clinical settings in developing countries," *IEEE Transactions on Biomedical Engineering,* vol. 62, no. 9, pp. 2279-2288, 2015.

[125] R. Manwar, M. Zafar, and Q. Xu, "Signal and image processing in biomedical photoacoustic imaging: A Review," *Optics,* vol. 2, no. 1, 2021.

[126] Y. Ding and I. W. Selesnick, "Artifact-free wavelet denoising: Non-convex sparse regularization, convex optimization," *IEEE Signal Processing Letters,* vol. 22, no. 9, pp. 1364-1368, 2015.

[127] S. Ulukaya, G. Serbes, and Y. P. Kahya, "Performance comparison of wavelet based denoising methods on discontinuous adventitious lung sounds," in *2017 39th Annual International Conference of the IEEE Engineering in Medicine and Biology Society (EMBC)*, 2017, pp. 2928-2931.

[128] D. Singh, B. K. Singh, and A. K. Behera, "Comparitive study of different IIR filter for denoising lung sound," in *2021 6th International Conference for Convergence in Technology (I2CT)*, 2021, pp. 1-3.

[129] N. S. Haider, R. Periyasamy, D. Joshi, and B. K. Singh, "Savitzky-Golay filter for denoising lung sound," *Brazilian Archives of Biology and Technology,* vol. 61, 2018.

[130] M. F. Syahputra, S. I. G. Situmeang, R. F. Rahmat, and R. Budiarto, "Noise reduction in breath sound files using Wavelet transform based filter," *IOP Conference Series: Materials Science and Engineering,* vol. 190, p. 012040, 2017.

[131] L. I. Rudin, S. Osher, and E. Fatemi, "Nonlinear total variation based noise removal algorithms," *Physica D: Nonlinear Phenomena,* vol. 60, no. 1, pp. 259-268, 1992.

[132] M. Sarkar, R. Bhardwaz, I. Madabhavi, and M. Modi, "Physical signs in patients with chronic obstructive pulmonary disease," *Lung India : official organ of Indian Chest Society,* vol. 36, no. 1, pp. 38-47, 2019.

[133] A. Bohadana, G. Izbicki, and S. S. Kraman, "Fundamentals of Lung Auscultation," *New England Journal of Medicine,* vol. 370, no. 8, pp. 744-751, 2014.

[134] T. Katila, P. Piirila, K. Kallio, E. Paajanen, T. Rosqvist, and A. R. Sovijarvi, "Original waveform of lung sound crackles: a case study of the effect of high-pass filtration," *Journal of Applied Physiology,* vol. 71, no. 6, pp. 2173-2177, 1991.

[135] D. Singh, B. K. Singh, and A. K. Behera, "Comparative analysis of Lung sound denoising technique," in *2020 First International Conference on Power, Control and Computing Technologies (ICPC2T)*, 2020, pp. 406-410.

[136] D. L. Donoho, I. M. Johnstone, G. Kerkyacharian, and D. Picard, "Wavelet shrinkage: Asymptopia?," *Journal of the Royal Statistical Society. Series B (Methodological),* vol. 57, no. 2, pp. 301-369, 1995.

[137] D. L. Donoho, "De-noising by soft-thresholding," *IEEE Transactions on Information Theory,* vol. 41, no. 3, pp. 613-627, 1995.

[138] D. L. Donoho and I. M. Johnstone, "Ideal spatial adaptation by Wavelet shrinkage," *Biometrika,* vol. 81, no. 3, pp. 425-455, 1994.

[139] P. G. Sandeep, M. S. Akbar, and G. B. Richard, "Improved wavelet denoising via empirical Wiener filtering," in *Proc.SPIE*, 1997, vol. 3169.

[140] N. Nikolaev, Z. Nikolov, A. Gotchev, and K. Egiazarian, "Wavelet domain Wiener filtering for ECG denoising using improved signal estimate," in *2000 IEEE International Conference on Acoustics, Speech, and Signal Processing. Proceedings*, 2000, vol. 6, pp. 3578-3581 vol.6.

[141] C. Hyeokho and R. Baraniuk, "Analysis of wavelet-domain Wiener filters," in *Proceedings of the IEEE-SP International Symposium on Time-Frequency and Time-Scale Analysis*, 1998, pp. 613-616.

[142] J. G. Gallaire and A. M. Sayeed, "Wavelet-based empirical Wiener filtering," in *Proceedings of the IEEE-SP International Symposium on Time-Frequency and Time-Scale Analysis*, 1998, pp. 641-644.

[143] M. Hsueh, H. Wu, and B. Lu, "The evaluation system for the computer simulation of the crackles in respirations," in *2019 21st International Conference on Advanced Communication Technology (ICACT)*, 2019, pp. 583-588.

[144] B. Lu, M. Liu, M. Hsueh, P. Lin, X. W. Li, and H. Wu, "Preliminary study on production of coarse and fine crackles in respiration using a model of communication theory," in *2020 22nd International Conference on Advanced Communication Technology (ICACT)*, 2020, pp. 461-464.

[145] B.-Y. Lu, H.-D. Wu, S.-R. Shih, F.-C. Chong, M.-L. Hsueh, and Y.-L. Chen, "Combination of frequency and amplitude-modulated model for the synthesis of normal and wheezing sounds," *Australasian Physical & Engineering Sciences in Medicine,* vol. 34, no. 4, pp. 449-457, 2011.

[146] R. L. H. Murphy, S. K. Holford, and W. C. Knowler, "Visual Lung-Sound Characterization by Time-Expanded Wave-Form Analysis," *New England Journal of Medicine,* vol. 296, no. 17, pp. 968-971, 1977.

[147] D. F. Ponte, R. Moraes, D. C. Hizume, and A. M. Alencar, "Characterization of crackles from patients with fibrosis, heart failure and pneumonia," *Medical Engineering & Physics,* vol. 35, no. 4, pp. 448-456, 2013.

[148] H. Kiyokawa, M. Greenberg, K. Shirota, and H. Pasterkamp, "Auditory detection of simulated crackles in breath sounds," *Chest,* vol. 119, no. 6, pp. 1886-1892, 2001.

[149] Y. Wu, G. Gao, and C. Cui, "Improved wavelet denoising by non-convex sparse regularization under double Wavelet domains," *IEEE Access,* vol. 7, pp. 30659-30671, 2019.

[150] J. L. Darbyshire, M. Müller-Trapet, J. Cheer, F. M. Fazi, and J. D. Young, "Mapping sources of noise in an intensive care unit," *Anaesthesia,* vol. 74, no. 8, pp. 1018-1025, 2019.

[151] D. Garcia. *Noise variance estimation*. Available: https://www.mathworks.com/matlabcentral/fileexchange/25645-noise-variance-estimation (accessed on 20 Oct 2021)

[152] S. R. Messer, J. Agzarian, and D. Abbott, "Optimal wavelet denoising for phonocardiograms," *Microelectronics Journal,* vol. 32, no. 12, pp. 931-941, 2001.

[153] S. Charleston-Villalobos, R. Gonzalez-Camarena, G. Chi-Lem, and T. Aljama-Corrales, "Acoustic thoracic images for transmitted glottal sounds," in *2007 29th Annual International Conference of the IEEE Engineering in Medicine and Biology Society*, pp. 3481-3484.

[154] U. Beckmann, D. M. Gillies, S. M. Berenholtz, A. W. Wu, and P. Pronovost, "Incidents relating to the intra-hospital transfer of critically ill patients. An analysis of the reports submitted to the Australian Incident Monitoring Study in Intensive Care," *Intensive Care Med,* vol. 30, no. 8, pp. 1579-85, 2004.

[155] C. TDK Group. *ICS-52000*. Available: https://invensense.tdk.com/products/ics-52000/ (accessed 18 May 2023)

[156] E. Messner, M. Hagmüller, P. Swatek, and F. Pernkopf, "A Robust Multichannel Lung Sound Recording Device," *International Joint Conference on Biomedical Engineering Systems and Technologies*, Rome, Italy, 2016.

[157] PJRC. (30 Jan). *Teensy® 3.6 Development Board*. Available: https://www.pjrc.com/store/teensy36.html (accessed 18 May 2023)

[158] S. M. A. Salehin and T. D. Abhayapala, "Lung sound localization using array of acoustic sensors," in *2008 2nd International Conference on Signal Processing and Communication Systems*, 2008, pp. 1-5.

[159] D. Skalicky, V. Koucky, D. Hadraba, M. Viteznik, M. Dub, and F. Lopot, "Detection of respiratory phases in a breath sound and their subsequent utilization in a diagnosis," *Applied Sciences*, vol. 11, no. 14. pp 6535, 2021.